Muonic Background Analysis in GERDA Phase II (II+) and in LEGEND-200 Commissioning Data

Dissertation

der Mathematisch-Naturwissenschaftlichen Fakultät

der Eberhard Karls Universität Tübingen

zur Erlangung des Grades eines

Doktors der Naturwissenschaften

(Dr. rer. nat.)

vorgelegt von

Khushbakht Habib

aus Peschawar, Pakistan

Tübingen

2023

Gedruckt mit Genehmigung der Mathematisch-Naturwissenschaftlichen Fakultät der Eberhard Karls Universität Tübingen.

Tag der mündlichen Qualifikation:	23.11.2023
Dekan:	Prof. Dr. Thilo Stehle
1. Berichterstatter:	Prof. Dr. Joseph Jochum
2. Berichterstatter:	Prof. Dr. Tobias Lachenmaier

Dedicated to my parents,
who admire education in the highest regard, in a land where the
importance of womens' education
is often underestimated

Abstract

Muons can generate a non-negligible background in rare-event experiments, such as GERDA and LEGEND which are dedicated to the search of neutrinoless double-beta decay ($0\nu\beta\beta$) in the isotope of ^{76}Ge. Cosmogenic muons, with their variable kinetic energy depending on the progenitor particle, have the capability to penetrate even the most deep underground laboratories. For this reason, both GERDA and its successor, LEGEND-200, are equipped with a powerful Cherenkov veto system which was initially designed, constructed, and recently refurbished by the University of Tübingen.

In this work, both direct and indirect muonic-induced background in the entire GERDA Phase II and Phase II+ data was studied. Coincidence events with the germanium detectors were examined and muon-germanium coincidences were clearly identified by using a timestamp correlation method between germanium and muon events. The residual muonic background after all the analysis cuts were studied in detail, and it highlights the essential requirement for the muon veto system in the next-generation LEGEND experiment. Two approaches were used to detect the cosmogenic isotopes produced by muons through spallation. Both approaches yielded results consistent with zero, indicating the absence of cosmogenic events in GERDA Phase II and Phase II+ data. Existing hardware components were carefully maintained, subject to frequent calibrations and monitoring over the duration of this work, ensuring a reliable performance of the veto. In addition, the radioactive background peak attributed to ^{137}Cs was investigated in the GERDA data. The source of this radioactive peak was traced back to the detector holder plates and bars employed in the GERDA setup. Furthermore, Monte Carlo simulations were employed within the GERDA dataset to study the impact of removing oil from the PMTs. These simulations provided the founda-

tion for affirming that the sensitivity of the Cherenkov veto system would remain sufficient following the repair, ensuring its effectiveness in the LEGEND-200 experiment.

This thesis also presents the upgrades to the data acquisition and analysis systems to cope with the new software and hardware requirements of the LEGEND-200 experiment. Notably, the new hardware trigger threshold was chosen in a way that the muon sample is recorded with minimal random coincidences. The first set of digital signal processing parameters for analyzing LEGEND-200's new data was implemented. Additionally, further selection criteria were defined to accurately identify true muon events in the data. Through a comprehensive analysis of commissioning data, together with regular monitoring, and frequent calibrations after the refurbishment of the muon veto, the good performance of the veto system is precisely verified.

Zusammenfassung

Myonen können bei Experimenten mit seltenen Ereignissen einen nicht zu vernachlässigenden Hintergrund erzeugen, wie z. B. bei GERDA und LEGEND, die der Suche nach dem neutrinolosen Doppelbetazerfall ($0\nu\beta\beta$) im ^{76}Ge Isotop gewidmet sind. Kosmogene Myonen mit ihrer je nach Vorläuferteilchen variablen kinetischen Energie sind in der Lage, selbst die tiefsten unterirdischen Laboratorien zu durchdringen. Aus diesem Grund sind sowohl GERDA als auch sein Nachfolger, LEGEND-200, mit einem leistungsstarken Cherenkov-Vetosystem ausgestattet, das ursprünglich von der Universität Tübingen entworfen, gebaut und kürzlich berarbeitet wurde.

In dieser Arbeit wurde sowohl der direkte als auch der indirekte muonische Hintergrund in den gesamten GERDA Phase II und Phase II+ Daten untersucht. Koinzidenzereignisse mit den Germaniumdetektoren wurden untersucht, und Myonen-Germanium-Koinzidenzen wurden mit Hilfe einer Zeitstempel Korrelationsmethode zwischen Germanium- und Myonenereignissen eindeutig identifiziert. Der verbleibende Myonenhintergrund nach allen Analyseschnitten wurde detailliert untersucht und verdeutlicht die wesentliche Anforderung an das Myonen-Veto-System im LEGEND Experiment der nächsten Generation. Zum Nachweis der kosmogenen Isotope, die von Myonen durch Spallation erzeugt werden, wurden zwei Ansätze verwendet. Beide Ansätze lieferten Ergebnisse, die mit Null übereinstimmten, was darauf hindeutet, dass es in den GERDA-Daten der Phase II und der Phase II+ keine kosmogenen Ereignisse gibt. Die vorhandenen Hardwarekomponenten wurden sorgfältig gewartet und während der gesamten Dauer dieser Arbeiten häufig kalibriert und überwacht, um eine zuverlässige Leistung des Vetos zu gewährleisten. Darüber hinaus wurde die in den GERDA-Daten gefundene Hintergurnd-Line, die dem radioaktiven Zerfall von ^{137}Cs zuge-

schrieben wird, detailliert untersucht. Die Quelle dieses radioaktiven Peaks wurde auf die zurückgeführt Detektorhalterplatten und -stangen, die im GERDA-Gehäuse verwendet werden. Darüber hinaus wurden Monte-Carlo-Simulationen mit dem GERDA-Datensatz durchgeführt, um die Auswirkungen der Entfernung von Öl aus den PMTs zu untersuchen. Diese Simulationen lieferten die Grundlage für die Bestätigung, dass die Empfindlichkeit des Cherenkov Vetosystems auch nach der Reparatur ausreichend ist, um seine Wirksamkeit im LEGEND-200 Experiment zu gewährleisten.

In dieser Arbeit werden auch die Upgrades der Datenerfassungs- und Analysesysteme vorgestellt, um den neuen Software- und Hardwareanforderungen des LEGEND-200-Experiments gerecht zu werden. Insbesondere wurde die neue Hardware-Triggerschwelle so gewählt, dass die Anzahl der zuflligen Koinzidenzen frdas Myon-Veto minimiert wird. Der erste Satz digitaler Signalverarbeitungsparameter für die Analyse der neuen Daten von LEGEND-200 wurde implementiert. Zusätzlich wurden weitere Auswahlkriterien definiert, um echte Myonenereignisse in den Daten genau zu identifizieren. Durch eine umfassende Analyse der commi-ssioning-Daten, zusammen mit der regelmüigen Überwachung und häufigen Kalibrierungen nach der berarbeitung des Myonen-Vetos wird die gute Leistung des Vetosystems genau überprüft.

Contents

Chapter 1

Neutrino Physics

In 1930, Wolfgang Pauli postulated an electrically neutral, spin 1/2, and weekly interacting particle as a way to solve a puzzle related to the conservation of energy in beta decay. His idea was that this new particle, later named the "neutrino", could carry away the missing energy. Even though it was initially thought to be impossible to detect, in 1956, Cowan and Reines managed to actually observe these elusive particles experimentally through inverse beta-decay [1]. This discovery marked a turning point, and raised a series of questions: Do neutrinos have mass? Could they be their own antiparticles? If they possess mass, which type of neutrino is the heaviest? Furthermore, how did they play a role in the emergence of matter-antimatter asymmetry? These inquiries are essential because the answers could reshape our understanding of particle physics. The answer to the first question regarding neutrino mass could have been answered already through the observation of Neutrino oscillations, a phenomenon where neutrinos switch between different "flavors". However, no clear answers have been found for the remaining questions, yet.

One fascinating way to answer these questions is the search for neutrinoless double beta decay, a phenomenon that, if detected, would reveal profound information about neutrinos. For instance, it would confirm that a neutrino is its own anti-particle as well as provide evidence of a lepton number violation. Additionally, it could help determine the absolute mass scale of neutrinos. In this chapter, the existing knowledge of neutrino physics will be briefly reviewed. Furthermore, an introduction to Neutrinoless double beta decay ($0\nu\beta\beta$) decay and the

idea of its experimental search will be presented.

1.1 Masses of Neutrino

Thanks to the significant advancements in detector and accelerator technologies, we now know that the detected neutrinos by Cowan and Reines were electron neutrinos, (ν_e). Additionally, in general, neutrinos exhibit three distinct "flavors" denoted as ν_e, ν_μ and ν_τ, like the charged leptons 'l' = (e, μ, τ) with which they couple. Neutrinos were originally integrated into the Standard Model (SM) of particle physics as massless, left-handed particles possessing spin 1/2 and thus, they only interact weakly. For each left-handed neutrino (ν_l), there exists a corresponding right-handed anti-neutrino ($\bar{\nu}_l$). Both neutrinos and anti-neutrinos possess a conserved lepton number, denoted as $L_{\nu_l} = 1$ and $L_{\bar{\nu}_l} = -1$, respectively [2]. For over half a century, neutrinos were considered to be massless. However, nowadays they are known to have a little mass, yet the exact value and the theoretical mechanism responsible for their mass generation remain unresolved.

1.1.1 Neutrino Oscillation and Mass Ordering

Several experiments have provided clear evidence supporting the phenomenon of neutrino oscillations. This intriguing phenomenon has been observed in neutrinos from different sources such as solar neutrinos [3, 4], reactor and atmospheric [5, 6], as well as accelerator neutrinos [7, 8]. In quantum mechanics, mass and flavor eigenstates don't have to be essentially the same. The concept of neutrino oscillation relies on the fact that neutrinos are comprised of distinct mass eigenstates, which inherently differ from the neutrino flavor eigenstates. Specifically, the flavor states (ν, ν_μ, and ν_τ) are superposition of the 3 mass eigenstates (ν_1, ν_2 and ν_3) while the mass eigenstates are likewise superposition of the flavor eigenstates. This relationship can be mathematically expressed in the flavor basis as a superposition of 3 mass eigenstates ($\nu_j \in$ [1,2,3]), as follows:

$$\nu_l = \sum_{j=1}^{3} U_{lj} \ \nu_j \tag{1.1}$$

Here, the index 'l' refers to the different families of leptons i.e. (l = e, μ and τ) and j runs over three mass eigenstates (ν_j), each with a specific mass m_j. The relation among the states is defined through a neutrino mixing matrix U_{lj}, known as the Pontecorvo-Maki-Nakagawa-Sakata (PMNS) matrix [9]. The components of this matrix represent the probability amplitude for a ν_l neutrino to be in the steady state ν_j. This discovery confirmed that neutrinos possess mass and marked the first evidence of physics beyond the standard model.

Neutrino Mass Ordering: The study of neutrino oscillations allows only the measurement of the squares of the mass differences Δm^2_{ij}. However, it doesn't provide insights into the absolute scale of neutrino mass nor about the lightest mass state. Based on the assumption that each particular state possesses a different mass and that $\Delta m^2_{21} < \Delta m^2_{31}$ as known from experiments [10], their values could be organized in the following two ways, known as normal and inverted order [11]:

- Normal Ordering (NO): $m_1 < m_2 < m_3$
- Inverted Ordering (IO): $m_3 < m_1 < m_2$

The schematic representation of these two neutrino mass orderings is illustrated in Figure 1.1.

1.1.2 Dirac and Majorana Mass of Neutrino

In the domain of the standard model, all fermions are characterized as spin 1/2 particles, and their behavior is described by the Dirac theory [13] of fermions, a framework further refined by the contributions of Gell-Mann and Feynman [14]. Within this framework, the mass terms in the Lagrangian L(D) appear in the form:

$$\mathcal{L}_{Dirac} = -M_D \bar{\nu}\nu = -M_D(\bar{\nu}_L \nu_R + \bar{\nu}_R \nu_L) \tag{1.2}$$

where M_D is denoted as a Dirac mass, and $\nu_{L,R}$ and $\bar{\nu}_{L,R}$ are the right and left handed neutrino fields play the role of annihilating and generating fermions with left or right chirality respectively. A mass term as shown in Equation 1.2 needs the existence of fermions possessing both right and left chirality, a characteristic that

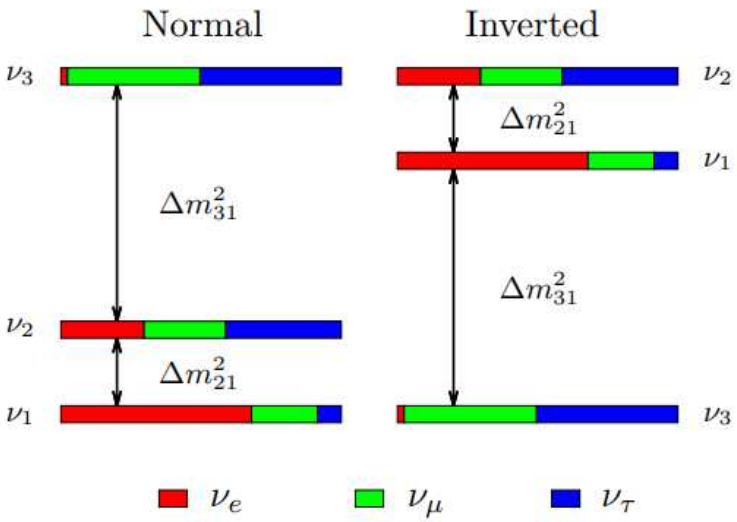

Figure 1.1: Two possible schemes of neutrino mass ordering. (Left) The normal ordering (NO), where ν_1 corresponds to the lightest among the mass eigenstates. (Right) The invited ordering (IO), highlighting ν_3 as the lightest mass eigenstate. The fractions of the neutrino flavors ν_e, ν_μ and ν_τ are displayed, providing a visual representation of their proportions within each mass hierarchy [12].

has been experimentally validated for all charged fermions. However, within the domain of neutrinos, there has not (yet) been an experimental observation of the right-handed neutrino. According to Equation 1.2, this situation could potentially be explained by the condition of the Dirac mass M_D being equated to zero.

Majorana Neutrinos: In 1937 Ettore Majorana proposed an alternate solution for Equation 1.2. He kept the previously existing left-handed neutrino field ν_L and, under the assumption that the neutrino is its own antiparticle ($\nu = \nu^C$), this yields the expression for the neutrino field as $\nu = \nu_R + \nu_L = \nu_L^C + \nu_L$, which is predicated on the assumption i.e. $\nu_R = C\bar{\nu}_L^T = \nu_L^C$. This approach enables the reformulation of the Dirac equation and the addition of another mass term into the Lagrangian without the need for the right-handed neutrino field ν_R and hence leads to the introduction of the Majorana mass term, represented as:

$$\mathcal{L}_{Majorana} = -\frac{1}{2} m_L (\bar{\nu}_L^C \nu_L + \bar{\nu}_L \nu_L^C) \tag{1.3}$$

This formulation can also be extended to right-handed neutrino fields. If right-handed neutrinos indeed exist, it opens the possibility that neutrinos could possess both a Majorana and Dirac mass component.

1.2 Double Beta Decay

Exploring the fundamental nature of neutrinos can be most effectively pursued through Neutrinoless Double Beta decay, commonly denoted as "$0\nu\beta\beta$-decay". If this decay exists, it represents a special case of the neutrino-accompanied double beta decay, denoted as "$2\nu\beta\beta$-decay", which is permissible within the standard model of particle physics. A brief description of these two types of double beta decay is presented in the following sections.

1.2.1 Standard and Two-Neutrino Double Beta Decay

In a standard negative beta (β^-) decay, a neutron within an atomic nucleus undergoes a transformation, being converted into a proton. This transformation is followed by the release of an electron, also known as a beta-minus (β-) particle and an associated anti-neutrino which ensures the conservation of the lepton number. The phenomenon of the beta decay of the nucleus is illustrated as follows:

$$ {}^{A}_{Z}X \longrightarrow {}^{A}_{Z+1}Y + e^- + \bar{\nu}_e \tag{1.4} $$

where X and Y represent the mother and daughter nucleus, and A and Z denote the mass number and atomic number, respectively. In nature, the process of double beta decay can happen in isotopes where a regular beta decay is energetically prohibited. However, the beta decay of two neutrons is both possible and energetically favored, as shown in Figure 1.2. The nuclear decay when two neutrons simultaneously convert into two protons with the emission of two electrons, and two anti-neutrinos known as $2\nu\beta\beta$ decay is presented as:

$$ {}^{A}_{Z}X \longrightarrow {}^{A}_{Z+2}Y + 2e^- + 2\bar{\nu}_e \tag{1.5} $$

The total energy $Q_{\beta\beta}$ liberated in double beta decay is distributed among the final-state particles, resulting in a continuous energy spectrum for the combined energy of the two detectable electrons, as illustrated in Figure 1.3. While the $2\nu\beta\beta$-decay is not forbidden for isotopes capable of undergoing a single beta decay, it is a second-order process and remains unobservable due to significantly lower probabilities compared to simple beta decay. The half-life ($T^{2\nu}_{1/2}$) varies for each

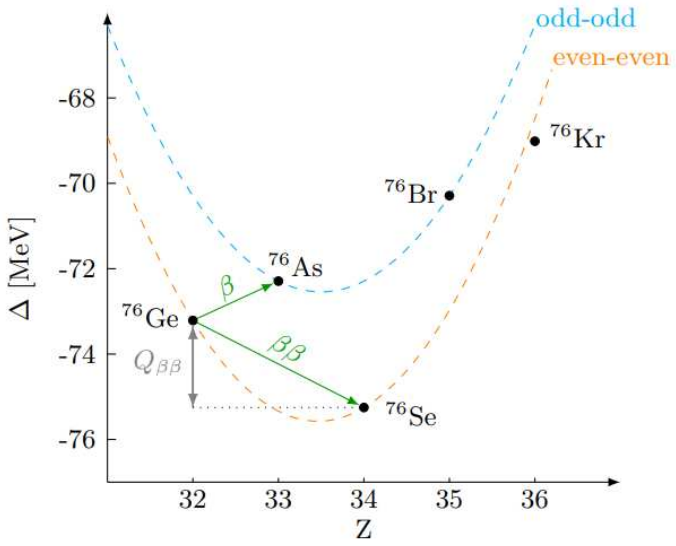

Figure 1.2: Illustration of the decay scheme for isobars with a mass number of A = 76. A standard β-decay shifts between the odd-odd and even-even mass parabola. The β-decay of ^{76}Ge to ^{76}As is energetically prohibited. However, the double beta ($\beta\beta$) decay to ^{76}Se is allowed. Figure source [15]

isotope but falls within the range of 10^{18} to 10^{24} years [16]. Table 1.1 presents a selection of double beta decaying nuclei, along with their corresponding $Q_{\beta\beta}$ values and natural abundances.

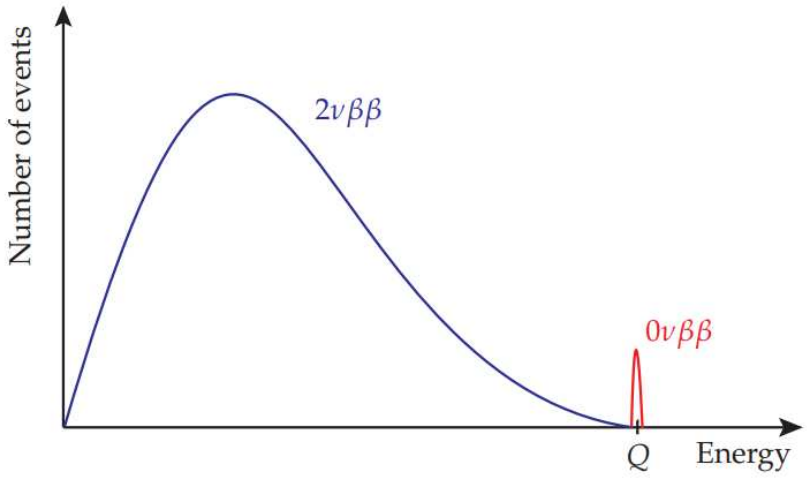

Figure 1.3: The schematic illustrates the total energy spectra of the emitted electrons for two modes of double beta decay of ^{76}Ge. The continuous spectrum (blue) represents the $2\nu\beta\beta$ decay mode, while the single peak (red) at $Q_{\beta\beta}$ corresponds to $0\nu\beta\beta$ decay [17].

Isotope	$Q_{\beta\beta}$ [keV]	Natural ab. [%]
^{150}Nd	3367.3	5.6
^{136}Xe	2461.9	8.9
^{130}Te	2530.3	34.5
^{124}Sn	2287.7	5.6
^{116}Cd	2809.1	7.6
^{110}Pd	2004.0	11.8
^{100}Mo	3035.0	9.6
^{96}Zr	3347.7	2.8
^{82}Se	2995.5	9.2
^{76}Ge	2039.1	7.8
^{48}Ca	4273.7	0.187

Table 1.1: The table provides a list of isotopes that undergo double beta decay, along with their respective $Q_{\beta\beta}$ values and natural abundances. Data source [18].

1.2.2 Neutrinoless Double Beta Decay

In $\beta\beta$ decay, the nucleus undergoes a process in which it releases two electrons and two $\overline{\nu}$, as dipicted in Equation 1.5. In contrast, Neutrinoless double beta decay, or $0\nu\beta\beta$ decay, referees to the scenario where, during the decay process, the neutrinos produced are absorbed at two vertices. This unique decay is possible only if neutrinos and antineutrinos possess the Majorana nature. Since no neutrinos are emitted, the energy of the 2 electrons should precisely equal to $Q_{\beta\beta}$, thus simplifying their identification. The mathematical expression for this decay is provided by Equation 1.6, and its characteristic signature is shown by a red line in Figure 1.3. The Feynmann diagram that represents both $2\nu\beta\beta$ decay and $0\nu\beta\beta$ decay can be observed in Figure 2.4(a) and (b) respectively.

$$ {}^{A}_{Z}X \longrightarrow {}^{A}_{Z+2}Y + 2e^{-} \tag{1.6} $$

The detection of $0\nu\beta\beta$ decay would lead to a lepton number violation, i.e. an imbalance in the number of leptons before and after the decay. This observation would also serve as evidence for the Majorana nature of the neutrino, indicating the presence of its own antiparticle [19]. The existence of $0\nu\beta\beta$ decay and the

extent of lepton violation could play a significant role in determining parameters for leptogenesis, thereby advancing our understanding of the fundamental matter-antimatter asymmetry in the universe.

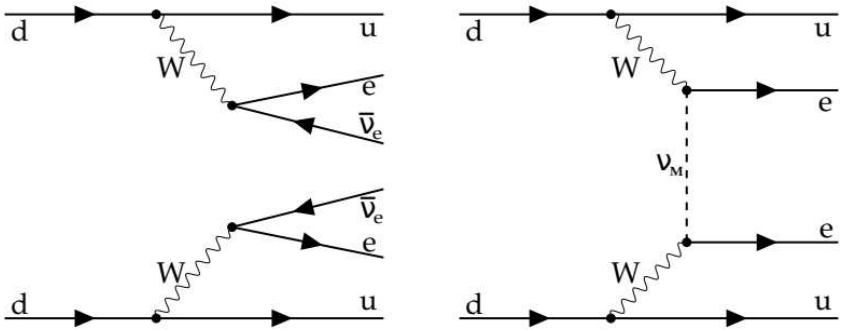

Figure 1.4: Two types of double beta decays. (Left) $2\nu\beta\beta$ involves the emission of two anti-neutrinos, conserving lepton number. (Right) The process of $0\nu\beta\beta$ occurs through the exchange of a massive Majorana neutrino (shown by ν_M), leading to lepton number violation. Source [20]

By measuring the half-life of neutrinoless double beta decay ($T_{1/2}^{0\nu\beta\beta}$), it becomes possible to figure out various other physical properties of the neutrino, including its mass [21]. As mentioned before, the neutrino was originally assumed to be massless until the discovery of neutrino oscillations. Although these oscillations were unable to determine the absolute neutrino mass, but it did reveal a three-neutrino mixing framework. Within this framework, neutrino mass is generated via neutrino mass matrix, expressed as $m_\nu = U \cdot U^T \cdot m_{jj}$. In this equation, m_{jj} indicates the diagonal matrix of the three massive states (m_{jj}, j = 1, 2, 3), and U represents the Pontecorvo-Maki-Nakagawa-Sakata matrix, as depicted in Equation 1.1. Assuming that neutrino is a massive Majorana particle and that no other non-neutrino processes are involved in the neutrinoless double beta decay ($0\nu\beta\beta$), a relationship can be established between the half-life of $0\nu\beta\beta$ decay and the effective neutrino mass ($m_{\beta\beta}$) [22] as follows:

$$T_{1/2}^{0\nu} = \left(G|M|^2 < m_{\beta\beta} >^2\right)^{-1} \tag{1.7}$$

where G and M represents the phase space factor and nuclear matrix element. The equation reveals a direct relation between the neutrino mass, $m_{\beta\beta}$, and the half-life of $0\nu\beta\beta$ decay ($T_{1/2}^{0\nu\beta\beta}$). Figure 1.5 shows the allowed parameter space of $m_{\beta\beta}$ as a function of the lightest neutrino mass m_l. The solid black lines shows the

acceptable regions for both the inverted and normal ordering of neutrino masses. If no observation is made and a limit is established on $T^{0\nu}_{1/2}$, it's possible to set a limit on $m_{\beta\beta}$ assuming neutrino mass exchange, using Equation 1.7. However, the uncertainties in Nuclear Matrix Elements can lead to substantial uncertainties in the limits of the effective neutrino mass ($m_{\beta\beta}$). Notably, the GERDA experiment has presented a limit of $m_{\beta\beta} < 79$ to 180 meV, based on their analysis of ^{76}Ge [23]. Whereas, the upcoming generation of 0vbb-decay search experiments, aims to reach a sensitivity of $\mathcal{O}(10)$ meV for $<m_{\beta\beta}>$ [19] as depicted by blue line in Figure 1.5.

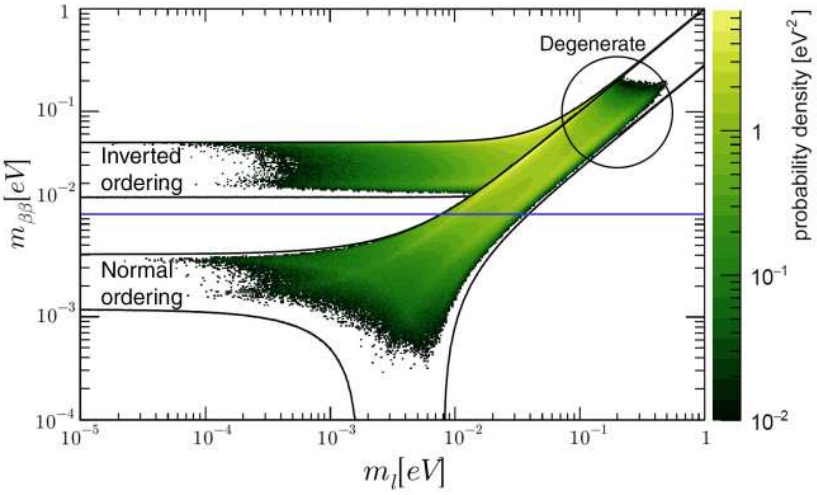

Figure 1.5: The probability density distribution of the effective Majorana neutrino mass ($m_{\beta\beta}$) plotted against the lightest neutrino mass. The permissible parameter range for both normal and inverted neutrino mass orderings are shown by solid black lines. The anticipated target of the next-generation experiment is highlighted by a blue line. Figure source [24]

1.3 Exploring $0\nu\beta\beta$ Decay: Experimetnal Search

In designing an experiment to search for $0\nu\beta\beta$ decay, it is important to understand the key factors that influence the sensitivity. The desired signal is a mono-energetic peak located at $Q_{\beta\beta}$ in the summed energy spectrum of the two emitted electrons, with a width of the peak set by the energy resolution of the detectors in use. Notably, $Q_{\beta\beta}$ can typically be measured with high precision via independent nuclear experiments. Therefore, a region of interest (ROI) can be confined to a narrow energy window centered around $Q_{\beta\beta}$. Within this ROI, the expected

number of events "N_{counts}", considering a total source mass "M" with an isotopic abundance "a", over a measurement time "t", [21] can be expressed as:

$$N_{counts} = ln2 \cdot \frac{N_A}{W} \left(\frac{a\epsilon Mt}{T^{0\nu}_{1/2}} \right) \tag{1.8}$$

Where "N_A" is Avogadro's number, "W" represents the molar mass of the target isotope, "ϵ" is the detection efficiency of the signal and "$T^{0\nu}_{1/2}$" denotes the half-life of the $0\nu\beta\beta$ decay.

The sensitivity of a $0\nu\beta\beta$ decay search experiment denoted as $S_{T^{0\nu\beta\beta}_{1/2}}$, with and without background can be mathematically described as:

$$S_{T^{0\nu\beta\beta}_{1/2}} \propto \begin{cases} a\epsilon Mt & \text{Background-free scenario} \\ a\epsilon\sqrt{\frac{Mt}{BI\Delta E}} & \text{With background scenario} \end{cases} \tag{1.9}$$

This equation represents two different scenarios. The first scenario shows the sensitivity in a background-free environment. In this ideal condition, the sensitivity to detect $0\nu\beta\beta$ decay with a specific half-life is directly proportional to the experiment's exposure, which is essentially the product of the total source mass (M) and the measurement time (t). Without any background, each count registered at $Q_{\beta\beta}$ represents the signal count. However, in the presence of a background, as indicated by the second scenario in Equation 1.9, the sensitivity follows a square root dependence, $S_{T_{1/2}} \propto \sqrt{Mt}$. In this context, the presence of background index (BI) and energy resolution (ΔE) decreases the sensitivity. Unlike the background-free scenario, not all counts registered at $Q_{\beta\beta}$ can be attributed to the signal. Hence, the success of a $0\nu\beta\beta$ decay search experiment essentially relies on both the background index and the total exposure of the experiment.

As per Equation 1.9, an isotope possessing a high natural abundance or has a higher potential for enrichment, low intrinsic background, and practically for use as a detector is considered highly advantageous. Furthermore, the detector should exhibit excellent energy resolution (small Δ E) and should be available in substantial quantities. Additionally, to minimize background from natural radioactivity, the $Q_{\beta\beta}$ value should ideally be above 2.6 MeV. Nevertheless, out of 35 viable isotopes, none of them fulfill all of these conditions. In reality, fewer than a third of them offer a suitable balance, making them feasible candidates for

the search for $0\nu\beta\beta$ decay as shown in Table 1.1. The GERDA and the LEGEND experiment using ^{76}Ge isotope to explore the neutrinoless $\beta\beta$ decay are explained in detail in the following chapters.

Chapter 2

Exploring Neutrinoless Double Beta Decay: GERDA and LEGEND

In this chapter, a comprehensive overview of the experimental setup of GERDA Phase II+ will be described (see Section 2.2.1), with emphasis on the benefits of using germanium (Ge) in double beta decay searches in Section 2.1. Furthermore, Section 2.2.2 describes the types of enriched Ge detectors used in GERDA Phase II+. The experimental approach and status of the next-generation LEGEND experiment, including both LEGEND-200 and LEGEND-1000, will also be reviewed in Section 2.3. This chapter serves as a review of experimental setups.

2.1 Germanium: As a Double Beta Decay Detector

Ever since transistors were invented in 1948 [25], germanium has been used in a wide range of applications. It's been essential in gamma-ray detection [26] and fiber optics [27, 28] as well as in a search for dark matter [29]. Nowadays, advanced technologies allows us to produce detector blanks with lengths and diameter of about 8 to 9 cm, using the Czochralski method [30]. With a level of impurities of the order of 10 billion atoms per cubic centimeter, such crystals can be effectively transformed into high-purity germanium (HPGe) detectors. A HPGe detector is a semiconductor device, containing two electrodes on the surface of the crystal to apply a bias voltage and establish a semiconductor junction throughout the entire detector volume. When a γ-ray or charged particle enters

the detector, it produces a large number of electron and hole pairs. The charge carriers of the same type, move towards the electrodes together as a cluster, guided by an electric field. This movement generates an electrical signal at the electrodes, which is typically read out by a charge-sensitive amplifier. By analyzing the time structure of the read-out signal, valuable information on the event's topology, such as the number and location of energy depositions can be determined.

The distinct signature of double beta ($\beta\beta$) decay is the emission of two electrons, whose combined energy (E) falls within the range $E \in [0, Q_{\beta\beta}]$ for $2\nu\beta\beta$ events or precisely $Q_{\beta\beta}$ for $0\nu\beta\beta$ decay. In 1967, Fiorini et al. recognized that such kind of signature could be detected using HPGe detectors [31] with high accuracy, which naturally possesses 7.75 (12)% [32] of the ^{76}Ge $\beta\beta$-decaying isotope. Since Ge is a semiconductor, it can be used as both source and detector at the same time leading to low background contamination and high detection efficiency. At $Q_{\beta\beta}$ = 2039.061 (7) keV [33], germanium detectors have already achieved an impressive resolution of approximately 2.0 keV. Moreover, the inherent high density of Ge crystals ensures that the two electrons sharing $Q_{\beta\beta}$ energy are absorbed within a few millimeters from its decay vertex. This leads to well-localized energy depositions that remain entirely contained within the detector.

Two former experiments based on ^{76}Ge isotope: the GERmanium Detector Array (GERDA) and the MAJORANA DEMONSTRATOR [34, 35], have achieved remarkable success in recent years and have brought the Ge detector design and technology to a new level. These experiments have recently concluded their operations and united to form the LEGEND collaboration, to continue the search of $0\nu\beta\beta$-decay with joint efforts and resources.

2.2 The GERDA Experiment

The GERDA experiment searches for the $0\nu\beta\beta$-decay of the ^{76}Ge isotope. The experimental concept is to immerse and operate bare HPGe detectors, isotopically enriched in ^{76}Ge, within a Liquid Argon (LAr) medium. The LAr serves both as a cooling agent for the detectors and as an effective shield against the radiation emitted by alpha (α), beta (β), and gamma (γ) decays occurring in the nearby or

surrounding materials. The experimental setup is explained in more detail in the following Section 2.2.1.

The experiment was strategically designed to achieve a total exposure of 100 kg · yr with a Background Index (BI) of $\mathcal{O}(10^{-3})$ counts / (keV·kg·yr), with the aim of exploring half-lives beyond 10^{26} years [36]. Beginning its data-taking in November 2011 with Phase I, GERDA operated 18 kg of enriched detectors during this initial phase. Phase II started after a major hardware upgrade, in December 2015, where new and innovative Broad Energy Germanium (BEGe) detectors [37], with a total mass of 35.6 kg were introduced into the experiment [38]. Furthermore, in May 2018, an additional 10 kg of detectors with the Inverted Coaxial (IC) geometry were brought into the setup, making the transition to Phase II+ [39]. After reaching the desired exposure of 100 kg·yr, the data collection was concluded in November 2019.

2.2.1 Experimental Setup

The GERDA experimental setup was located in Hall A at the Laboratori Nazionali del Gran Sasso (LNGS) and was shielded by 1400 meters of rock overburden, equivalent to 3500 meters water equivalent (m.w.e.). This shielding effectively reduces the muon flux to 1.25 / (m^2· h) [38].

Muon Veto: The GERDA's main tank has a diameter of 10 meters and is filled with 590 m^3 of ultra-pure water as shown in Figure 2.1a. This water effectively shields against neutrons from the rock surroundings and is equipped with 66 photomultiplier tubes (PMTs) to detect the Cherenkov radiation produced by the residual muons passing through the experiment. An additional part of the muon veto system was the plastic scintillator panels that were used to cover the "blind spot" above the neck of the cryostat, represented by the number '6' in Figure 2.1a. More detailed information about the muon veto system is provided in Chapter 4.

LAr veto: Inside the water tank lies a 4 m diameter cryostat. It is made up of stainless steel and filled with high-purity 64 m^3 liquid argon, which serves as both a cooling medium for Ge detectors and acts as a passive shield against external radiation. Events that deposit only a portion of their energy within the HPGe detectors are more likely to generate scintillation light within the surrounding LAr.

This scintillation light is collected by PMTs positioned above (9 PMTs) and below (7 PMTs) the detectors. Additionally, a system of wavelength-shifting (WLS) fibers surrounding the Ge detectors captures this scintillation light and guides it to silicon photomultipliers (SiPMs). Together they formed a LAr veto system, as depicted in Figure 2.1b, which acts in Anti-Coincidence (AC) with a signal in the Ge. A detailed description of the LAr veto system and its trigger conditions can be found in Section 3.3.2.

The Germanium Detector Array: At the central core of the experiment, Ge detectors were arranged in the form of seven strings, suspended within the LAr cryostat. The close-up view of this configuration, referred to as the germanium detector array, is shown in Figure 2.1c. Each string housed multiple detectors, with each detector connected vertically to its own holding frame. The bare Ge detectors were positioned on monocrystalline silicon plates, which were upheld by copper structural components. Each of these 40 cm long strings was covered in a transparent nylon 'mini shroud', which served as a mechanical barrier to prevent the accumulation of ^{42}K ions, resulting from the decay of ^{42}Ar, on the detector surfaces. A preliminary (two-stage) signal amplification was performed using custom-made front-end electronics positioned within the LAr at a distance of $\sim$ 30 cm above the detector array [40]. The bias voltage and signals were transmitted to and from the detectors through flexible flat cables chosen for their minimal radio purity and widespread availability. A comprehensive explanation of the type of detectors used in the GERDA experiment is presented in Section 2.2.

Clean Room: Situated on top of the experiment is a clean room where the detectors are carefully assembled into strings inside a glove box. These strings are then inserted into the setup through the lock system. The lock system contained 3 weak radioactive sources that could be lowered down to the detector array for calibrations of Ge-detectors [41]. A schematic layout of the clean room, lock system, and glove box is represented by numbers 3, 4, and 5 in Figure 2.1a.

2.2.2 The GERDA Detectors

All the HPGe detectors used in the GERDA experiment were made up of high-purity p-type germanium material. These detectors employ separate electrodes

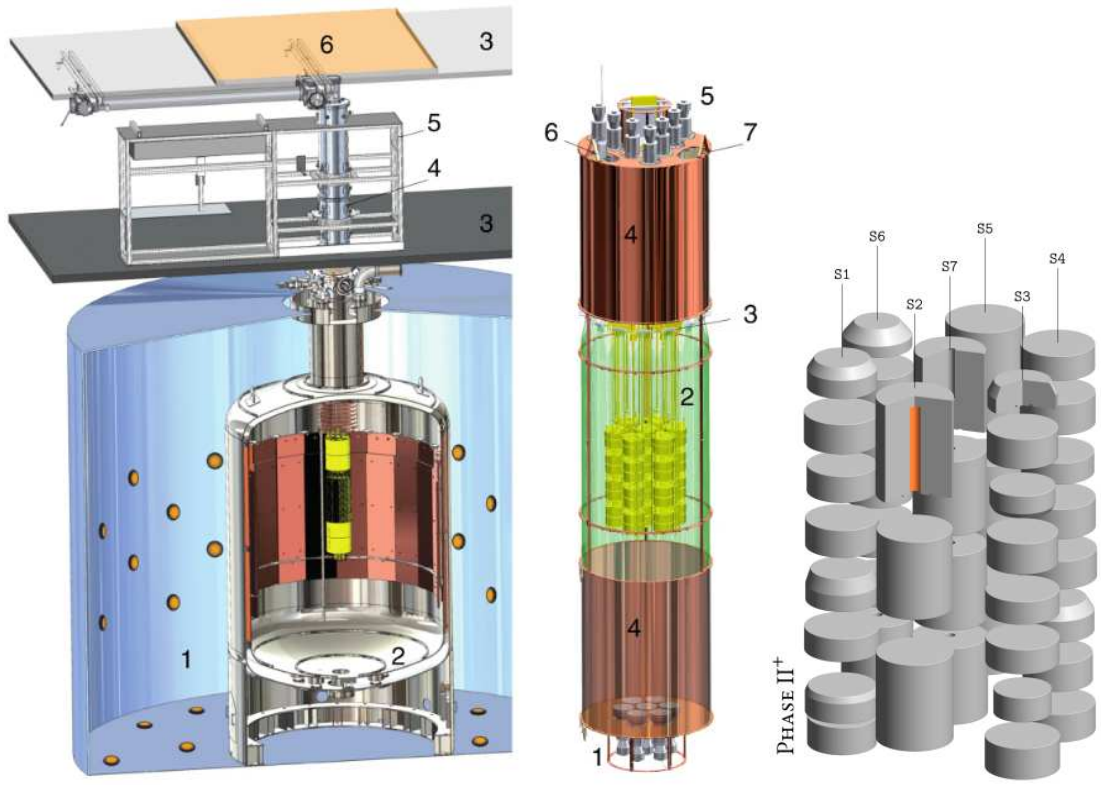

(a) Overview of the apparatus **(b)** LAr veto **(c)** Detector Array

Figure 2.1: The experimental setup of Gerda Phase II+. **(a):** Components include 1. Cerenkov water tank (10 m diameter), furnished with 66 PMTs; 2. LAr cryostat (4 m diameter); 3. Clean room's floor and roof on the top of the GERDA; 4. Lock system; 5. Glove-box; 6. Plastic scintillator veto panels. **(b):** Components include 1. The bottom plate (with 7 PMTs); 2. Fiber curtain; 3. Optical coupling and silicon photomultiplier (SiPMs); 4. Thin-walled copper cylinder; 5. Top plate (with 9 PMTs); 6. Slit for calibration source entry; 7. Second slit for calibration sources. **(c):** Layout displays HPGe detectors, organized in 7 labeled strings, forming the array; This is the layout of the array after the upgrade of May 2018. Images (a) and (b) are sourced from [42]. Image (c) was generated with [43].

for signal read-out and voltage biasing, referred to as the p+ and n+ contacts, respectively. The n+ contact where the external voltage is applied, encircles the detector and is formed by thermally diffusing a lithium layer onto the surface. This lithium layer diffused into the surface to a depth of around 1 mm. The presence of lithium impurities forms a region with a reduced charge collection efficiency (CCE), known as a 'dead layer', even when operating at full-depletion voltages. Within this region, the CCE is zero at the surface and increases gradually to its maximum value at the full charge collection depth (FCCD). In contrast, the p+ electrode, responsible for signal readout, is formed through boron implantation

and typically results in a smaller dead layer, approximately $\mathcal{O}(100)$ nm. These two conductive surfaces are separated by an insulating segment, which is created by carving a "groove". Gerda utilized three different geometries for Ge-detectors, as displayed in Figure 2.2.

2.2.2.1 The Semi-Coaxial Detector

The semi-coaxial (COAX) detectors exhibit a cylindrical shape with a central bore-hole running along the symmetry axis, extending nearly the entire length of the detector. The surface of the bore-hole is boron-implanted, highlighted in orange color in Figure 2.2a, forming a p+ electrode. The p+ electrode also extends to the bottom horizontal surface, ending at a passivated groove, whose thickness and depth are ~ 3 millimeters. The remaining part of the detector surface is Lithium-diffused, forming the n+ electrode. This structural design ensures a strong electric field along the entire crystal length, allowing the production of longer detectors (ranging from 8 to 10 cm), that can be effectively operated with voltages in the range of a few kilo-Volts. A total of seven coaxial detectors were inherited from the former IGEX [44] and Heidelberg-Moscow [45] experiments and were used in both Gerda Phase I and Phase II after refurbishment. However, during the transition to Phase II+, one of these detectors, exhibiting poor background discrimination performance, was discarded. In total, their combined masses contributed to 15.6 kg in Gerda Phase I and II and 14.6 kg in Phase II+.

2.2.2.2 The Broad Energy Germanium Detector

The Broad Energy Germanium (BEGe) detectors also possess cylindrical shape but are much shorter in size than the COAX detectors and exhibit different electrode structures as shown in Figure 2.2b. Unlike COAX detectors, the BEGe design does not include a bore-hole, resulting in small dot-shaped p+ contact located at the center of one of the two detector sides. Similar to COAX detectors, the n+ electrode of BEGe detectors extends down to the groove, wrapping around the detector on all surfaces. The BEGe detectors were specially manufactured for the Phase II campaign and the details of their production and characteristics can be found in Reference [46]. These detectors offer improved energy resolution,

background rejection capabilities, and excellent performance stability in comparison to COAX detectors. GERDA Phase II incorporated a total of 30 BEGe detectors, all produced from enriched HPGe material with a ^{76}Ge fraction of 87.8%, contributing to a combined mass of 20 kg [47].

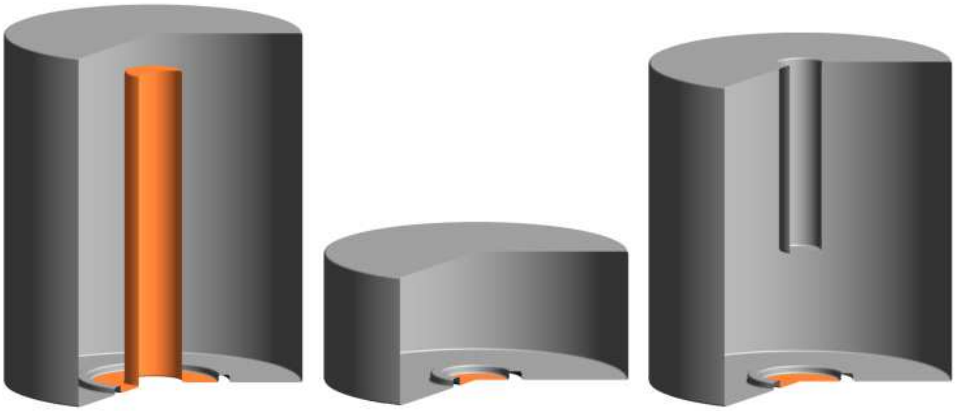

(a) Semi-Coaxial **(b)** BEGe **(c)** Inverted Coaxial

Figure 2.2: Types of detector geometries utilized in the GERDA experiment. The p+ electrodes are displayed in orange, while the n+ electrodes cover most of the surface, displayed in grey color, except for the small groove that provides electrical insulation. These geometries are produced with [43].

2.2.2.3 Inverted Coaxial Detector

For Phase II+, a set of five new detectors of Inverted-Coaxial (IC) type was fabricated and integrated into the existing detector array. This involved the replacement of three natural detectors located in string 7 with four of these enriched IC detectors, while a fifth one was placed at the bottom of string 6, replacing one COAX detector (referred to as ANG1). This innovative IC geometry design possesses a dot-shaped p+ contact (shown in orange, in Figure 2.2c), to enable BEGe-like pulse-shape discrimination capabilities, and a bore-hole on the opposite side, to make it possible to achieve higher detector masses. The remaining surface, including the surface of the bore-hole as depicted in grey in Figure 2.2c, forms the n+ contact. Collectively, these IC detectors contribute a combined mass of 9.6 kg to the Phase II+ configuration. A detailed description of the production and characterization of these IC detectors used in Gerda Phase II+ can be found in [39, 48].

By the conclusion of data-taking in November 2019, GERDA had accumulated a total exposure of 127.2 kg·yr. Throughout this duration, no indication of $0\nu\beta\beta$-decay was detected. With an energy resolution of 3.3 keV FWHM at $Q_{\beta\beta}$ and a background index of $(5.2^{+1.6}_{-1.3}) \times 10^{-4}$ counts/(keV·kg·yr), a recent lower limit for $T^{0\nu}_{1/2} > 1.8 \times 10^{26}$ yr at 90% C.L. in ^{76}Ge was established [23].

2.3 The LEGEND Experiment

The aim of the upcoming generation of $0\nu\beta\beta$-decay search experiments is to attain a sensitivity of ~ 10 meV for the effective Majorana neutrino mass and if exists, to detect $0\nu\beta\beta$ decay. To fulfill this goal within the scope of germanium technology, the GERDA and MAJORANA [49, 35] collaborations, alongside other research groups, joined together in 2016 to establish a new LEGEND collaboration which now consists of about 50 institutions and more than 250 members [50].

The LEGEND experiment, an acronym for "Large Enriched Germanium Experiment for Neutrinoless $\beta\beta$ Decay", is the world's most extensive $0\nu\beta\beta$-decay search experiment based on ^{76}Ge. It is planned to operate in two phases: LEGEND-200 succeeded by LEGEND-1000. These numbers represent the approximate enriched detector mass (in kg) being employed. With the LEGEND-200 phase, the goal is to achieve a sensitivity of $T^{0\nu}_{1/2} > 10^{27}$ years with an exposure of 1 t·yr over a span of 5 years of data-taking. This corresponds to setting an upper limit on the effective Majorana neutrino mass, $m_{\beta\beta}$, within the range of $(33 - 71)$ meV. To achieve this goal, the background index (BI) must be a factor of five lower than that of previous GERDA and MAJORANA experiments.

The upcoming LEGEND-1000 phase requires a significant improvement in background index which should be $< 10^{-5}$ counts/(keV·kg·yr) to operate in a background-free environment. With this background level in the energy range of $Q_{\beta\beta}$ and total exposure of 10 t·yr, the goal is to achieve a sensitivity for a limit of $T^{0\nu}_{1/2} > 10^{28}$ years within a 90% C.L. This achievement would result in effective Majorana neutrino mass, within a range of $(10 - 20)$ meV. Figure 2.3 illustrates a visual representation of the sensitivity on a $0\nu\beta\beta$ decay signal in ^{76}Ge as a function of exposure, for different background levels. The highlighted light blue band

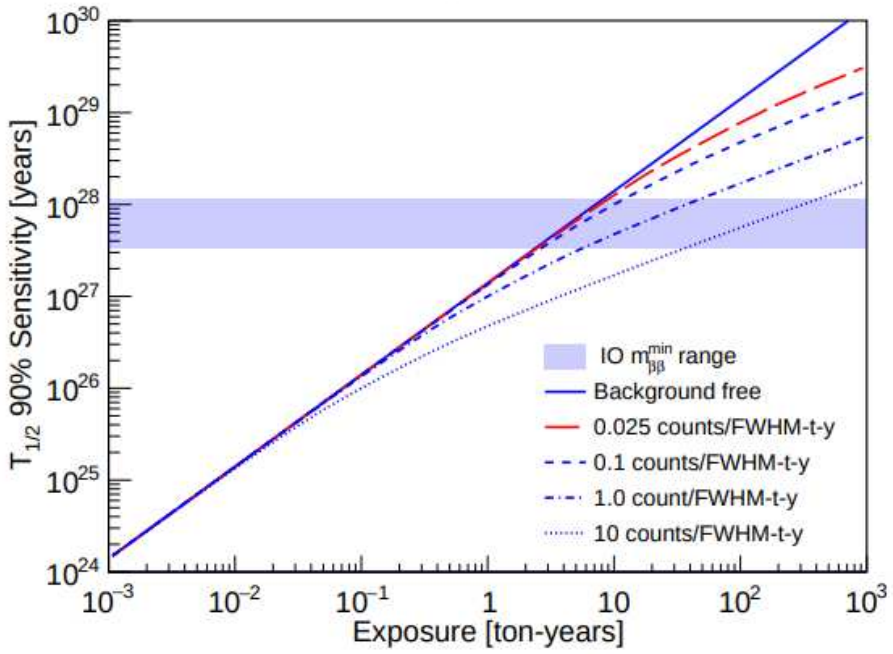

Figure 2.3: The sensitivity of the $0\nu\beta\beta$-decay half-life for ^{76}Ge, plotted against exposure at a 90% C.L. The plot includes various scenarios corresponding to different background levels, all normalized to an energy resolution of 2.5 keV. Figure Taken from [19].

corresponds to the region associated with the Inverted Neutrino mass Ordering (IO). The solid blue line represents the background-free scenario where sensitivity grows linearly with exposure, while the red line corresponds to the targeted background level in a more realistic or quasi-background-free context. Our background goal aligns with the red line, marked at 0.025 counts/(FWHM-t-y), signifying a "quasi-background-free" condition [19]. The background index values presented in the figure have been normalized to an energy resolution of 2.5 keV (FWHM).

2.3.1 LEGEND-200 Experiment: Design and Status

LEGEND-200 experiment took advantage of the existing infrastructure of GERDA at LNGS, which was adapted to hold 200 kg of enriched ^{76}Ge detectors within the LAr cryostat [19], with a background goal of < 0.6 counts/(FWHM·t·yr). The GERDA setup was handed over to the LEGEND collaboration in September 2020. After all the commissioning runs, the stable physics data-taking started in March 2023. Modifications and improvements were made to accommodate the 200 kg of

detector mass. For instance, to accommodate the longer strings, the lock system of the cryostat had to be replaced as it wasn't designed to handle the higher mass of the detector array. The clean room was also adjusted by removing the plastic scintillator panels from the top to create more space.

The LEGEND-200 detector array is a composite of detectors sourced from both the GERDA and MAJORANA experiments, in addition to newly produced detectors. Thus, the array contains a variety of enriched detectors, including BEGe detectors (transferred from GERDA), p-type Point Contact (PPC) detectors [51] (brought from MAJORANA), Inverted Coaxial Point Contact (ICPC) detectors [52] (newly produced) and a few coaxial detectors from GERDA. The newly introduced ICPC detector offers excellent pulse shape discrimination performance similar to the PPC and BEGe detectors [53], yet has a mass up to 4 times greater than the others. This feature makes these detectors ideal for the LEGEND experiment, as their larger mass helps to reduce the amount of detectors and thus its associated components such as detector holders and cables, which can contribute significantly to the background. The updated layout of the modified GERDA cryostat is presented in Figure 2.4a. This design is intended to house a total of 200 kg of Ge detectors, organized into 14 strings. To enhance the coverage of the fiber curtain, a dual-curtain configuration is employed in LEGEND-200, as illustrated in Figure 2.4b. It involves the placement of one curtain inside and one surrounding the detector array.

The readout electronics design adopted for LEGEND-200 is a hybrid design that combines the low-noise front-end readout technology from MAJORANA [54] with the wire bonding technique of GERDA [50]. This approach allows the placement of read-out electronics in close proximity to the detector ($\sim$ 5cm from the crystal base) inside the LAr. The integration of this low-noise readout electronics will result in improved pulse shape discrimination power and energy resolution.

In GERDA, the holding plates for the Ge-detectors were made from low background silicon (Si) material. However, in the LEGEND-200 setup, these Si plates have been replaced by poly(ethylene naphthalate) (PEN) [55] plates, in combination with a holding structure made up of electroformed copper. Both of these materials possess an incredibly low level of radioactive impurities. Moreover,

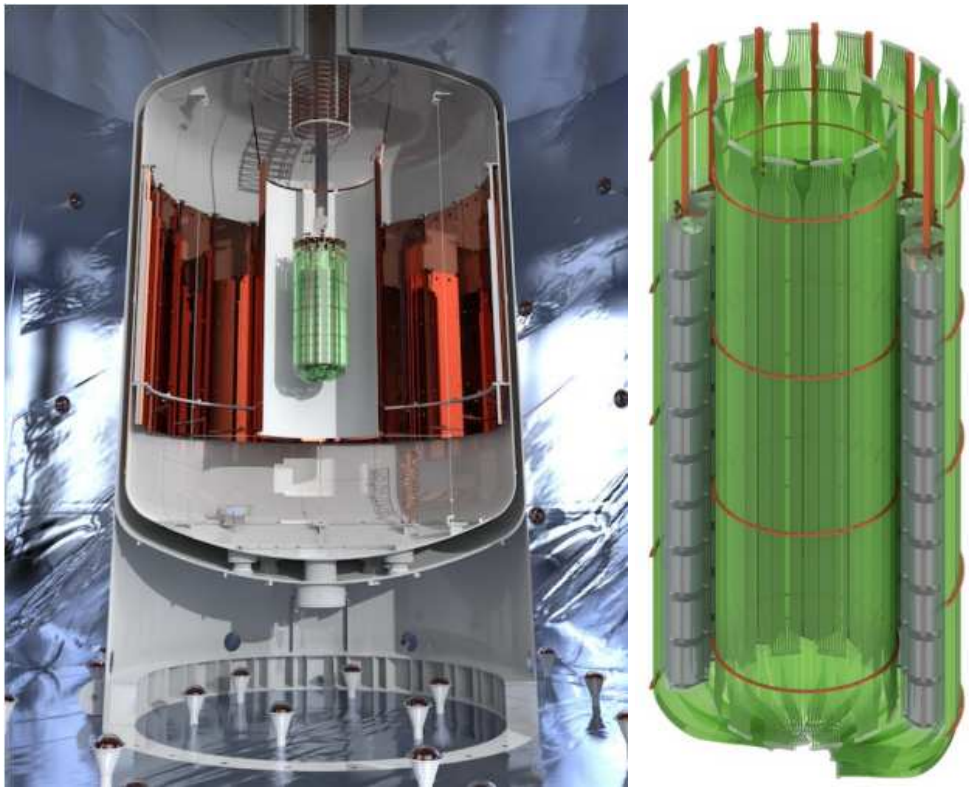

(a) (b)

Figure 2.4: (a) Schematic cross-section of the altered GERDA cryostat for LEGEND-200 featuring the modified lock system. (b) Configuration design of the 14-string array to house 200 kg of Ge detectors. Fiber curtains are displayed in green with one set of curtains inside and one surrounding the detector array. Images sourced from [19].

the PEN material has the additional property of being scintillating, which provides additional light for the events originating close to the detectors or from the PEN material itself. This feature increases the probability of such events being detected by the LAr veto.

2.3.2 LEGEND-1000 Experiment

The LEGEND-1000 experiment is planned to operate over a span of 10 years, incorporating around 1000 kg of enriched Ge detectors deployed in individual payloads. To achieve background-free conditions and to reach a sensitivity of a half-life greater than 10^{28} years, the background must be lowered by at least sixfold compared to the LEGEND-200 phase [19]. Due to the inherently low background, the existing background models carry large uncertainties, thus LEGEND-200 will provide more informed estimates for LEGEND-1000. Efforts to achieve these

strict background levels involve reducing radioactivity originating from the Uranium (U) and Thorium (Th) decay chains. This is planned through strategies like optimizing array spacing, employing larger detectors, minimizing the presence of inactive materials, enhancing light collection efficiency in the LAr medium, and using more cleaner materials. Moreover, the challenges such as the impact of ^{42}Ar can be mitigated by using argon from underground sources near the detectors and improving process control to minimize surface alpha contamination.

While the site for the upcoming LEGEND-1000 infrastructure is yet to be chosen, it is clear that the existing GERDA infrastructure will be insufficient to support the scale of detectors required for the LEGEND-1000.

In conclusion, the ongoing experiments dedicated to the search for $0\nu\beta\beta$-decay using Ge detectors have achieved remarkable advancements in enhancing both resolution and background reduction which are very important for future $0\nu\beta\beta$-decay signal discovery. LEGEND will continue a background-free search in a phased strategy with the initial phase, known as LEGEND-200 is presently in the process of collecting data as part of this ongoing search.

Chapter 3

Background Sources and their Reduction Techniques in GERDA

Rare-event search experiments, like GERDA or LEGEND, encounter numerous challenges in minimizing background contamination. To achieve the necessary reduction of background levels as required in these experiments, a thorough examination of all the components of background is required. The GERDA collaboration has made significant advancements in developing effective methods for identifying and reducing various sources of background. These advancements resulted in remarkable achievements within the GERDA experiment and will also be used in the LEGEND experiment to further enhance its performance.

This chapter provides an overview of the main sources of background originating from both internally and externally to the experiment. Additionally, it highlights the background reduction techniques used in GERDA such as detector Anti-Coincidence (AC) cut, Liquid Argon (LAr) veto, muon veto, and pulse shape discrimination (PSD) techniques to identify and effectively exclude these background sources. All the details presented in this chapter are developed within the GERDA collaboration and the author is not directly involved in their creation.

3.1 Internal Background Contributions

All the components used in an experiment, including the detector itself, poses a potential risk of background contamination. Such contamination can arise from

either the manufacturing process of the materials or the presence of primordial radionuclides [56]. Therefore, it is important to understand the internal radioactivity of these components and its impact on the sensitivity of the experiment including energy, rate, and type of the respective radiation. Having this information, it can be evaluated (via simulations) whether the emitted radiation can reach the detector and if so, whether the resulting deposited energy is high enough to mimic the desired signal.

The materials typically used in the experiments cannot be completely free from radioactive contamination. Nevertheless, there are certain materials known as low-background materials (i.e. semiconductor-grade Silicon, lead, Teflon (PTFE), copper and PEN) that are well-suited for use in environments where minimal background radiation is required. In order to clean these materials and reduce their background radiation, specific manufacturing and cleaning techniques have been developed [57, 58]. These methods help to minimize radioactive impurities and ensure that the materials have low levels of background radiation.

Primordial radionuclides are radioactive elements that were present even before the formation of the Earth, approximately 4.5 billion years ago. These radionuclides originated from the matter of the solar system and are expected to contaminate all components of experimental setups due to their significantly longer half-lives. To still be present today, these nuclides must have half-lives that exceed 50 million years. In low-background experiments, like GERDA and LEGEND, particular attention has been given to the radionuclides like Thorium-232 (^{232}Th) and Uranium-238 (^{238}U). It is because their decay chains produce daughter nuclei such as ^{208}Tl ($\gamma = 2615$ keV), ^{214}Bi ($\beta = 3270$ keV) and ^{222}Rn ($\alpha = 5490$ keV) [59] which emit radiation with energies that are high enough to contribute to the background near $Q_{\beta\beta}$ energy of ^{76}Ge.

In addition to primordial radionuclides, another significant contributor to the background radiation is ^{40}K, a naturally occurring radioisotope of potassium. Due to its half-life of 1.3×10^9 years [59], trace amounts of ^{40}K are expected to be present in various materials. The gamma radiation emitted by ^{40}K at 1460.9 keV does not possess enough energy to contribute to the background at $Q_{\beta\beta}$. However, it does contribute to the background for spectral analysis of $2\nu\beta\beta$ de-

cay. Furthermore, this background can also result in performance losses when applying analysis cuts based on signals with lower energies [19].

An additional source of background at $Q_{\beta\beta}$ is ^{42}Ar, which is a cosmogenically produced isotope that undergoes a beta-decay with a half life of 32.9 years. It is formed through neutron capture processes, specifically ^{40}Ar (n,γ) ^{41}Ar (n, γ) ^{42}Ar in environments that are rich in neutrons. Additionally, cosmic alphas contribute to the production of ^{42}Ar through the reaction ^{40}Ar (α,2p) ^{42}Ar in the atmosphere. The decay of ^{42}Ar leads to the formation of a short-lived daughter isotope called ^{42}K, which has a half life of 12 hours. ^{42}K undergoes beta decay with a Q value of 3525.2 keV, resulting in the production of the stable isotope ^{42}Ca. This background from ^{42}Ar has been detected in Liquid Argon (LAr) during GERDA commissioning runs. The beta decay of its daughter isotope ^{42}K can contribute to the background at $Q_{\beta\beta}$ if the decay happens near detector surfaces.

3.2 External Background Contributions

While it is possible to optimize the background introduced by the structural materials of an experiment through careful selection and thorough cleaning, an additional source of background arises from cosmic radiation. These high-energy particles coming from outer space can penetrate the experimental setup and contribute to the background. Therefore, measures must be taken to shield the experiment from cosmic rays or implement veto systems to identify and reject events caused by them. During the transportation or manufacturing process, various isotopes with both short and long half-lives can be produced. The resulting activation of the crystals can either be caused by spallation reactions, where fast nucleons from cosmic rays collide with the atoms in the crystals or by the capture of stopped muons and muon-induced neutrons. To minimize the impact of this cosmic radiation background, many low-background experiments are placed in deep underground laboratories. One such example is Laboratori Nazionali del Gran Sasso (LNGS), where the muon rate is approximately 1.25 $m^{-2}h^{-1}$, which represents a reduction of six orders of magnitude with a mean muon energy of 270 GeV compared to the muon rate at the surface of the Earth [60, 38].

Cosmic radiation can lead to radioactivity in materials through cosmogenic activation. This results in the production of radionuclides such as ^{60}Co, ^{39}Ar ,^{36}Cl and ^{68}Ge. In order to minimize this activation process as effectively as possible, the production and storage of low-background materials are often conducted underground [58]. Considering the precautions taken during the production and storage of low-background materials as well as the history of exposure to cosmic radiation, it can be inferred that the majority of the contamination produced from such exposure does not significantly contribute to the energy spectrum.

A simulation study presented in [61] investigated the impact of high-energy muons on germanium detectors and liquid argon (LAr) in the GERDA setup. The study showed that in-situ cosmogenic isotopes produced by these muons contribute to the ambient radioactivity at the $\mathcal{O}$ 1(nBq/kg) which is three orders of magnitude lower compared to the contribution from natural radioactivity. However, it is necessary to consider the presence of radioactive isotopes such as ^{75}Ga and ^{77m}Ge, which can be produced within the bulk of the enriched HPGe detectors. The beta emissions from these isotopes cannot be distinguished topologically from double beta decay events, potentially introducing background interference. Despite their lower contribution compared to natural radioactivity, it is important to take into account and manage carefully the presence of these radioactive isotopes.

3.3 Background Reduction Techniques in GERDA

GERDA and its successor LEGEND experiment, are designed with an objective of achieving a background-free environment throughout their operational lifetime. The ultimate aim is to distinguish and eliminate all detected background events occurring at the level of $Q_{\beta\beta}$ energy. To accomplish this goal of achieving a low background index in these experiments, various techniques have been developed and implemented for identifying and characterizing background sources. These methods have been actively utilized in the experiment to enhance background identification and its subsequent reduction.

In the following sub-sections, a short overview of background reduction tech-

niques used in GERDA Phase II are presented. These techniques consists of the several selection cuts such as the detector Anti-Coincidence (AC), the Liquid Argon (LAr) veto, the muon veto and the Pulse Shape Discrimination (PSD). Figure 3.1 presents a schematic representation of these selection methods. The fundamental idea behind these techniques is that the majority of double beta decay events (depicted in yellow) exhibit a point-like behavior, with two electrons depositing energy within a small volume (typically within 1 mm^3 [62]). Therefore, events with energy depositions occurring over large volumes can be readily identified and discarded as background events.

3.3.1 Anti-Coincidence (AC) Cut

The $0\nu\beta\beta$-decay event typically results in a localized energy deposition within the Ge crystal bulk. Hence, events that exhibit simultaneous energy depositions in multiple Ge detectors can be confidently rejected as background events using detector anti-coincidence (AC) cut. This behavior is depicted in Figure 3.1, where a γ event (shown in blue) is presented as an example. Furthermore, to reduce background interference, events that occur successively within a time window of 1 ms are excluded by this selection from the analysis. This exclusion criterion is implemented to effectively remove events that originate from the decay chains of primodial radionuclides, such as radon progenies ^{214}Po and ^{214}Bi [63].

3.3.2 Liquid Argon (LAr) Veto

The GERDA cryostat, filled with 64 m^3 of radio-pure liquid argon (LAr), simultaneously acted as: a coolant to maintain the desired temperature, a scintillator to detect particles, and a shield against external radiation. When ionizing radiation passes and interacts with the LAr, it emits scintillation light with a wavelength of 128 nm. To detect this scintillation light, optical fibers coated with a wavelength-shifting material called tetraphenyl butadiene (TPB) were used. These fibers guided the shifted light to silicon photomultipliers (SiPMs) for detection. The SiPMs and fibers were complemented with 16 PMTs coated with TPB. These PMTs were positioned above (9 PMTs pointing downward) and below (7 PMTs pointing upwards) the array of Ge detectors [63]. Additionally, the ny-

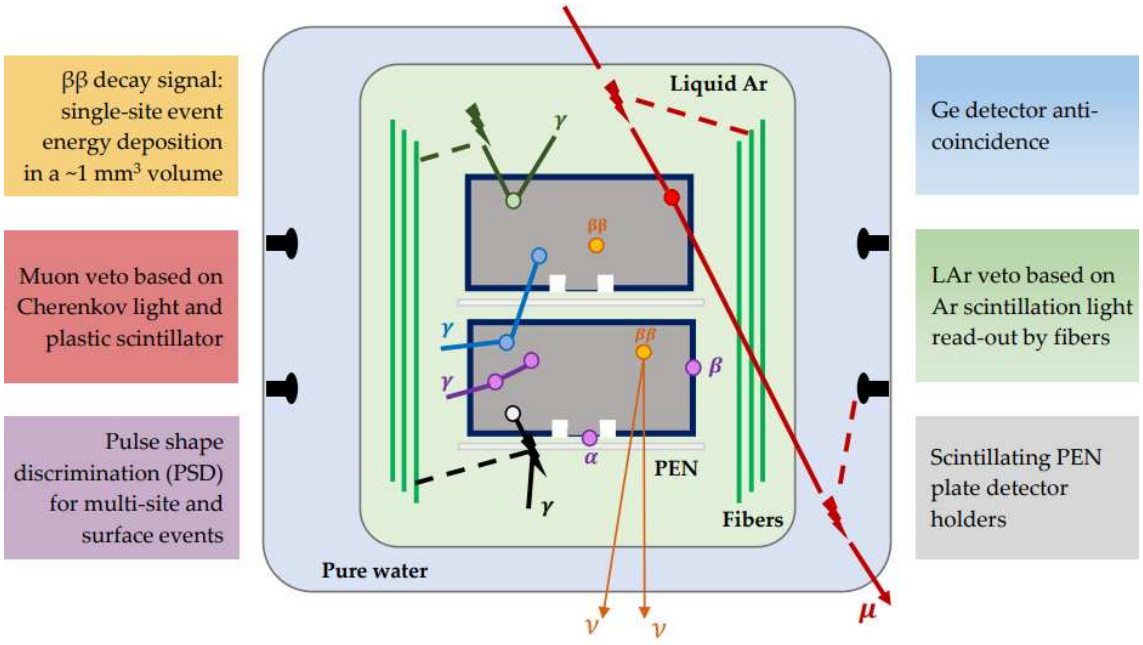

Figure 3.1: Graphical representation of the background event topologies observed in the GERDA experiment along with the corresponding reduction techniques. Two Ge-detectors, shown in grey color are placed on the Polyethylene Naphthalate (PEN) holders, as in the LEGEND-200 setup. The reduction techniques involve the detector AC cuts, muon, and LAr veto cuts, and PSD methods to reject MSE, as well as α and β surface events effectively. The figure is taken from [64].

lon mini-shrouds that surrounded the detector strings were also coated with TPB to enhance light collection efficiency. This method of background identification played a significant role for the GERDA experiment towards a background-free search for neutrinoless double beta decay [19].

To efficiently detect scintillation light, the GERDA experiment set a threshold at 50% of the expected amplitude of a single photoelectron in one sensor. The veto condition was fulfilled when at least 1 photoelectron within a specific time window of 6 μs around the germanium trigger was detected. The induced dead time by the LAr veto was 2.3% with a small uncertainty of 0.1%. The strong reduction power of the LAr veto system in reducing background events is demonstrated by the population of events at the 1525 keV ^{42}K line. This particular line is associated with a β and γ cascade, where the β particle can release $\sim$ 2 MeV of energy within the LAr medium, and the expected γ line at 1525 keV in Ge detectors is significantly suppressed by approximately a factor of 5 [63]. Figure 3.1 shows a schematic representation, where a γ event (depicted in dark green) illustrates

this principle. On the other hand, the 1461 keV line associated with ^{40}K shows very little suppression because of the electron capture without significant energy release in LAr.

3.3.3 Water Cherenkov Veto

The LAr cryostat is surrounded by a layer of pure water, serving as an additional shield. For instance, high energetic muons coming from cosmic radiation can deposit energy in almost all parts of the experimental setup. In order to detect these muonic-induced background in the HPGe detectors, a water cherenkov veto was used. The muon veto system consists of a large water tank filled with 590 m^3 of pure water and equipped with 60 $8^{''}$ photomultiplier tubes (PMTs) mounted on its walls. Additionally, 6 PMTs were placed in a small region under the cryostat (known as Pillbox) to detect Cherenkov light. To further reduce μ-induced background, three layers of plastic scintillators were installed above the clean room, covering the central area ($4 \times 3m^2$), to detect muons passing directly through the cryostat neck. To enhance the photon detection efficiency, the tank is covered with a highly reflective foil called VM2000 which has a reflectivity of $> 99\%$ [65]. An example of muon passing through the experiment, highlighted in red is shown in Figure 3.1.

In order to have a valid trigger for the muon veto system, certain conditions need to be fulfilled. For the main water tank, at least 5 out of the 66 PMTs need to detect a signal within a time window of 60 ns. Similarly, for the plastic veto on the top of the roof, a triple coincidence (all three layers) of signals within the same time window is required. Additionally, the PMTs in the water tank must collect more than 0.5 photoelectrons (PE) to ensure reliable detection of μ-induced signals. If a μ-tagged event occurs within a time window of 10 µs before a trigger in Ge detectors, it is classified as μ-induced background. This enables the identification of over 99% of muons that deposit energy in Ge detectors while inducing a low dead time of less than 0.1% [65]. A detailed analysis of these μ-induced events in GERDA Phase II data will be presented in the next chapter.

3.3.4 Pulse Shape Discrimination (PSD)

For Ge detectors, the pulse shape of a signal depends on where the energy is deposited inside the detector. This enables the classification of events into three main types: single site events (SSE), multi site events (MSE), and surface events. As the name suggests, the main difference between SSE and MSE is the number of interactions they do inside a detector. SSEs occur when the energy is deposited in a localized region of approximately 1 mm^3 in the detector. Examples of SSEs include processes such as $2\nu\beta\beta$ and $0\nu\beta\beta$, where both electrons involved in the decay process deposit their energy within this small volume. On the other hand, background events that deposit their energy at well-separated ($\sim$1 cm) and multiple locations in the detector are classified as MSEs, such as multiple Compton scattering of γ-rays. Other background events coming from α or β decay close to the p+ and n+ electrode surfaces are referred to as surface events. The events, located near the n+ (p+) contact, typically exhibit slow (fast) pulse-shape characteristics due to the influence of the electric field. Slow pulses often have incomplete charge collection. The differentiation of surface events and MSE from SSE based on their pulse shapes and time structure is known as Pulse Shape Discrimination (PSD).

In GERDA experiment, three types of HPGe detectors with different geometries were used. These included the coaxial detectors (Coax), Broad Energy Germanium (BEGe) detectors and the newly developed Inverted Coaxial Point Contact (IC) detectors for GERDA Phase II. All of these detectors were fabricated using p-type Ge material and featured a lithium diffused n+ electrode and a boron implanted p+ electrode. To maintain electrical isolation, these electrodes were separated by an insulating groove. The PSD behavior of different detectors depends on their geometry. For example, BEGe and IC detectors exhibit excellent PSD behavior due to their small p+ contact area, which results in a highly pronounced weighting potential. In contrast, coaxial detectors have a different electric field compared to BEGe detectors, with a lower gradient in their weighting potential. Figure 3.2 provides a visual comparison of the weighting potentials and geometries of the detector types used in GERDA Phase II [66].

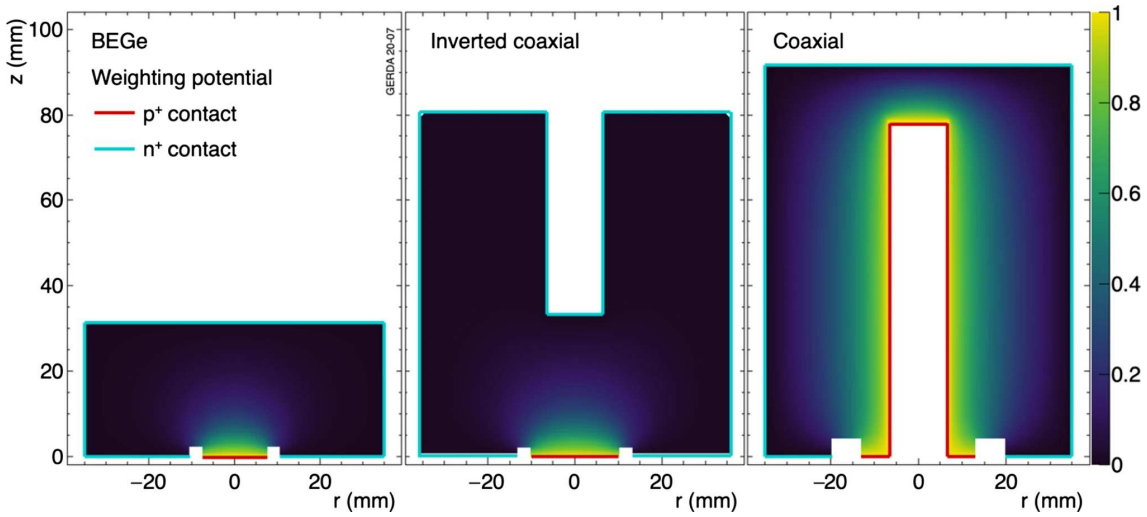

Figure 3.2: Weighting potential and geometry of HPGe detector types (BEGe, IC, and Coaxial) used in the GERDA experiment. Schematic representations of the n+ and p+ contact surfaces are indicated. The BEGe and IC detectors are characterized by a small planar p+ contact, whereas the coaxial detectors are read out through a borehole electrode. Figure taken from [66].

3.3.4.1 PSD Techniques for BEGE Detectors

The pulse shapes recorded from BEGe detectors is shown in the Figure 3.3 for single-site, multi-site and events near the p+ and n+ electrodes. The discrimination is based on the amplitude of the current pulse (A) normalized by the energy (E). The energy corresponds to the amplitude of the charge pulse [66]. The normalized charge pulses are depicted in blue, while the corresponding current pulses are shown in orange in the Figure 3.3. The current pulses show a noticeable variation in their amplitudes across different event types. By comparing the amplitude (A) and the energy (E) using the ratio A/E, it is possible to differentiate between different type of events. For events with a single energy deposition in the detector bulk, the A/E ratio remains constant over energy. The leftmost plot in Figure 3.3 illustrates a visual representation of the charge and current pulse for such an event. Events where energy is deposited at multiple locations in the detector exhibit pulse shapes that represents the superposition of single-site event pulses. The pulse shape of such a multi-site event is depicted in the second plot from the left in Figure 3.3. It is characterized by a smaller A/E value compared to SSE. Events that take place on the surface of the p+ readout electrode, such as the surface α contaminations, exhibit a rapid rise in the charge pulse because of

the strong electric field in this region. As a result, the ratio of A/E is higher compared to SSE. An example pulse from such an event is shown in the third plot from left of Figure 3.3. On the other hand, events involving energy deposition at the high voltage n+ contact, such as β-decays of ^{42}K, generate a current pulse with a smaller amplitude. This is due to the extended dead layer in these regions. The pulse shape of such events is dipicted in the rightmost plot of figure 3.3.

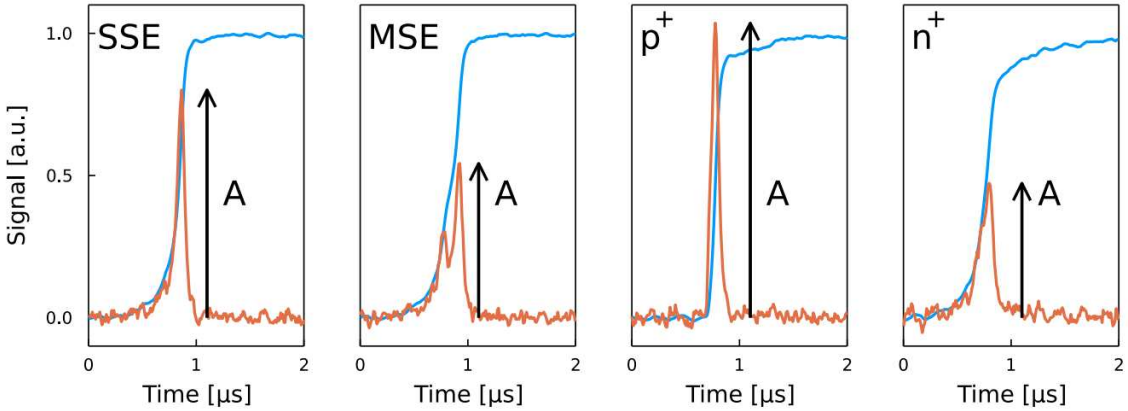

Figure 3.3: Various normalized charge pulses (depicted in blue) for SSE, MSE, and an event at p+ and n+ contacts along with the corresponding current pulses (shown in orange) from a BEGE detector. Arrows indicate the amplitude A of the current pulses. Figure source [66].

Due to the continuous and energy-dependent nature of the A/E spectrum, the differentiation between event types is not always straightforward. To address this, the GERDA experiment introduced an energy-independent A/E classifier (ζ). This classifier is defined as $([A/E]/\mu_{A/E}(E) - 1)/\sigma_{A/E}(E)$, where $\mu_{A/E}$ and $\sigma_{A/E}$ represent the energy-dependent peak position of SSE in the A/E spectrum and width respectively [66]. The A/E spectrum utilized in this equation is normalized to one. It exhibits a distribution with a peak centered around 0 and a standard deviation of 1 for SSEs. To distinguish SSEs from MSEs and n+ surface events, a low cut value of ($\zeta < 0$) is defined. Additionally, a high-side A/E cut of ($\zeta = 3.0$) is chosen for each detector to reject p+ surface events, especially to remove all α events above 3525 keV in physics data [66]. The A/E cuts used in this thesis are determined based on the above-mentioned A/E classifier.

3.3.4.2 PSD Techniques for Coaxial Detectors

For semi-coaxial (Coax) detectors, one of the challenges in pulse shape analysis compared to BEGE detectors is the wide range of pulse shapes exhibited by SSEs from the bulk of the active volume. Given a vast variety of underlying signal shapes, a simple mono-parametric cut such as A/E is not sufficient. In order to address this issue, the GERDA experiment has implemented various PSD methods for Coax detectors. One of the main methods includes multiparameter analysis based on the Artificial Neural Network for MSE (ANN_MSE). It is designed to identify and remove MSE which have typically a longer rise time compared to SSE. The input parameters used for this method are extracted from the rising parts of the charge pulses, such as the time it takes for the pulse to reach different percentages (i.e. 1%,3%,...,99%) of its maximum amplitude in increments of 2%. The time when the pulse reaches 50% of its amplitude serves as a reference [67]. This ANN-based PSD method is conducted using Toolkit for Multivariate Data Analysis (TMVA) implemented in ROOT [68]. This binary classifier takes input parameters and provide a score between 1 (signal-like event) and 0 (background-like event).

Another ANN-based PSD method is used to reject α-induced surface events on the p+ contact. This method utilizes a training sample, consisting of $2\nu\beta\beta$ events that remain after LAr veto cut, along with events exhibiting an energy deposition above 3500 keV [67]. In addition, the rejection of α events is further enhanced by a single parametric rise time (RT: $10-90$) selection criteria. This selection is based on the time difference between the intermediate rise times at 10% and 90% of the maximum signal amplitude [69]. The example of such waveform is shown in the Figure 3.4 . The rise time cut value is carefully optimized in a way that it maximize the acceptance of $2\nu\beta\beta$ events while simultaneously minimizing the oocurrence of α-induced surface events. In this thesis, these PSD techniques have been used for investigation of α events in the muonic induced background.

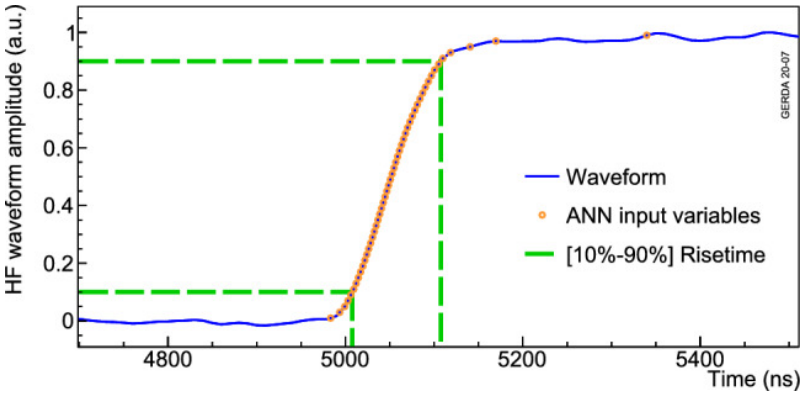

Figure 3.4: A normalized 100 MHz trace (depicted in blue) from a coaxial detector. The 50 input variables used for ANN analysis are indicated by orange circles, while the estimates for the 10-90% rise time are shown with dashed green lines. Image source [66].

Chapter 4

Muon Veto System of GERDA

This chapter provides an overview of the Gerda Muon veto system, including its layout and hardware. It begins with a brief introduction to the veto system and its components, followed by an explanation of the data acquisition system of GERDA. Subsequently, the calibration and monitoring of the system conducted by the author during Phase II+ of GERDA will be presented. The focus of this chapter is to provide details into the hardware and stability of the veto system, while a thorough discussion on the background induced by muons in Phase II and Phase II+ physics data is presented in Chapter 5. The Muon veto is composed of two main parts: the water tank, which is equipped with PMTs to detect Cherenkov light from muons passing through the water, and plastic scintillator panels that cover the cryostat's neck. Further details on these components are explained in the subsequent sections.

4.1 The Cherenkov Water Veto

There were in total, 66 Photomultipliers (PMTs) operated under water inside the GERDA water tank. The PMTs were organized in seven rings within the tank. One ring of six PMTs, was placed in the small volume (2m diameter and $\sim$ 1.35 m height) under the cryostat, known as the Pillbox. Two rings, consists of eight and twelve PMTs respectively were distributed on the floor of the water tank, facing upwards into the main water tank volume. Additionally, four rings, each containing 10 PMTs were placed on the wall of the tank, facing towards the cryostat.

Figure 4.1b shows the arrangement and naming scheme of these PMTs within the water tank. In the figure, the PMTs represented by red crosses, indicate the ones that encountered issues. More details about these defected PMTs can be found in Section 4.5.

In addition, to enhance the detection efficiency of optical photons, the inner wall and floor of the water tank, as well as the outer wall of the cryostat, are covered with a highly reflective foil known as "VM2000" (Daylighting Film DF2000MA) [70]. This reflective foil, on one hand enhances the light yield of each muon due to its high reflectivity and on the other hand, it shifts the predominantly UV Cherenkov photons to $\sim$ 400 nm, where the PMTs are most efficient in detecting light. The sheets of reflective foil have one side covered with an adhesive, which adheres remarkably well to the stainless steel surfaces. Thus the inner walls and floor of the water tank are covered with these adhesive sheets. However, the outer surface of the cryostat, which is coated with the porous insulating material 'Jackodur' (by Jackon), poses a challenge as the foil doesn't stick to this surface easily. To overcome this issue, a nylon rope was tightly wound around the cryostat to prevent the foil from coming off. The optical fibers and HV cables of each PMT are fastened at multiple points with clamps and cable binders. All these cables are lead to a chimney flange located on top of the roof of the water tank. On the outside of the tank, several cable trays connect this chimney flange to a control room on the second floor of the GERDA building. Inside this control room, the data acquisition (DAQ) system and other electronics are housed in a custom muon veto rack. A full coverage of reflective foil gives a beautiful view to the veto. The water tank of muon veto, covered in reflective foil can be seen in Figure 4.1a.

4.1.1 Structure of PMTs

The Photomultipliers (PMTs) used in the GERDA experiment are of the 8" type, specifically the 9350KB/9354KB model from ET Enterprises [71]. These PMTs consist of a vacuum-sealed glass bulb that holds the photocathode. Within the glass bulb, a series of electrodes known as dynodes are located, along with certain focusing electrodes. All these electrodes are connected to an electronics base,

(a)

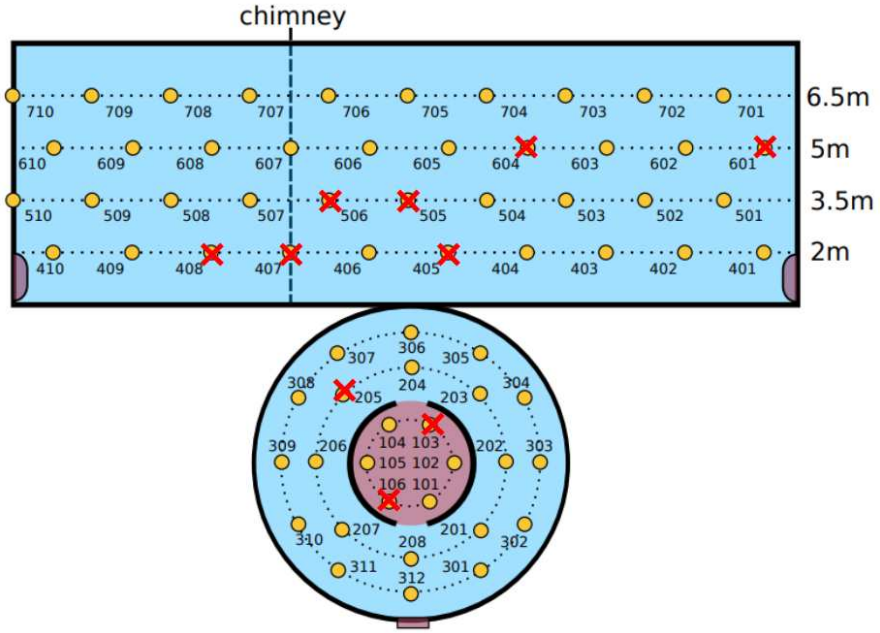

(b)

Figure 4.1: (a) An inside view of the Cherenkov water veto. Photo credit: Prof. Josef Jochum. (b) Distribution and naming of the PMTs inside the water tank. The rectangular part of the figure represents the wall of the tank, while the circular part at the bottom represents the floor of the tank. The smaller region in the middle indicates the Pillbox. The PMTs are arranged in seven rings and are marked with yellow dots. However, the ones marked with red crosses indicate PMTs that either broke or malfunctioned during the lifetime of GERDA. Figure Source [65].

where the voltage divider is located. When a photon strikes the cathode, it releases an electron through the photoelectric effect. Due to the voltage divider, the following dynode carries a positive potential, which accelerates the electron towards it. Upon reaching the dynode, the electron gains enough energy to release

several additional electrons (typically in the order of two to five e^-). Thus, this process of electron multiplication, from dynode to dynode, initiates an avalanche effect, resulting in a current pulse on the anode with a magnitude in the range of some tens of milliamperes and with a duration lasting from 10 to 50 nanoseconds (ns). A schematic view of the PMT encapsulation used in GERDA is shown in Figure 4.2 and the different parts of the encapsulation are explained as follows:

- Each PMT is encased in a stainless steel encapsulation, consisting of a cone attached to a cylindrical part with two fixation holes at the bottom plate. The capsule is made up of low-radioactivity steel by Raff and Grund GmbH.
- The capsule is sealed with a custom-made flexible polyethylene (PET) cap, which was designed to serve as a transparent window to enable the transmission of light to the photocathode. The PET cap is attached to the capsule via a metal ring fixed with screws.
- To hold the PMT in position, the voltage divider or base of the PMT is enclosed in polyurethane (UR5041 by Electrolube) and to provide further water blocking, it is sealed with a silicon gel (SilGel 612 by Wacker).
- An underwater high-voltage coaxial cable (RG213/U by JoWo Systemtechnik) connects the PMT on one end to the data acquisition (DAQ) for the transmission of PMT signals to the DAQ and on the other end to the CAEN (SY1527LC) High-Voltage (HV) supply module via a signal splitter box which provides the necessary high voltage to the PMTs.
- The remaining volume of the PMT capsule is filled with mineral oil (161403 by Sigma-Aldrich) [72]. Each PMT contains approximately 1-2 liters of oil which keeps the optical transition of Cherenkov photons from the water via PET window into the glass of the PMT to the photocathode, as smooth as possible. It minimizes the efficiency losses due to total internal reflections.

4.2 The Plastic Scintillator Veto

Muons passing through the neck of the cryostat may not travel a sufficient distance in either the pillbox or the water tank, and thus may not produce enough

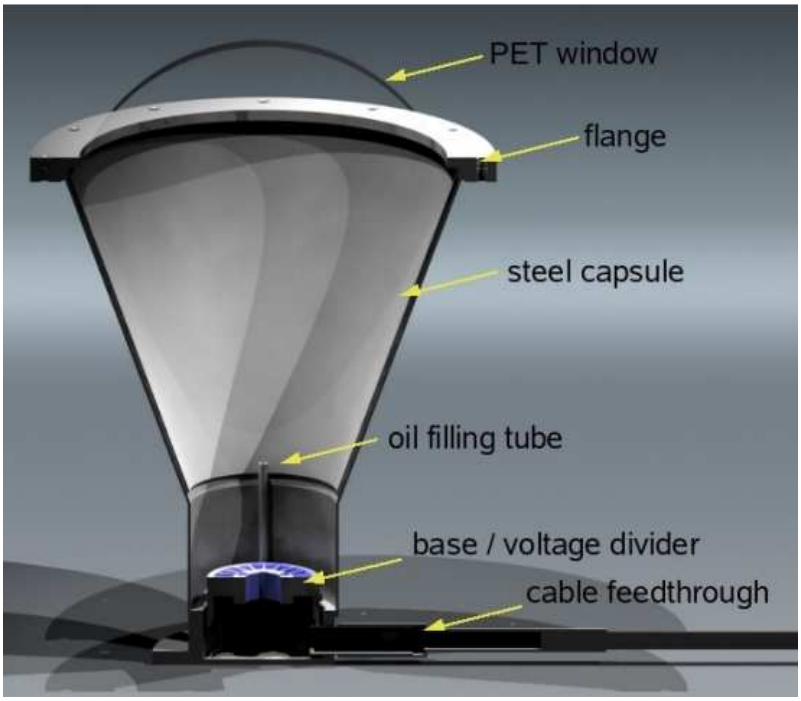

Figure 4.2: Schematic sketch of the PMT capsule [73].

Cherenkov photons to be detected. To cover this potential "blind spot" of the water Cherenkov detector, a specialized system of plastic scintillators was installed on the roof of GERDA's clean room [73]. This arrangement ensures that muons passing through this critical region can be reliably detected. The plastic scintillator veto system is composed of 36 panels, with each panel containing a $3 \times 50 \times 200$ cm^3 plastic scintillator sheet, along with optical fibers serving as light guides on the long sides of the sheet. Additionally, each panel contains an electronics board with a trigger and shaper, alongside a PMT. When a muon passes through, it causes a light in the plastic panel which is then transmitted to the PMT through the optical fibers. These 36 modules are arranged in three layers with each layer consisting of 12 panels, effectively covering a horizontal cross-section area of 4×3 m^2 on the roof of the clean room. Further details on plastic scintillator veto can be seen in [73].

4.3 Data Acquisition (DAQ)

The muon veto data acquisition system (DAQ) of the GERDA experiment is based on a Versa Module Eurocard (VME) crate, which consists of 14 FlashADCs (SIS

3301) from Struck. Each of these FADC houses 8 channels with a sampling rate of 100 MHz and a resolution of 14 bit. Additionally, the VME crate is equipped with a clock, a controller, and a VME-PC. A Digital-to-Analog Converter (DAC) was integrated into the system to serve as a power supply for the calibration system [74]. The calibration system itself consists of 6 pulser boxes (and one spare), equipped with ultra-fast, bright blue LEDs. Five of these LEDs are connected to five diffuser balls, distributed inside the water tank, while the sixth drives the optical fibers that are connected to each individual PMT. Although these optical fibers were initially installed for calibration purposes, they were never used for PMT calibration.

The pulser boxes and the 66 PMT signal splitter boxes, along with four spares, were placed in a custom-made 19" crate. The splitter consists of two RC bandpass filters: a low-pass filter that permits the High Voltage (HV) to pass, and a high-pass filter for the signal. The crate was placed on a rack located directly under the cable trays carrying the HV cables and optical fibers from the chimney flange. The same rack also accommodates a HV crate (SY1527LC) by CAEN which holds six 12-channel HV cards (A1733). Moreover, the six remaining spare card slots within the HV crate served the purpose of operating the muon scintillation panels situated on top of the clean room.

The FADC controller PC runs a DAQ data-taking program that records binary data tag files [75]. These files contain essential information such as run details (e.g., physics run, calibration run, test run), timestamp information, trigger thresholds, trigger multiplicities, etc. Moreover, The PC also be used to power the LEDs for the calibration of the PMTs through the DAC. To ensure data safety, the recorded data was automatically copied to aboveground storage, with backup copies maintained in both Heidelberg and Tübingen. In GERDA, muon data was saved in separate files from the germanium data, hence it doesn't contain any information about germanium data. This allowed the muon data to be available freely for analysis without compromising the integrity of the blind analysis. The entire muon veto set-up can be conveniently controlled and operated remotely.

4.3.1 Hardware Trigger

The DAQ program enables separate trigger conditions for both the Cherenkov veto and the scintillator veto systems. A trigger is generated when a certain number of FADCs, each containing up to 8 channels, record a trace above a specified trigger threshold within a specific time window. The trigger signals from each FADC are then processed through a custom-made 'MPIC' module and read out by the DAQ PC. The muon DAQ consists of 14 FADCs. The distribution of all the PMTs on the FADC channels is shown in Table 4.1. Their configuration and trigger conditions are detailed as follows:

- FADC 1: Used only for calibration purposes and triggers on the MPIC pulser at channel 1 (represented by red color in Table 4.1). The remaining channels in this FADC were kept empty.

- FADC 2-4: Dedicated to the panels with a required multiplicity of 3 panel-FADCs, a trigger threshold at a pulse height of 20 ADC channels, and a trigger window of 60 ns. However, since there were only 4 FADCs (24 channels) available for 36 panels, the best solution was to combine two of the 36 single-panel signals from one layer to one signal. As a result, only 18 channels (6 channels per layer) were left. These six channels were then connected to one FADC each, thus, the scintillation veto system was distributed in a total of three FADCs. These FADCs associated with the panels can be found in Table 4.1, highlighted in yellow. A detailed discussion on the distribution of these panels in FADCs is explained in reference [65].

- FADC 5-14: Used for the Cherenkov PMTs with a required multiplicity of 5 channels. Each PMT has its own dedicated FADC channel, with 6-7 PMTs assigned to each FADC (indicated by light pink color, in Table 4.1). The trigger threshold of each PMT was set at a pulse height of 50 ADC channels, with a trigger window of 60 ns.

To keep the trigger efficiency as high as possible, each FADC gives one trigger only, independent of how many PMTs connected to it are fired, it was also assured that all the neighboring PMTs were placed on the different FADCs. This

ch	FADC: 1	FADC: 2	FADC: 3	FADC: 4	FADC: 5	FADC: 6	FADC: 7
1	Pulser	1/2	13/14	25/26	101	106	105
2	–	3/4	15/16	27/28	307	304	207
3	–	5/6	17/18	29/30	301	310	303
4	–	7/8	19/20	31/32	409	408	407
5	–	∅	21/22	33/34	501	510	509
6	–	9/10	23/24	35/36	604	603	602
7	–	11/12	–	–	706	705	704
8	–	–	–	–	–	–	–
ch	FADC: 8	FADC: 9	FADC: 10	FADC: 11	FADC: 12	FADC: 13	FADC: 14
1	104	103	102	–	–	–	–
2	206	205	204	2203	202	201	208
3	302	312	311	309	308	306	305
4	406	405	404	403	402	401	410
5	508	507	506	505	504	503	502
6	601	610	609	608	607	606	605
7	703	702	701	710	709	708	707
8	–	–	–	–	–	–	–

Table 4.1: Distribution of all PMTs on the 14 FADCs of GERDA muon DAQ [65].

configuration allowed the muon veto system to effectively trigger even for events with spatially less light distribution [76], thus enhancing the overall efficiency of the veto.

As soon as the trigger condition is fulfilled for either the Cherenkov or scintillator veto, the entire veto is read out by the DAQ system. This involves recording 400 data points for each detector with a time resolution of 10 ns (4 μs in total). For an event to be recorded, at least one detector on an FADC must surpass the trigger threshold, and if a certain number of FADCs show a trigger signal within 60 ns, the event is recorded. In the case of a scintillator veto, 3 out of 3 panel FADCs or for the Cherenkov veto, 5 out of 10 Cherenkov FADCs need to surpass the threshold in this time window. Once this condition is fulfilled, the system records the 400 data-point traces for further analysis. The trigger conditions for the GERDA muon veto system were investigated and determined in [76].

4.4 Calibration Procedure of Muon Veto

The muon veto DAQ system has two main modes of operation: the regular run mode for collecting physics data and the calibration mode. In the calibration mode, all the PMTs are calibrated regularly using a set of five custom-made diffuser balls [73]. These balls are filled with a mixture of silicon gel (by Wacker) and tiny glass pearls (S32 by 3M). Each ball contains an optical fiber glued into a small vial with a high concentration of glass pearls. To ensure a controlled and precise light emission, the cladding of the fiber's end is removed, and the fiber is roughened, enabling a unidirectional light emission. Four of these diffuser balls are distributed within the main water tank, while the fifth one is placed inside the pillbox. A schematic representation and a picture of the diffuser ball used in GERDA are presented in Figure 4.3a and 4.3b.

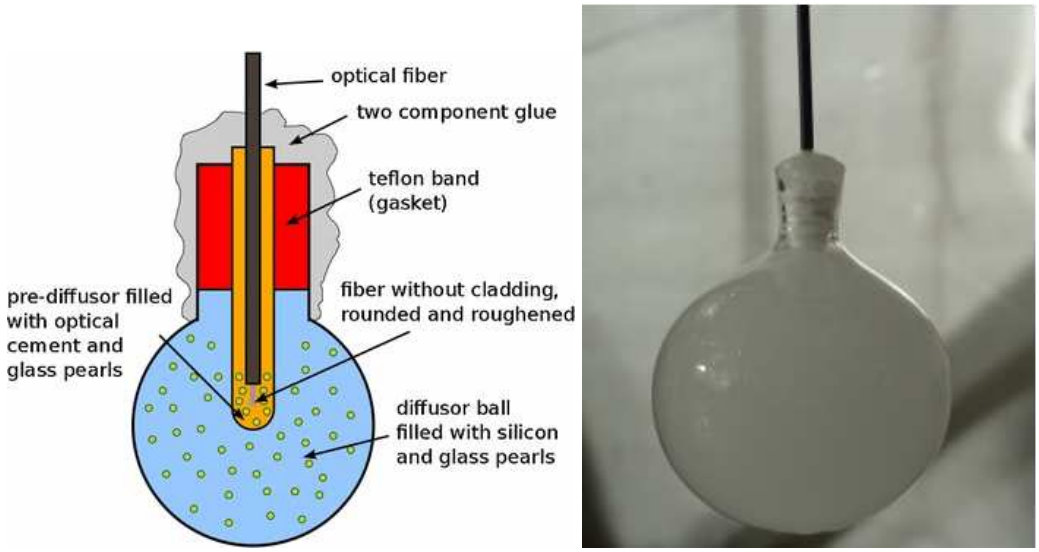

Figure 4.3: (a) Schematic representation of a diffuser ball. (b) Original picture of a diffuser ball [73].

Pulser signals are generated by a pulser in the MPIC module and then multiplied using a CAEN fan-in/fan-out module. These multiple pulser signals are used to power the ultra-fast LED drivers, which in turn illuminate all the diffuser balls inside the water tank. By carefully adjusting the forward voltages of the LEDs, it becomes possible to illuminate all PMTs simultaneously with single photons. This allows us to gather information about the position of the single

photon peak (SPP) of each PMT at the same time. The specific forward voltage values for these diffuser balls and their respective locations inside the water tank can be found in Table 5.4 of [65]. With these settings of the forward voltages, a ratio of one photoelectron (PE) in ten pulser events can be achieved for each GERDA PMT.

The calibrations of PMTs were conducted during the pauses of germanium data taking. The calibration process consists of the following steps: The first step involves turning off the muon data-taking and initializing the calibration process remotely, via ge-gate. This action powers the LED drivers to illuminate the diffuser balls inside the water tank. The calibration data is then recorded for ~ 10 minutes, during which the SPPs of each PMT are measured and stored. The SPP position of each PMT is typically adjusted to a target value of 100 FADC channels. The trigger threshold of the Cherenkov veto is set to 50 FADC channels for each PMT. In the next step, the recorded SPP of each PMT is examined for any deviations from the desired value of 100 FADC channels. If the SPP of a PMT is found to have deviated from the target value, the High Voltage (HV) supply of that specific PMT can be adjusted accordingly to bring the SPP back to 100 FADC channels. In this way, the response of each PMT to single photon illumination is homogenized. In additional steps, the HV supply can be re-adjusted until the desired response is achieved. Fortunately, during GERDA Phase II, the gains of the PMTs show minimal drift over time, hence only a few PMTs needed to be adjusted during each calibration.

Figure 4.4 displays the SPP spectra for the PMTs: 105, 311, and 507 within the water tank. In each spectrum, there is a prominent large peak near zero, known as the "pedestal", which corresponds to the random noise of the PMT when it was not recording any light during the LED pulsing. The peak in the middle of each spectrum represents the SPP of each individual PMT. The pedestal, containing > 10 times more entries compared to the peak, confirms that this central peak indeed corresponds to the SPP, with only minimal contamination from double-photon peak events. For every PMT, there is a clear distinction between the pedestal and SPP, with a peak-to-valley ratio typically ranging from 1.5 to 3.0. Figure 4.4a displays the desired mean value of SPP at 100 FADC channels. Fig-

ure 4.4b and 4.4c are added for comparison, showing peak shifts towards higher and lower FADC channels, respectively. By appropriately adjusting the HV supply for these PMTs, the peak position can be brought back to the target of 100 FADC channels. Figure 4.4d illustrates the PMT resolution in terms of the width of the SPP versus the position of the SPP. The plot shows that both the peak position and standard deviation of the Gaussian distributions show minimal deviation.

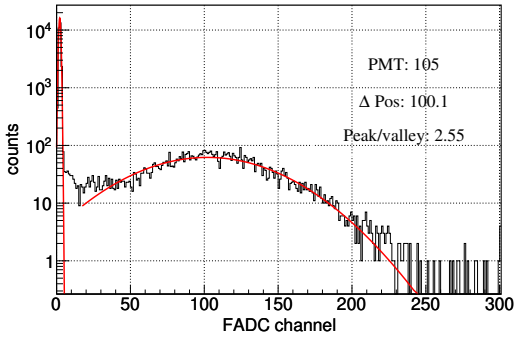

(a) PMT: 105, SPP = 100 FADC ch

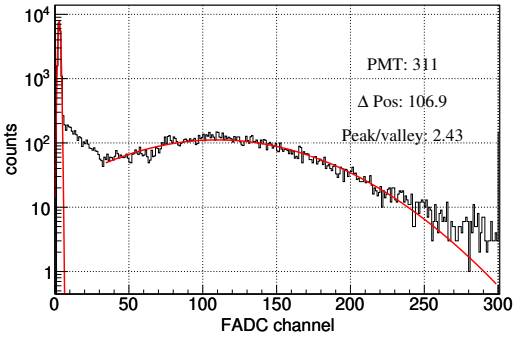

(b) PMT: 311, SPP = 107 FADC ch

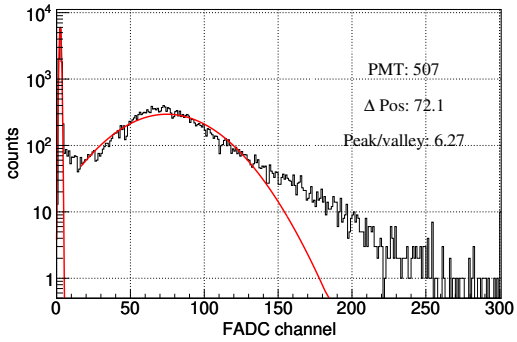

(c) PMT: 507, SPP = 72 FADC ch

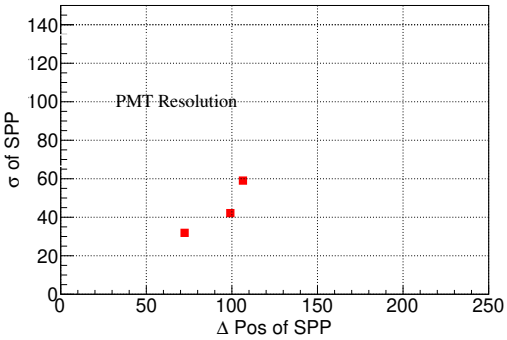

(d)

Figure 4.4: Calibrated SPP spectra of three selected PMTs: (a) PMT 105, (b) PMT 311, and (c) PMT 507. (d) The PMT resolution is presented in terms of the width of the SPP versus the position of the SPP.

4.5 Performance of Muon Veto during GERDA Phase: II

During Phase II and Phase II+, the muon veto recorded a total of 1349 live days of data taking. The duty cycle is shown in Figure 4.5a together with the accumulated

live time (shown as the red line). The major interruption of the DAQ in April 2017 is due to a drainage of the water tank. Other than this, the muon DAQ was only stopped either due to power shortcuts or due to breaks of the germanium data taking in order to perform calibrations and other maintenance work like the upgrade. During the Germanium data taking the muon veto was always fully operational.

The performance of the PMTs used in GERDA is of great interest to ensure the proper functioning of the muon veto system. These PMTs were encapsulated in 2008 and have shown a remarkable level of reliability over time. A PMT is a very dependable detector, known for its long-term stability often remains active for years without any significant deterioration in performance. Since the efficiency of the muon veto relies on the individual performance of each PMT, daily monitoring of the PMT rates has been carried out throughout the data taking. A mean daily rate of 3182 $\pm$ 2 muons was measured in Phase II and Phase II+ which translates into a muon rate of $(3.07 \pm 0.20) \cdot 10^{-4} / (\mathrm{m}^2 \cdot \mathrm{s})$ (neglecting the annual flux modulation). Figure 4.5b shows the daily rate of a selected group of PMTs, representing one PMT from each ring of PMTs, within the water tank. This figure shows the long-term stability of the entire veto system over almost 2.5 years, spanning from July 2018 to February 2020. Overall, there was very little to no change in the individual rate of the PMTs except for only a few PMTs which experienced instability or damage during the operation of GERDA.

During the entire lifetime of GERDA, including Phase I, Phase II, and Phase II+, a total of 10 out of 66 PMTs encountered issues, either by implosion or malfunction. Among these 10 PMTs, 6 had a history of poor performance or had experienced implosions in the past. Two PMTs became non-functional towards the end of GERDA while the remaining two suffered implosion during or after the final water drainage of GERDA in October 2020, despite performing well throughout the data-taking period. The location of these 10 PMTs inside the water tank is indicated by red crosses in Figure 4.1b. The overall mean loss rate of PMTs during GERDA's operation was $\sim$ 1-2 PMTs per year. A brief summary of these 10 PMTs is as follows:

- **PMT 604** (Location: Wall at 5m): Not operational since the beginning of

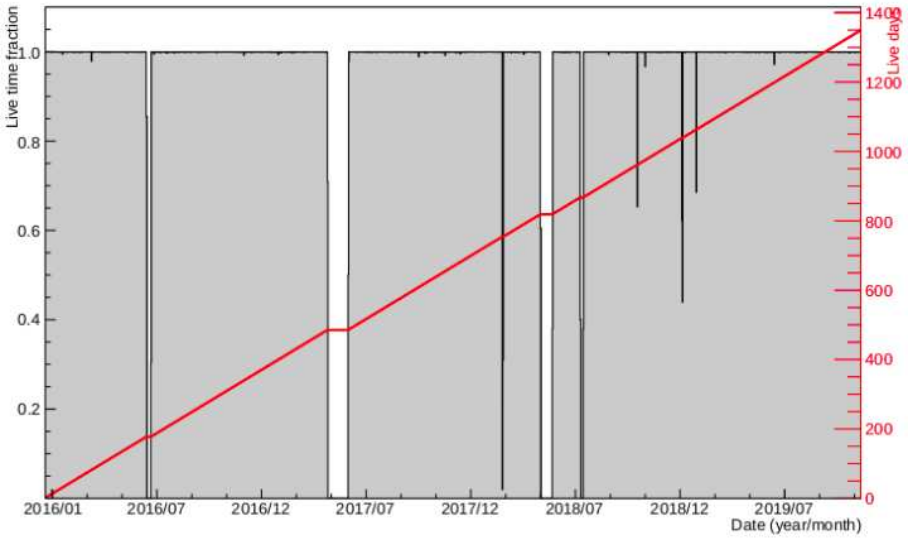

(a)

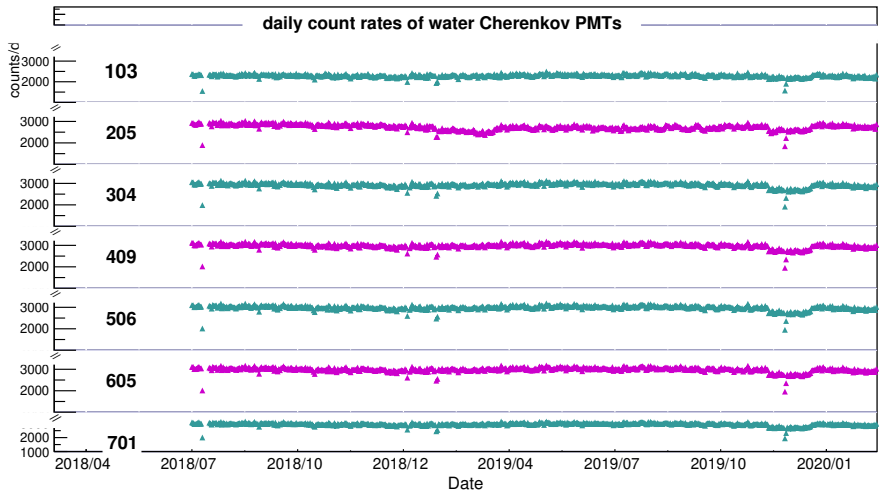

(b)

Figure 4.5: (a) Duty cycle of the muon veto for Phase II and Phase II+ data. The veto lifetime (black) and accumulated live days (red) are indicated. (b) Summary of the daily rate stability from July 2019 to February 2020, for selected seven PMTs located in the water tank. The three-digit numbers on the left side of the plot correspond to the labels assigned to each PMT.

GERDA data taking due to high current (>1 mA) leading to self-shutdown of its HV channel as a precaution ("I-tripping") [65].

- **PMT 106** (Location: Pillbox): Deactivated since the start of Phase I due to current tripping.
- **PMT 405** (Location: Wall at 2m): Exhibited unstable behavior throughout the entire data-taking period.
- **PMT 408** (Location: Wall at 2m): Non-functional since 2016 due to I-tripping.

- **PMT 505** (Location: Wall at 3.5 m): Experienced unstable behavior throughout its operational time.
- **PMT 601** (Location: Wall at 5m): Stopped working in February 2016, briefly switched on in February 2018 but tripped off again.
- **PMT 407** (Location: Wall at 2m): Stopped functioning by the end of 2019 and exhibited instability throughout its operational duration.
- **PMT 205** (Location: Floor, inner ring): Stopped working towards the end of GERDA data taking in February 2020. It worked well throughout its operation until the malfunction which can be seen in Figure 4.5b.
- **PMT 103** (Location: Pillbox): Imploded during or after the final water drainage of GERDA in October 2020. The capsule broke, leading to mineral oil from the PMT spilling into the water. The PMT performed well until the end of data-taking as shown in Figure 4.5b.
- **PMT 506** (Location: Wall at 3.5m): Also imploded during or after the final water drainage of GERDA, with the capsule breaking and mineral oil spilling into the water. It also functioned well throughout its operational lifespan, as shown in Figure 4.5b.

Despite these issues with some PMTs, the majority of the PMTs operated reliably and contributed significantly to the success of the GERDA experiment. As mentioned above, upon opening the water tank in October 2020 after the final data taking of GERDA, it was discovered that both PMTs 103 and 506 had imploded. The Polyethylene (PET) caps of these PMTs ruptured, resulting in the spillage of oil into the tank. While the presence of oil was detectable, the amount of oil in the water was found minimal. Most importantly, the oil used in PMTs was mineral oil, which was not hazardous or dangerous under EU regulations [77, 72]. Nevertheless, as a precautionary measure and to ensure safety, the muon veto system was modified for the LEGEND-200 Experiment. Further details about the repair process and the exchange of the defected PMTs for the LEGEND-200 are thoroughly explained in Chapter 8.

Chapter 5

Muonic Background in GERDA Phase II and Phase II+

Muons can interact in multiple ways with the core of the GERDA Experiment: the Germanium Detector Array. They can either pass directly through the detectors and deposit energy in one or more detectors or they may spallate the nuclei in its surrounding, which can lead to radioactive isotopes in the vicinity of the detectors. In addition, muons could generate free neutrons which can further activate any material in its surrounding and thus produce other potentially radioactive isotopes. This chapter presents a detailed analysis of the direct and delayed muonic-induced background in GERDA Phase II data.

Section 5.1 focuses on the rates of germanium, muon, and muon-germanium coincident events and a method to generate the coincidences. The comparison between the observed muon-Ge coincident rate and the expected random coincident rate in Phase II data will be presented in Section 5.2. Section 5.3 discusses the detailed analysis of prompt muonic background in the GERDA Phase II data, over the whole energy range as well as in the region of interest (ROI). Various techniques, such as waveform analysis, event classification based on event properties, PSD techniques as well as simulation studies have been performed to identify and characterize the residual muonic background. The second half of this chapter, Section 5.4, will cover the analysis of the delayed muonic background in the GERDA Phase II data, which arises from the proton spallation of argon. The entire work presented in this chapter is done by the author of this thesis.

Description of Runs:

The whole GERDA Phase II data is divided into two parts: Phase II (Runs: 53 - 93) before and Phase II+ (Runs: 95 - 114) after the upgrade. GERDA Phase II started collecting physics data taking on 25^{th} December 2015 and in 2018, the setup was upgraded (Phase II+) which involved replacing the natural Ge detectors with a string of enriched Ge Inverted Coaxial (IC) detectors. To ensure impartiality, a blind analysis is performed i.e. the physics data in the $\pm$ 25 keV window around $Q_{\beta\beta}$ were not available for the analysis. Before unblinding the events within the energy range of 2014 to 2064 keV, data selection, quality cuts and other analysis cuts were established.

The work presented in this chapter has been done using the entire Phase II and Phase II+ GERDA muon and germanium data corresponding to a total exposure of 102.3 kg·yr, except for seven germanium data runs (66, 68, 80, 81, 82, 94 and 102) which were excluded from the analysis. All the events with non-physical traces, overflows or test-pulser were also discarded from the analysis.

5.1 Rates of Muon-Germanium Coincident Events

To observe the behavior of events over time, the time difference (Δt) between two subsequent events of Ge, μ, and the coincidence between Ge and μ are calculated for the entire Phase II and Phase II+ data. Events caused by uncorrelated and constant physical effects are expected to have a flat distribution over time. Therefore, the time difference between above mentioned consecutive events should follow an exponential behavior, and the rate can be determined directly from the slope of the distribution. As the two systems (i.e. Ge-DAQ and μ-DAQ) are physically and electronically very stable, any deviation from exponential behavior would indicate some additional effects taking place. The corresponding rate curves are shown in Figure 5.1a, 5.1b and 5.1c. The decrease in Ge trigger threshold starting in run 87 onwards, from 150 keV down to 16 keV, increases the rate of Ge events which can be observed in figure 5.1a. Therefore, based on the varying trigger conditions, the Phase II and Phase II+ data have been split into two separate data sets for this analysis: Run 53 to 85, and Run 87 to 114.

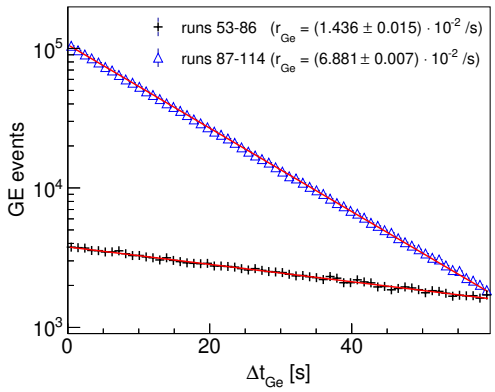

(a) $r_{53-86} = (1.438 \pm 0.015) \cdot 10^{-2} \ s^{-1}$
$r_{87-114} = (6.882 \pm 0.007) \cdot 10^{-2} \ s^{-1}$

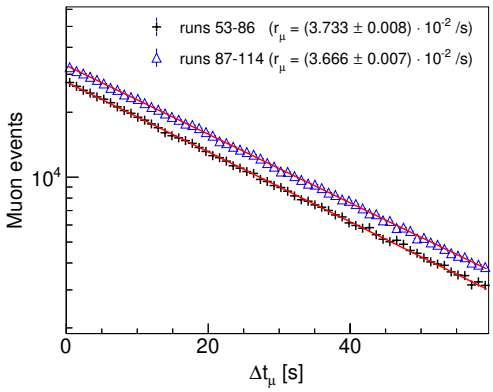

(b) $r_{53-86} = (3.735 \pm 0.008) \cdot 10^{-2} \ s^{-1}$
$r_{87-114} = (3.667 \pm 0.007) \cdot 10^{-2} \ s^{-1}$

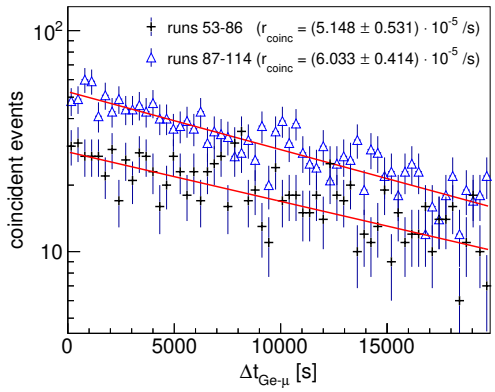

(c) $r_{53-86} = (5.048 \pm 0.576) \cdot 10^{-5} \ s^{-1}$
$r_{87-114} = (6.233 \pm 0.442) \cdot 10^{-5} \ s^{-1}$

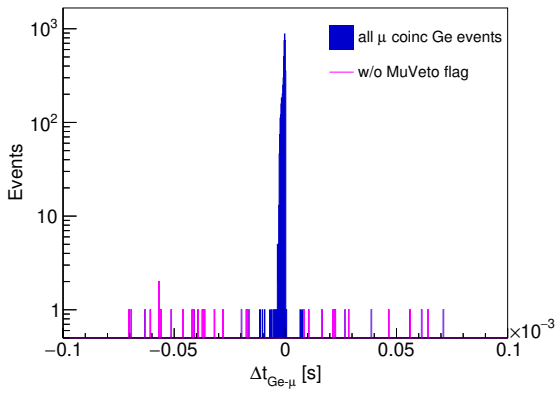

(d) Time-difference between Ge-event at (t=0 s) and muon events in $\pm 80 \mu$s window

Figure 5.1: Time distribution between two subsequent Ge (a), muon (b), and coincidence events (c) for separate datasets: Run 53-86 and Run 86-114. The rates (r_{Ge}, r_{μ} and r_{coinc}) were determined from the slope of the exponential fits. (d) The coincident rate was obtained using the timestamp correlation method within a time window of ± 80 μs.

All those Ge events are considered that fulfilled the selection criteria of having at least one active detector. All the test pulses and baseline events are discarded from the analysis. The muon rate was determined by considering any muon event, where the total amount of light detected was >30 PE or that the panels of veto had triggered in each layer. The muon-Ge coincidence rate was analyzed by comparing the trigger timestamps of muon and Ge DAQ. Both DAQ systems were synchronized every second with the Borexino GPS signal, ensuring a good agreement between them. By defining an acceptance window around the Ge event, coincident events may be studied without being restricted by the

length of the Ge trace. This can later be used to search for delayed coincidences caused, for example, by a muon spallation product. For this analysis, μ-Ge coincident events were analyzed by defining the Ge trigger at t=0 sec and searching for muon events within $\pm$ 80μs window. The resulted time window spectrum is plotted in Figure 5.1d. All the events in a peak i.e. within 2μs centered around zero are accompanied by a muon with a Cherenkov multiplicity of 30 or more and hence are true muons. However, there are a few events scattered along the window (highlighted in pink) outside the muon peak that are not flagged as muons in the Ge-data. These events can be considered as random coincidences. All the curves are fitted with an exponential function and exhibit a good agreement with the data. As the coincident rate is three orders of magnitude lower than the other rates, therefore it suffers from lower statistics. The rates are calculated from the slope of their respective fitted curves.

5.2 Random Coincidences

The random coincidence rate (r_{rand}) between Ge and muon veto can be estimated by using the product of individual rates of the detectors and a time window of muon trace, i.e. $\pm 10\mu s$ (in this case) as shown in the equation 5.1. By taking into account the germanium and muon rates from figures 5.1a and 5.1b, the random coincidence rate in the data-set 53 to 86 are calculated as

$$r_{rand} = r_{Ge} \cdot \Delta t \cdot r_{\mu} \tag{5.1}$$

$$r_{(rand,\ 53-86)} = (0.0144 \cdot s^{-1}) \cdot (20\mu s) \cdot (0.0374 \cdot s^{-1})$$

$$r_{(rand,\ 53-86)} = 1.0742 \cdot 10^{-8}\ s^{-1} \tag{5.2}$$

Similarly for data-set 86 to 114, the random coincidence rate is found to be

$$r_{(rand,\ 87-114)} = (0.0688 \cdot s^{-1}) \cdot (20\mu s) \cdot (0.0367 \cdot s^{-1}) \tag{5.3}$$

$$r_{(rand,\ 87-114)} = 5.0473 \cdot 10^{-8}\ s^{-1} \tag{5.4}$$

By comparing these random coincidence rates with their respective observed Ge-muon coincidence rates from section 5.1 i.e. $(5.048 \cdot 10^{-5} s^{-1})$ for data-set 53 to 86 and $(6.233 \cdot 10^{-5} s^{-1})$ for data-set 87 to 114, it can be concluded that the

observed coincidence rates for both data-sets are dominated entirely by physical events and not accidental random coincidences.

5.3 Prompt Muonic Background

In order to determine the muonic-induced background in the whole GERDA Phase II and Phase II+ data, a timestamp correlation method with a small window of $\pm$ 10μs around the Ge timestamp is used. There are a total of 4879 muon coincident events with energy deposition in enriched HPGe detectors (^{enr}Coax, ^{enr}BEGE and IC) with a Ge multiplicity (M $\geq$ 1) of one or more detectors. The Ge-energy spectrum of these muon coincident Ge events is shown in the figure 7.1a with respect to the different selection cuts. Since muons are most likely to deposit energy in more than one Ge detector, these muon-induced events can be vetoed by the additional detector-AC cut (M=1) which filters out 53.8% of the total events. Even though 2.9% of the total muon-induced events are untagged by the scintillation light in the LAr veto, the LAr veto nonetheless enhances the μ rejection power of the muon veto. Most of these events (marked in red in Figure 7.1a) that escaped detection through LAr veto mainly occupy the low energy part of the spectrum i.e. far below the region of interest (ROI). Although these events do not contribute to background at $Q_{\beta\beta}$, they are still of great interest as they could potentially be neutron events. The detailed analysis of these remaining background events is discussed in the next section 5.3.1. However, due to the absence of LAr veto trigger independent from the Ge trigger in GERDA, no clear muon identification in the LAr veto can be determined. Therefore, the muons that are not tagged by the muon veto system can not be verified by the LAr veto.

Figure 5.2b shows the muonic-induced background w.r.t to the above-mentioned cuts in the ROI which corresponds to the energy range of 1930 - 2190 keV, excluding $\pm$ 5 keV around the two known 2104 keV (^{208}Tl) and 2119 keV (^{214}Bi) γ-lines. The blinding window of $\pm$ 25 keV around $Q_{\beta\beta}$ is also omitted from the analysis. The advantages of the muon veto system are reflected in the significant reduction of the background index in the ROI (from total μ-Ge coincident events) that

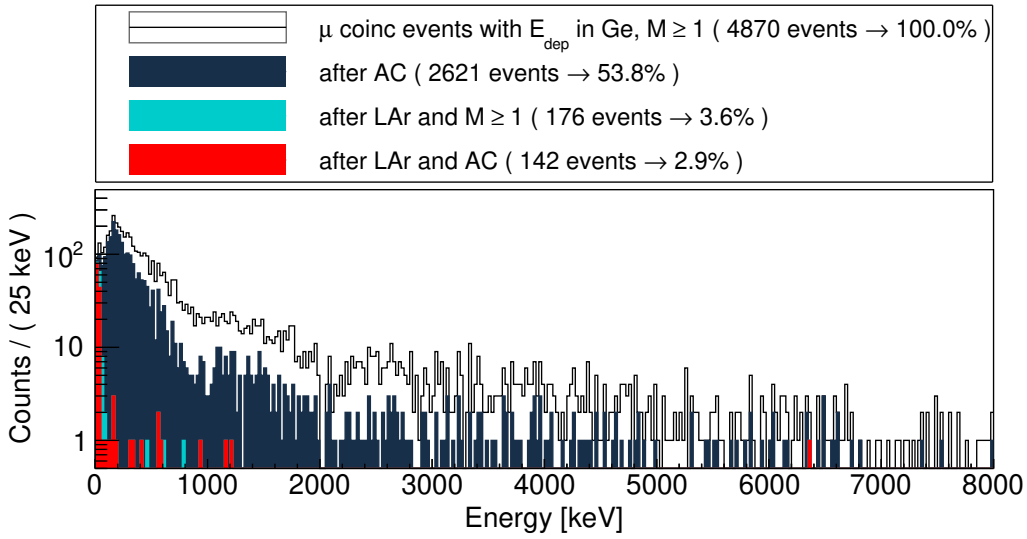

(a)

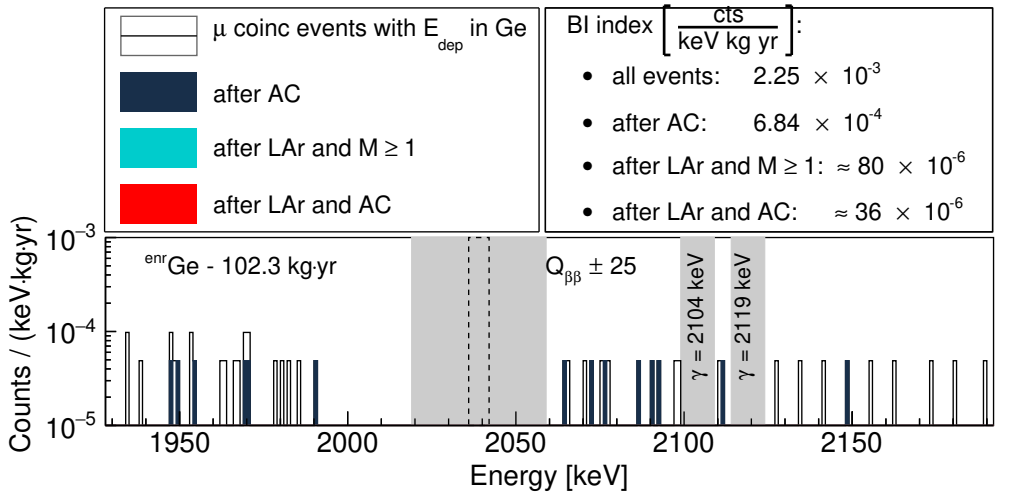

(b)

Figure 5.2: (a) Energy distribution of muon-induced background over the entire energy range under the assumption of various cuts i.e. M $\geq$ 1, After AC (M=1), After LAr veto plus M $\geq$ 1 and After LAr veto plus AC cut. (b) Represents the energy distribution of muon coincident Ge events in the ROI. Blinding window of $\pm$25 keV around $Q_{\beta\beta}$ and $\pm$5 keV around two γ-lines are omitted from the analysis.

would have led without the muon veto to a contribution of

$$2.25 \cdot 10^{-3} \text{ counts}/(\text{keV} \cdot \text{kg} \cdot \text{yr}) \tag{5.5}$$

Also, it can be observed from the figure 5.2b that none of the muon events with (M=1, no LAr veto) were observed in the ROI in Phase II data. Nevertheless, to estimate the background index caused by such events, the same spectrum is assumed for the (M=1, muon veto) events with and without LAr, from the total

energy spectrum. This allows for scaling down the events with LAr in the ROI as an estimate for the events without LAr in the ROI. Based on this assumption, a reduced background index of

$$\sim 36 \cdot 10^{-6} \text{ counts}/(\text{keV} \cdot \text{kg} \cdot \text{yr}) \tag{5.6}$$

is calculated for events with selection cuts of M=1 and no LAr veto.

5.3.1 Investigation of Residual Muonic Background

As shown in the figure 7.1a, there are in total 142 remaining Ge-muon coincidence events that escaped detection through detector-anticoincidence (AC) and scintillation light in liquid argon (LAr) veto cut. These events are considered a dangerous muonic background in such a rare event experiment and deserve a closer examination. Most of these events lie in the lower energy part of the spectrum, except one event, which is located at $\sim$ 6 MeV. To study these events in detail, the following characteristics are taken into account. The first step was to check the pulse shape of these events which can be seen in the following section 5.3.1.1.

5.3.1.1 Waveform Analysis of the Events

To investigate, if these events are really physical events, all the waveforms of these 142 events have been checked. Figure 5.3 shows the traces of some of these events at low and high energies. The rest of some of the waveforms are placed in Appendix A. Approximately 40 out of 142 events appear to be non-physical events and have energies less than 80 keV. Two of these non-physical waveforms are displayed in figure 5.3a and 5.3b which show sharp spikes due to high voltage discharges. Apart from that, all the events are identified as having a physical trace and have fulfilled the definition of standard Ge events. Although some of the events exhibit traces with a lot of noise in them as shown in figure 5.3c, 5.3d and it is tough to extract parameters like rise time or AoE, from them but they are still classified as physical traces. The event at 6357 keV has a very promising waveform with a clear exponential decaying tail because it lies at the high energy where electronic noise is significantly reduced. This waveform can be seen in figure 5.3f. On closely examining all the waveforms, it can be confidently concluded

that 72% of all the events are real events and require further investigation. Furthermore, the majority of the waveforms at $E < 80$ keV are either non-physical or have a lot of noise in them. None of the events above 80 keV exhibit non-physical behavior. In order to check if there are any physical explanations for events above and below 80 keV energy, a dedicated analysis has been done in section 5.3.1.5.

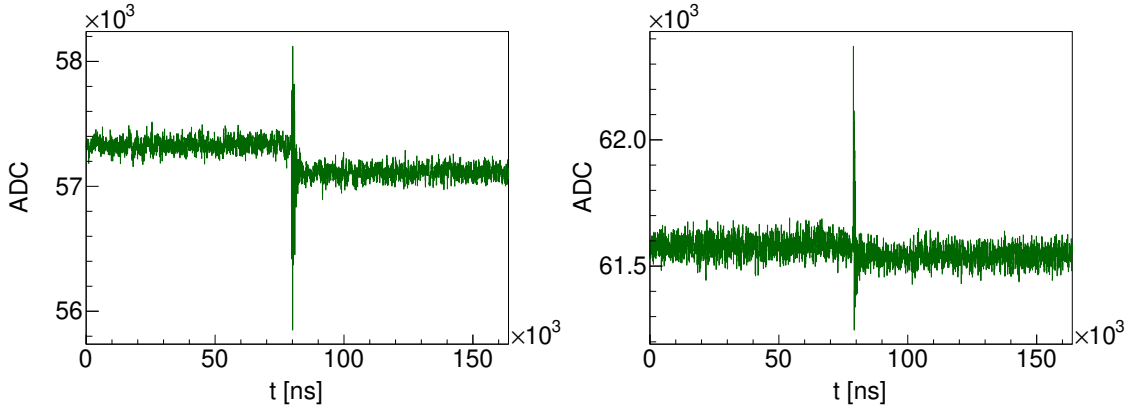

(a) Waveform at Energy = 6.0 keV

(b) Waveform at Energy = 27.2 keV

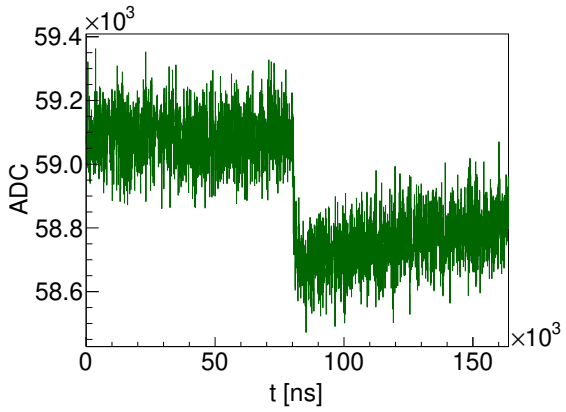

(c) Waveform at Energy = 36.7 keV

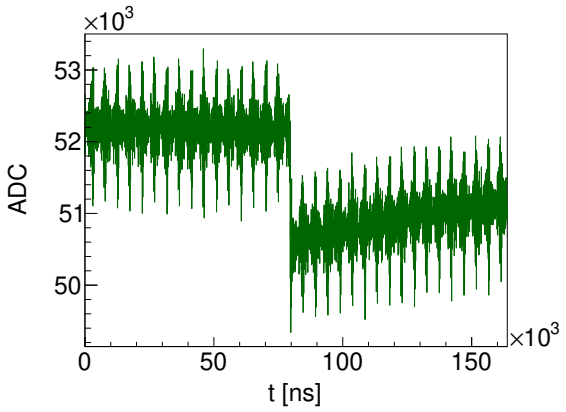

(d) Waveform at Energy = 184.7 keV

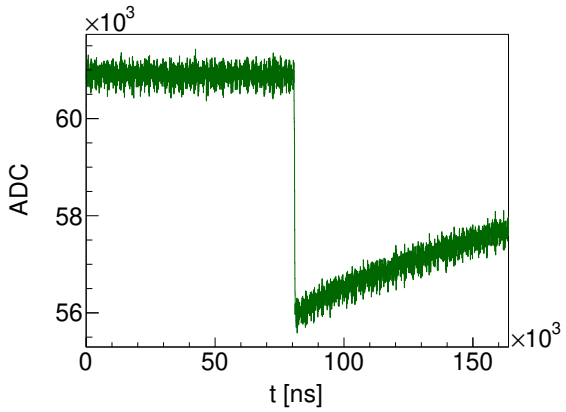

(e) Waveform at Energy = 576.4 keV

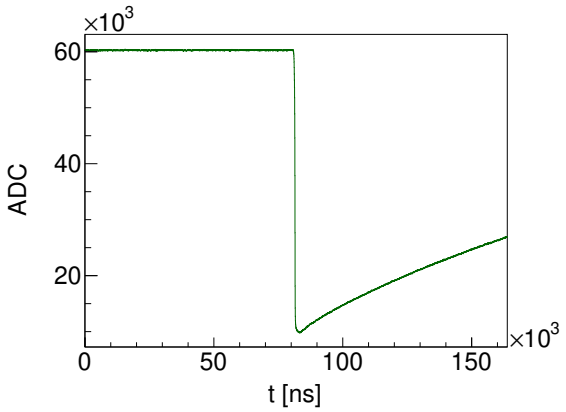

(f) Waveform at Energy = 6357 keV

Figure 5.3: The low-frequency 160 μs long traces recorded for HPGe detectors. (a) and (b) represent non-physical traces with sharp spikes showing High Voltage discharge. (c) and (d) are the physical events but contain a lot of noise in them. (e) and (f) are the standard Ge trace with a clear exponential decaying tail.

5.3.1.2 Comparison between Random and Muon-Ge Coincidences

In addition to examining the waveforms of the above mentioned 142 events, it is also important to investigate whether these events are genuine μ-Ge coincidences or only random coincidences. To determine this, we need to recalculate the rate of random coincidences using equation 5.1 while taking into account the selection cuts of single-detector events (M=1) and the After LAr veto cut on the Ge rate. As a result, the recalculated Ge rate r_{Ge} (M=1, After LAr) for data-set 53-86 was found to be (0.014 s^{-1}), while for data-set 86-114, it was determined as (0.069 s^{-1}). Hence, considering these Ge rates along with the muon rates from section 5.2, the random coincidence rate for data-set 53 to 86 was calculated as (1.1×10^{-8} s^{-1}), and for data-set 86 to 114, it was found to be (5.0×10^{-8} s^{-1}). So in total, only ~ 7 random coincidences are expected among these 142 events throughout the whole data-taking period of 1349 days (Phase II & Phase II+). This observation clearly indicates that the majority of these events are physical events and not accidental random coincidences.

5.3.1.3 Classification of Events Based on Event Properties

These events can be further classified based on their event properties such as the correlation between different observables (i.e. PMT multiplicity vs. $\Delta t_{Ge-\mu}$ and Energy) as demonstrated in Figure 5.4, as well as, the A/E and rise time characteristics of these events as presented in the following subsection. For example, Figure 5.4a displays the timing information of muon events when they arrive in Ge trace. As discussed in section 5.1, muon events that occur within 2μs of the germanium trace are due to the direct energy depositions by muons and it can be seen from the figure 5.4a that most of these events lie within 2-3 μs of the germanium event. Furthermore, Figure 5.4b shows that all these events share a common feature of having a high Cherenkov muon veto multiplicity of around 60 PMTs, with very few below 30 PMTs, despite their low energies. Hence, these events can generally be considered as true muon events.

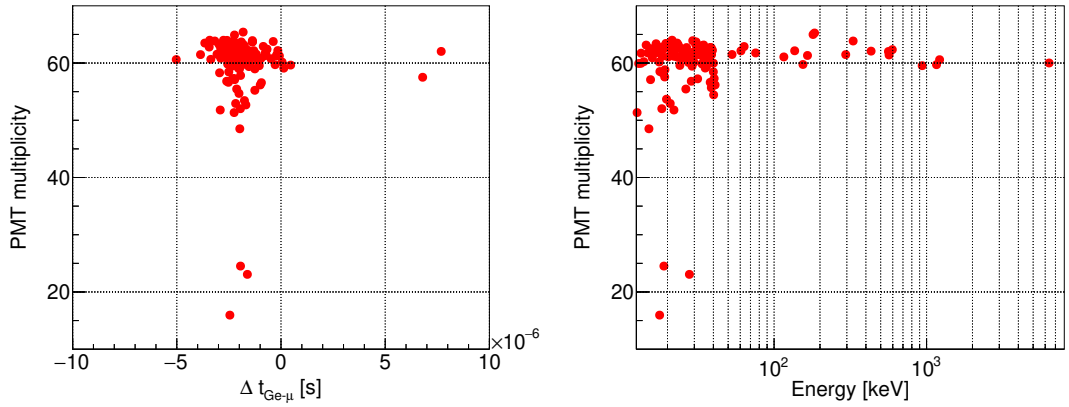

(a) PMT multiplicity vs. $\Delta t_{Ge,\mu} = \pm$ 10 μs

(b) PMT multiplicity of 142 muon events

Figure 5.4: Correlation of PMT multiplicity with the (a) time difference between Ge-muon coincident events and (b) versus energy.

5.3.1.4 A/E and Risetime Classifier of the Events

As discussed in section 3.3.4, in the pulse shape analysis, the BEGE and IC detectors are treated separately from the coaxial detectors due to their different geometries. When analyzing the pulse shape of BEGE and IC detectors, a single parameter known as A/E is used to classify background events. Here A refers to the maximum current amplitude and E represents the total energy. Based on the A/E parameter, events can be categorized as either SSE (normalized A/E $\sim$ 1), MSE and n+ surface events (A/E $<$ 1), or p+ surface events like α particles (A/E $>$ 1).

The corrected and normalized A/E distribution of muon coincident events are plotted against their energy as shown in Figure 5.5a. The figure shows that most (81 out of 142 events) of the events at low energies have A/E values greater than 1, which indicates that the majority of these events occur near p+ contact. About 50 out of 142 events exhibit A/E values less than 1, indicating multi-site events and only a few events (11 out of 142 events) have A/E values of $\sim$ 1. As described in section 3.3.4.2, events that deposit energies above 3.5 MeV and exhibit low rise time values are generally associated with α-decays. Therefore, the event at 6357 keV energy shall be examined carefully. To analyze the rise time characteristics of these events, the distribution of rise time 10-90% classifier for Ge-muon coincident events is plotted as a function of energy, as depicted in figure 5.5b. It can

be observed that the majority of events, particularly those with energies below 80 keV, exhibit a rise time below 5 ns. This suggests that these events have very fast pulses, making it challenging to determine their nature, based only on the rise time information. The remaining events are spread across the rise time range of 100 to 900 ns. Further analysis and investigation are required to gain a deeper understanding of these events and their underlying processes.

As A/E approach and its associated veto flags (e.g. isAoEveteod) have proven to be more useful in distinguishing between different types of events for BEGe and IC detectors compared to coaxial detectors. Therefore, in GERDA, an alternate technique called Artificial Neural Network for MSE (ANN_MSE) is used to distinguish between SSEs and MSEs in coaxial detectors. This technique uses different rise time amplitudes of the charge pulse as input parameters as elaborated in section 3.3.4.2. The rise time is fully integrated into GERDA data production, starting with cycle v03.03. The classifier based on the 10-90% rise time along with the PSD flags (i.e. psdFlag_risetime1090 and psdFlag_ANNmse) are implemented to identify and remove α-induced events from coaxial detectors and are available in the tier-4 files. As PSD techniques strongly depend on the energy deposition of events in specific types of detectors, therefore it is important to determine which event has deposited energy in which detector. In order to accurately determine the association of events with specific detectors, the energy spectrum of residual muon-Ge coincident events is divided based on their energy deposition in the corresponding detector as shown in figure 5.5c.

This division allows for reliable conclusions regarding the event at 6357 keV energy. The upper plot in figure 5.5c displays the combined energy spectrum of ^{enr}BEGE and ^{enr}IC detectors, while the bottom plot shows the energy deposition exclusively in ^{enr}Coax detectors. Out of the 142 muon-Ge coincident events, 94 events, including the event at 6357 keV, exhibit energy deposition in ^{enr}BEGE and ^{enr}IC detectors, while the remaining 48 events occur in ^{enr}Coax detectors. The figure also depicts the classification of these events, based on the above-mentioned PSD flags. The black dots represent events that have been removed by the corresponding PSD flags, while the red dots indicate the events surviving all cuts. It can be observed that 26 events, including the 6375 keV event, in BEGE detectors,

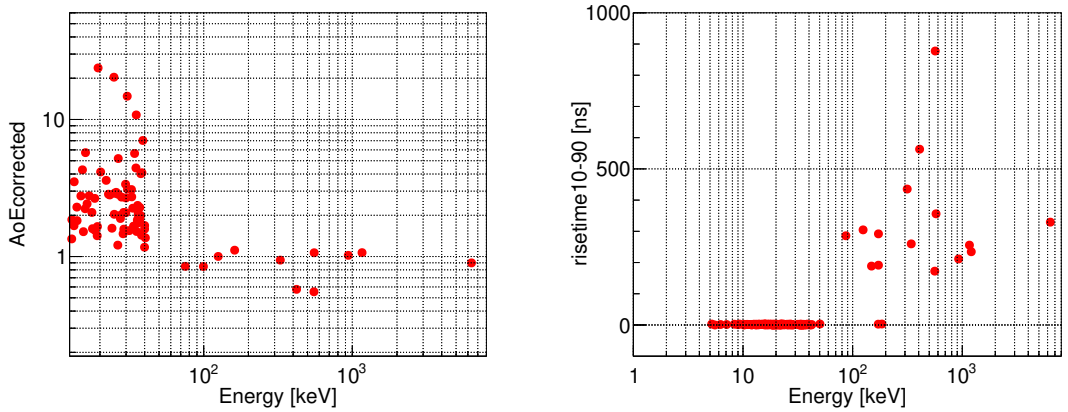

(a) (b)

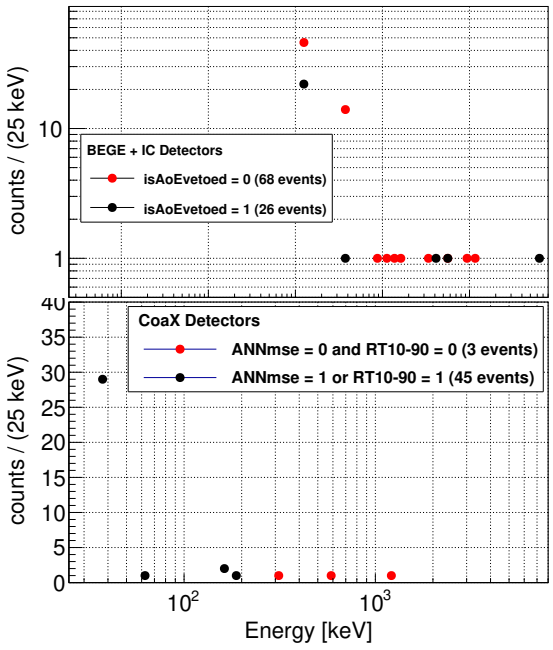

(c)

Figure 5.5: (a) Corrected and normalized distribution of the A/E parameter for Ge-muon coincident events. (b) Distribution of the rise time 10–90% classifier for these events. (c) Detector-wise classification of Ge-muon coincident events with energy deposition in ^{enr}BEGE and ^{enr}IC detectors (Upper plot) and in ^{enr}Coaxial detectors (Bottom plot). Events rejected by PSD flags (i.e. AoEvetoed, ANNmse, and rise time 10-90%) are marked with black dots, while events that survived all cuts are shown in red.

are rejected by the A/E veto, suggesting that these events are either multi-site events or caused by an α event. The classification of events in coaxial detectors based on the ANNmse and rise time criteria is also presented in the bottom plot.

5.3.1.5 Re-Analysis of Random Coincidences with Energy Cut at 80 keV

After examining the waveforms, A/E and rise time distributions (see Figures 5.3, 5.5a, 5.5b) as a function of energy for all (Multiplicity=1, muon vetoed, After LAr) events, a clear difference in the behavior of events with E $<$ 80 keV and E $>$ 80 keV can be observed. If the cut at 80 keV energy effectively reduces the number of events in a way that it is consistent with random coincidences, it would indicate that the events above 80 keV are mainly random coincidences, leaving only real coincidences at lower energies. This would indicate that a muon veto may not be necessary for the upcoming LEGEND experiments. However, this hypothesis needs to be tested by re-analyzing the Ge event rate and thus random coincidence rate as described in Section 5.3.1.2 with an E $>$ 80 keV on the Ge data.

After applying the energy cut of E $>$ 80 keV, only 17 (Multi=1, muon vetoed, After LAr) events remained, and the germanium event rate dropped to (0.014 s^{-1}) for runs 53-86 and (0.040 s^{-1}) for runs 87-114. Using Equation 5.1, the number of random coincidences with the respective Ge rates (after $>$ 80 keV cut) is calculated to be $\sim$ 5 events in the whole Phase II and Phase II+ data (lifetime = 1349 days), which is significantly lower than the total number of remaining events. This indicates that even after E $>$ 80 keV cut, the remaining events are not compatible with random coincidences alone, suggesting that we still need a muon veto in the next generation of LEGEND Experiments.

However, the presence of these low-energy events in the spectrum that are untagged by the LAr veto raises the question of whether these events are caused by neutron interactions. Neutrons, being nuclear recoils, typically exhibit lower ionization yield and low momentum transfer compared to other types of interactions. This characteristic behavior of neutrons may provide a possible explanation for the observed untagged low-energy events. Thus, Section 5.3.1.6 focuses on a simulation study of these events to determine if they can indeed be attributed to neutron interactions.

5.3.1.6 Simulation Study of Residual Muonic Background

In order to investigate these events, Monte Carlo (MC) simulations have been performed using Geant4-based [78] MaGe simulation framework [79], which has

been jointly developed and maintained by the GERDA and MAJORANA [49] collaborations. The GERDA Phase II implementation possesses all the significant components of the experiment, as well as the rock surroundings of Hall A at Laboratori Nazionali del Gran Sasso (LNGS). The simulations are performed with MaGe compiled against Geant4 version 10.5. In Geant4 terminology, a physics list is a collection of various physics processes that are applied to specific types of particles. These physics processes are designed to accurately model the interactions and behaviors of particles within different energy ranges. In this work, the default physics list of MaGe, known as QGSP_BERT_HP of Geant4 is used, which contains a range of physics processes tailored for different energy realms. For instance, for inelastic interactions involving nucleons and pions, the simulations utilize different modeling approaches depending on the energy of the particles. Specifically, the theory driven Quark-Gluon String (QGS) model is used for interactions above 20 GeV, while the Fritiof (FTF) model is used for interactions between 10 and 20 GeV. Below 10 GeV, the simulations employ the Bertini cascade (BERT) model. To accurately describe interactions of neutrons across a wide energy range, i.e. from below 20 MeV down to thermal energies, the High-Precision data driven models known as NeutronHP are used which are based on the evaluated ENDF/B-VII data libraries [80], ensuring precise representation of neutron interactions throughout the energy spectrum.

According to [81], the neutrons produced in the muonic interactions that can potentially be captured by Ge, happen mostly inside the Liquid Argon (LAr). Hence, the kinetic energy spectrum of neutrons, simulated at the position of LAr has been used as an input in this simulation, as shown in Figure 5.6a. This energy spectrum is obtained by using MC simulation of muons striking the GERDA setup using MUon Simulations UNderground (MUSUN) package [82]. To investigate the behavior of neutrons within the experimental setup, a total of $2 \cdot 10^8$ neutrons were generated within a 30 cm diameter surrounding the Ge-detector array. After scattering down in energy, neutrons eventually deposit their residual energy within the Ge-detectors of the GERDA setup. This deposition of energy by neutrons inside the Ge detectors is then recorded and stored in the output for further analysis. To examine the effects of neutron interactions in the LAr medium,

the energy depositions in the Ge detectors are simulated both with and without considering their energy deposition in LAr. The sum of the energy deposition over all Ge detectors has been constructed and normalized to 1. In order to account for the quenching effect inherent in the Ge detector material, a quenching factor of 3.0 is applied to the energy spectrum, shown in the figure 5.6b. This simulated energy spectrum has been compared to the muonic-induced background in Ge detectors as depicted in figure 7.1a, both with and without energy deposition in LAr.

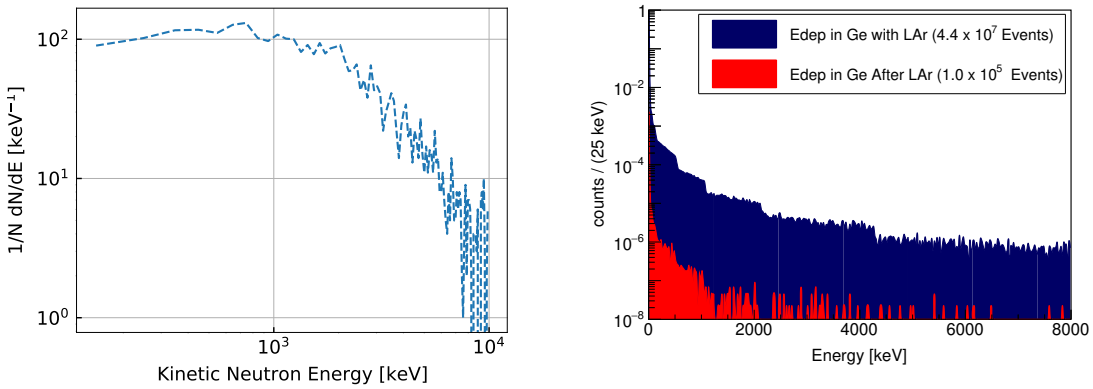

(a) **(b)**

Figure 5.6: (a) Neutron Input Spectrum simulated at the position of LAr in GERDA setup. (b) A simulated spectrum of neutron energy deposition in HPGe detectors both with and without energy deposition in LAr.

Figure 5.6b shows that 22% (4.4×10^7 events) of all the generated neutrons deposited energy in the Ge detectors with LAr. Only 0.1% (105761 events) of the total neutrons ended up depositing energy in the Ge detectors without any energy deposition in LAr. In order to compare these simulated events with the experimental data, it is necessary to estimate the number of neutrons based on the neutron flux within a lifetime of GERDA Phase II. The number of measured neutron-induced events N can be expressed as the product of the neutron flux (Φ), the surface area of the cryostat cylinder (A), and the data-taking time of GERDA Phase II (t), i.e.,

$$N = \Phi \times A \times t \tag{5.7}$$

Here, the neutron flux (Φ) at the position of the HPGe detector array is calculated

to be 1.6 $m^{-2} \cdot h^{-1}$ [81]. The surface area of the cryostat cylinder (A) is determined as 106 m^2 and the data-taking time of GERDA Phase II (t) spans 1349 days. By considering these parameters, the number of neutrons passing through the cryostat over the entire lifetime of GERDA Phase II is calculated to be 5.5×10^6. Similarly, the number of neutrons passing through a 30 cm sphere surrounding the Ge array during the entire Phase II lifetime is estimated to be 5.8×10^4. After normalizing the calculated events with the above-mentioned neutron flux passing through the 30 cm sphere, the expected number of neutron events depositing energy in the Ge detectors without any interactions in LAr is calculated to be 30.9 events. In comparison, the experimental data shows the remaining 71 such events (M=1, no LAr) after PSD cuts, which roughly aligns with our expectations. The comparison of events that deposited energy with and without the presence of LAr, both from the data and the Monte Carlo (MC) simulation, is summarized in Table 5.1. As discussed in section 5.1, the entire Phase II data is divided into two datasets based on the Ge-trigger threshold. The energy threshold of 150 keV (runs: 53 - 86) and 16 keV (runs: 87 - 114) has also been applied to the simulated energy spectrum, allowing for a comparison with the relevant events observed in the data sets. The details of these events are also presented in Table 5.1.

	Without LAr		With LAr	
	GERDA Runs	MC	GERDA Runs	MC
Neutrons ended up in Ge	71	30.9	2621	12896
After threshold of 16 keV	54	0.66	1767	226
After threshold of 150 keV	8	0.23	1303	83

Table 5.1: Comparison of Events with and without Liquid Argon (LAr) in Monte Carlo (MC) Simulation and Experimental Data.

The analysis reveals a somewhat resemblance between the number of events obtained from the MC simulation without LAr and the number of μ-Ge coincident events in the data before implementing any energy threshold cuts (i.e., MC = 30.9 and GERDA Runs = 71 as shown in Table 5.1). This suggests that these events may be attributed to neutrons. However, upon applying the respective energy threshold cuts to the data and MC, a significant difference emerges be-

tween the events from MC and those observed in the data. This difference could arise because the simulation only accounts for individual neutrons and did not consider the likelihood of neutrons occurring in clusters after muons. Therefore, conducting a comprehensive simulation that assumes the presence of approximately 10 or 50 neutrons together might yield a different outcome (i.e., perhaps the MC simulated events would match the events in the data after threshold cuts). Nevertheless, conducting such a full shower simulation was beyond the scope of this thesis, though it remains a useful work for future investigation.

5.4 Delayed Muonic Background

In-situ production of radioactive isotopes by cosmic muon interactions may generate a non-negligible background for deep underground rare event searches. In such low count-rate experiments, the amount of cosmogenically produced isotopes found in the experiment is of great interest. Direct interaction of muons, when comparing the different DAQ systems of Ge and muon veto, has been observed to occur within a few microseconds. However, cosmogenically produced isotopes pose a different challenge. For example, muon at the LNGS possesses a sufficiently high energy of 270 GeV, which has the ability to shatter a nucleus on its way, via spallation. This process generates free neutrons and protons, which can further activate nearby nuclei, leading to the production of additional radioactive isotopes in the setup materials (water, LAr, and Ge-detectors). These spallation products undergo decay with their own characteristic half-life and might not decay within a coincidence window for a clear muon veto flag. However, if the half-life of the particular isotope is too long, it will be difficult to establish any correlation between the delayed decay of an isotope and its responsible muon.

Certain isotopes such as ^{38}Cl, ^{39}Cl, ^{24}Na, ^{28}Mg, ^{29}Al, ^{22}Na, ^{27}Mg and so on, are created through the proton spallation of argon [83]. These isotopes have higher probabilities of being produced from argon. In the GERDA experiment, which utilizes liquid argon, it is possible for muons to induce proton spallation near the Ge detectors. For this reason, a selection of cosmogenic isotopes resulting from

the proton spallation of argon have been chosen for this analysis. Their half-lives, decay schemes, and end-point energies are shown in Table B.1. By searching for these specific isotopes in the data, it is possible to determine limits on their production.

The γ lines originating from these isotopes were investigated using data from GERDA Phase II and Phase II+ (Runs: 53-114) with all the enriched detectors i.e. (^{enr}BEGe, ^{enr}IC and ^{enr}Coax). All the quality cuts were applied to the data. Two different approaches were used to search for these γ lines in the data. The first approach, presented in 5.4.1 is focused on identifying potential characteristic γ lines directly in the germanium data. The second approach is described in section 5.4.2 which involves examining the decay structures of these isotopes by comparing the time difference between Ge and muon events.

5.4.1 First Approach: Search of γ-lines only in Ge-data

In the first approach, the analysis focused solely on the germanium data to identify these γ lines that arise from beta or γ decay. During this analysis, various constraints were applied to identify suitable γ lines in the data. The first constraint was that the γ line should have a significant intensity, making it detectable in the data. Another important constraint was to make sure that the selected γ line did not overlap with another line from a different isotope.

For instance, the isotope ^{38}Cl, in its metastable state has a short half-life of 715 ms. During its decay, it undergoes an isomeric transition by emitting a γ line with an energy of 671 keV. This γ line has a high intensity of 99.9%. The data was analyzed within an energy window of $\pm$ 50 keV around 671 keV energy, to search for this γ line as shown in Figure 5.7a. All the events with M=1 and After LAr veto cut were selected. A Gaussian distribution representing a peak (signal) along with a locally linear background (first-order polynomial) was fitted to the respective energy range using an (Unbinned Extended) Maximum Likelihood fit. The purpose was to identify any significant peak corresponding to the γ line at 671 keV. However, from the analysis shown in Figure 5.7a, it can be observed that no clear peak at 671 keV is observed in the data. The likelihood fit provides an estimation of the number of signal counts, allowing for the calculation of an upper

limit for the production yield within a 95% Confidence Level (CL). Similar analyses were conducted for the other isotopes listed in Table B.1. Their respective γ lines were examined for any significant peaks in the data within the designated energy windows. The energy region around the expected γ-lines of the three isotopes ^{38m}Cl, ^{39}Cl and ^{29}Al are presented in Figure 5.7a, 5.7c and 5.7e and the rest of them are placed in the Appendix B. None of these cosmogenic peaks clearly appear in the data and all the peaks of these isotopes are compatible with zero.

In order to estimate an upper limit on the number of signal events, profile likelihood method is used. As mentioned above, each data set x_i is fitted with Unbinned Maximum Likelihood by assuming the Gaussian distribution for the peak (signal) and a linear distribution for a background with a_0 and a_1 representing the intercept and slope of the linear function:

$$\mathcal{L}_i(x_i|N_{sig},\theta_i) = \frac{1}{N_{sig}+N_{bkg}} \prod_{j=1}^{N_i^{obs}} \left[N_{sig} \cdot \frac{1}{\sqrt{2\pi}\sigma_i} \cdot exp\left(\frac{(E_j-\mu-\delta_i)^2}{2\sigma_i^2} \right) + N_{bkg} \cdot (a_0 + a_1 E_j) \right] \tag{5.8}$$

where E_j represents the individual event energies and N_i^{obs} shows the total number of events observed in the i-th data set. The Gaussian was centered at $\mu\pm$ 0.2 keV [41] taking into account the systematic uncertainty (δ_i) associated with the energy calibration. The width of the Gaussian, σ_i, was calculated using the formula $\sigma_i = \sqrt{a+bE}$, where a and b are fit parameters specific to different types of detectors (BEGe, Coax, and IC), as provided in [41]. The energy (E) used in this calculation was the energy of the respective γ line. For example, in the analysis of ^{38}Cl, the energy of the γ line under investigation is 671 keV. By inserting this value into the formula, the resolution at μ for ^{38}Cl was obtained. N_{sig} and N_{bkg} represent the expected number of signal and background events in the signal range. For the analysis of ^{38}Cl, the signal range was defined as 670-672 keV, where it was expected to observe the γ line. The parameters with uncertainties are indicated with $\theta_i = \{\sigma_i, \delta_i, N_{bkg}, a_0, a_1\}$. The total likelihood is constructed by taking the

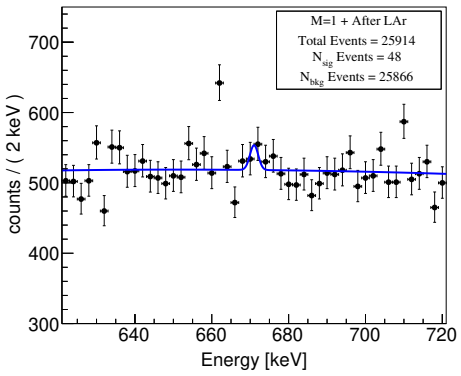

(a) 671 keV $\pm$ 50 keV IT in ^{38}Cl

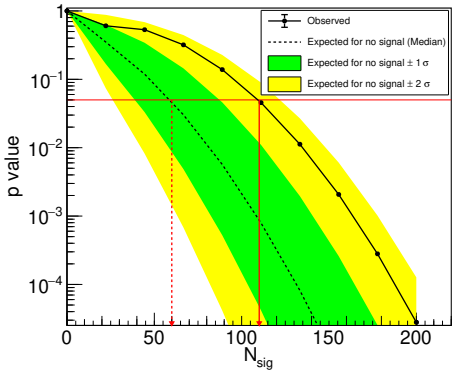

(b) $N_{sig} < 110$ counts (95% CL)

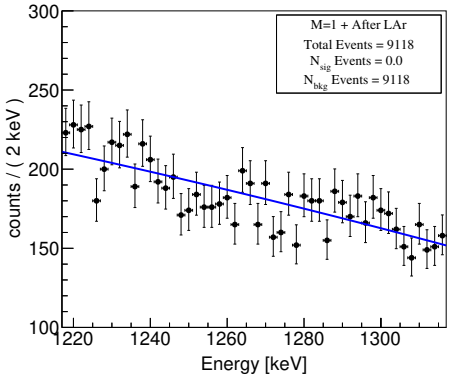

(c) 1267 keV $\pm$ 50 keV γ in ^{39}Cl

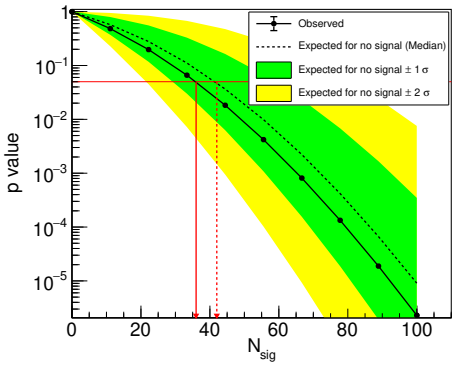

(d) $N_{sig} < 37.0$ counts (95% CL)

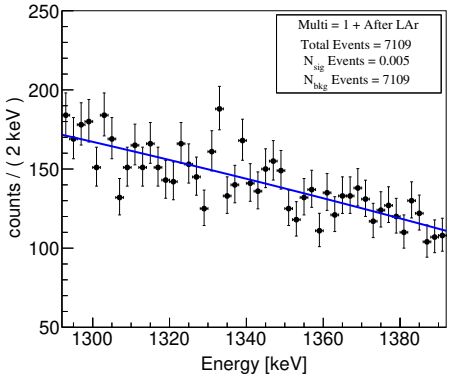

(e) 1342 keV $\pm$ 50 keV γ in ^{28}Mg

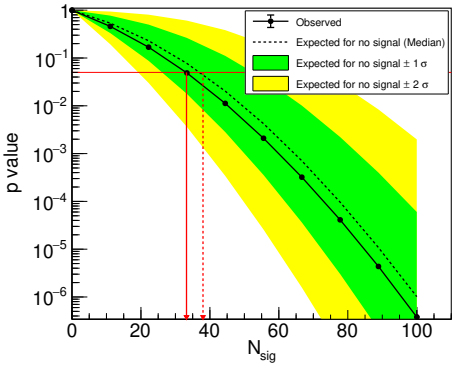

(f) $N_{sig} < 33.3$ counts (95% CL)

Figure 5.7: Potential γ-lines from ^{38m}Cl, ^{39}Cl, and ^{28}Mg isotopes. The figures (a), (c), and (e) represent energy windows for each isotope, while figures (b), (d), and (f) show the corresponding p-value distributions. The profile likelihood fit to the data consists of a Gaussian signal and a polynomial background. The upper limit on the number of signal counts, N_{sig}, within 95% CL is provided with each plot.

product of all individual likelihood terms ($\mathcal{L}_i$), weighted with the Poisson terms:

$$\mathcal{L}(x|N_{sig},\theta) = \prod_i \left[\frac{e^{-(N_{sig}+N_{bkg})} \cdot (N_{sig}+N_{bkg})^{N_i}}{N_i^{obs}!} \cdot \mathcal{L}_i(x_i|N_{sig},\theta_i) \right] \tag{5.9}$$

where x = {x_1,...,x_i,...}, N_{sig} = {$N_{sig,1}$,...$N_{sig,i}$...} and θ = {θ_1,...θ_i...}. Since the parameter of interest (POI) is the number of signal events N_{sig} and all the other parameters θ are treated as (unknown) nuisance parameters, the profile likelihood ratio λ (N_{sig}) is defined as:

$$\lambda(N_{sig}) = \frac{\mathcal{L}(N_{sig}, \hat{\hat{\theta}})}{\mathcal{L}(\hat{N_{sig}}, \hat{\theta})} \tag{5.10}$$

where $\hat{\hat{\theta}}$ in the numerator denotes the value of the parameter that maximizes $\mathcal{L}$ for a fixed POI (N_{sig}). In the denominator, $\hat{N_{sig}}$ and $\hat{\theta}$ represent the values of parameters that jointly maximize the likelihood function with respect to all parameters. The statistical analysis described here is performed with RooPlot/ RooStat [84] which are software frameworks commonly used for statistical modeling and analysis in high-energy physics and other related fields.

In the asymptotic approach, the probability is interpreted based on large sample approximations. The analysis performed here follows the method described by Cowen et al. [85] in which an asymptotic test statistic is constructed using a profile likelihood ratio. This ratio represents the maximum value of the profile likelihood function under the null hypothesis (in this case, assuming signal+background) to the maximum value under the alternative hypothesis (background only). The test statistic, denoted as $t_{N_{sig}}$ is defined as:

$$t_{N_{sig}} = -2 \ \log\lambda(N_{sig}) \tag{5.11}$$

To summarize the outcome, one quantifies the level of agreement between the observed data and a specific given hypothesis by computing a p-value. The p-value represents the probability, under the assumption of the given hypothesis, of finding data that is equally or more inconsistent with the predictions of the hypothesis. It serves as a measure of the compatibility between the observed data and the hypothesis being tested. If the p-value is found to be below a specified threshold, denoted as "a" the hypothesis can be rejected. The commonly used threshold for rejection is a = 0.05, corresponding to a 95% confidence level. This means that if the p-value is less than or equal to 0.05, the hypothesis is considered unlikely to be compatible with the observed data at the 95% confidence level. The

p-value is defined as:

$$p = \int_{t^{obs}_{N_{sig}}}^{\infty} f(t_{N_{sig}}|N_{sig})\, dt_{N_{sig}} \tag{5.12}$$

where $t^{obs}_{N_{sig}}$ is the value of the test statistic $t_{N_{sig}}$ observed from the data. The $f(t_{N_{sig}}|N_{sig})$ denotes the probability density function (pdf) of $t_{N_{sig}}$ under the assumption of the signal strength N_{sig}. It is determined by using asymptotic formulas mentioned by Cowen et al. [85] to get the sampling distribution of test statistics.

The p-value distribution for the hypothesis test, as a function of the N_{sig} counts is shown in Figure 5.7b. The dashed black line corresponds to the expected p-value distribution, with green and yellow bands indicating the 68% and 90% ranges, respectively. This expected p-value distribution is obtained by evaluating the test statistics using the values from the background-only (alternate) model. This expected p-value distribution is obtained by using the values from the background-only (alternate) model. It indicates the sensitivity of the analysis and represents what would be expected in the absence of a signal in the data. On the other hand, the solid black line represents the p-value distribution for the observed data. The red solid arrow indicates the upper limit at the 95% CL on the observed data whereas the red dashed arrow shows the upper limit on the median sensitivity. In the case of ^{38}Cl, the best fit yields a signal strength estimate of N_{sig} = 48 counts, and the upper limit on N_{sig} is determined to be $N_{sig} < 110$ counts (Median Sensitivity $N_{sig} < 65$ counts) within 95% CL.

The production yield (Y) of the isotopes can be determined by taking into account the detector efficiency and exposure. In this analysis, the production yield of the isotopes is calculated using the formula Y_i = (Number of Counts) / ($\varepsilon \times I \times \epsilon$), where ϵ represents the detector efficiency, ε is the exposure, and I denote the intensity of the γ emission. The total exposure of 102.3 kg. yr over the whole GERDA Phase II data was considered. The efficiency of detecting a 671 keV γ emission from a 30 cm sphere around the Ge array through MC simulations using MaGe, was found to be 0.199. This efficiency accounts for all energy depositions, including both the full-energy peak and the Compton spectrum. With an intensity of 99.9%, the calculated yield of ^{38}Cl in the Ge detectors is found to be Y (^{38}Cl) < 5.4 counts / (kg·yr). For all the other peak energies examined

in the analysis, no significant signals for these isotopes are observed in the data. The limits on the signal strength for each peak and their corresponding limits on the production yield of these isotopes over the entire GERDA Phase II data are presented in Table 5.2.

Isotope	γ-Energy [keV]	Observed Upper Limit [counts] @ 95% CL	Experimental Sensitivity [counts] @ 95% CL	Production Yield (Y_i) [nuclei/kg·yr]
^{38}Cl	671	110	64.5	5.4
^{39}Cl	1267	37.0	42.2	1.7
^{24}Na	1368	56.4	35.6	1.4
^{28}Mg	1342	33.3	38.3	1.5
^{29}Al	1273	24.8	41.8	0.6
^{27}Mg	1015	44.1	55.4	3.6
^{22}Na	1274	28.7	41.8	0.9

Table 5.2: Analysis Results of Isotopes: Observed and Experimental Limits and their Production Yields.

5.4.2 Second Approach: Search for decay structures in Ge-muon coincidence data

In addition to the search for γ-lines directly in the Ge-data, an alternate approach was used to search for decay structures of the isotopes in the data. This approach involved analyzing the time difference between Ge and muon events to identify potential radioactive decay. When a muon produces a radioactive isotope, it undergo decay according to its specific half-life, described by the equation $N(t) = N_0\, e^{-ln2 \cdot t/t_{1/2}}$. During the decay process, these isotopes have a chance to deposit energy in the Ge detectors. By comparing the timestamps of the Ge and muon events, it is possible to observe a characteristic exponential decay structure in the distribution of time difference between the events.

Certain constraints need to be taken into account when considering the half-

life of an isotope. If the half-life is too short, such as less than 3 μs, it can interfere with the prompt coincidences observed in the data. Conversely, if the half-life of an isotope is too long, any decay features it exhibits will be hidden, if the random coincidences are too high. Therefore, for the analysis, the half-life of the isotope should be long enough to allow the observation of characteristic decay features but not so long that the random coincidences dominate the data. Based on these constraints, the isomeric transition (IT) in ^{38}Cl with a half-life of 715 ms and an energy of 671 keV appears to be the best candidate for this type of analysis. A time-difference spectrum for the decay of ^{38}Cl is presented in Figure 5.8a. The analysis window is defined as four times the half-life of ^{38m}Cl and is constructed by setting the Ge events at t=0 and plotting all muon events within the specified window. For better visibility, the prompt coincidence region ($\pm 10 \mu$s) around t=0 is excluded from the spectrum. Additionally, an energy cut of 671 $\pm$ 5 keV, corresponding to the peak region of ^{38}Cl, is applied to this window. This energy cut guarantees that only events within the specific energy range associated with the decay of ^{38}Cl are considered. An exponential distribution for the signal and a polynomial distribution for the background with a fixed half-life of 715 ms is fitted to the data using unbinned maximum likelihood. The signal strength of the fit is again compatible with zero as shown in Figure 5.8a indicating that there is no exponential decay observed. To determine an upper limit on the number of signal counts, an asymptotic analysis using the profile likelihood as a test statistic is performed. The p-value distribution for this analysis is shown in Figure 5.8b. As a result, an upper limit of $N_{sig} < 58.7$ counts (with a sensitivity limit of $N_{sig} < 64.3$) for the decay of ^{38}Cl is obtained for the entire phase II dataset within a 95% CL. Additionally, the analysis yields a limit on the total counts/exposure, which is determined to be 0.5 counts/kg.yr over the entire Phase II data for ^{38}Cl isotope.

Another broader way to search for this decay is by constructing a two dimensional histogram of the time difference between Ge-muon events versus the energy window associated with the decay of ^{38}Cl. The 2D histogram in Figure 5.8c covers a time window of up to 10 seconds. Visual inspection of this plot reveals that there is no sign of a prominent γ-line at 671 keV associated with the decay of ^{38}Cl, around the expected half-life of 715 ms. None of the expected peaks asso-

ciated with the proton spallation of argon isotopes mentioned in Table B.1 have been observed in the GERDA Phase II data. Furthermore, the obtained limits on the decays are found to be quite low which indicates strong constraints on the possible occurrence of these decay processes in the data.

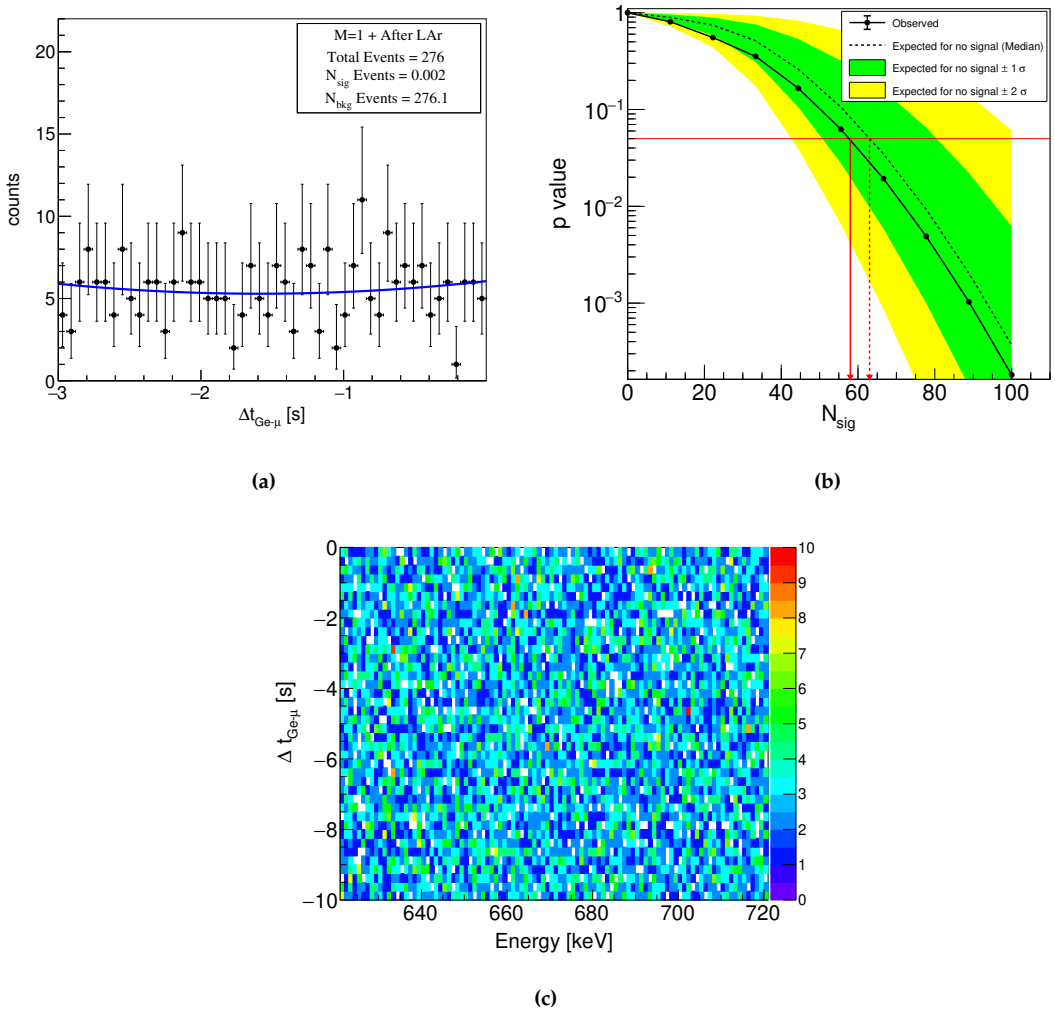

(a) **(b)**

(c)

Figure 5.8: (a) Time difference window for the decay of ^{38m}Cl with an energy cut of 671 $\pm$ 5 keV and (b) its corresponding p-value distribution. A profile likelihood fit of the model consists of a flat background with an exponential distribution for the deacy. A 95% CL upper limit on the number of signal counts ($N_{sig} < 58.7$) is obtained. (c) Two- dimensional histogram of time-difference ($\Delta t_{Ge-\mu}$) vs. energy window associated with the decay of ^{38}Cl.

Chapter 6

^{137}Cs Background Peak Analysis in GERDA Phase II data

While exploring the energy range of 621 keV to 721 keV in search of the ^{38}Cl cosmogenic peak signal (as displayed in Figure 5.7a), an unexpected and prominent peak of Cesium-137 ($^{137}_{55}$Cs) at 661.6 keV was discovered. Previous background studies, as referenced in [86, 87, 88, 89], broadly explained the expected background contributions arising from impurities in the materials used in the GERDA experimental setup. Since the Q-value of ^{137}Cs decay is substantially lower than that of the ^{76}Ge, the contamination with ^{137}Cs does not contribute to the background in the region of interest. Thus, this isotope did not attract much attention in previous analyses. However, the background contribution from ^{137}Cs is of great interest for upcoming LEGEND Experiments, since the aim of the LEGEND-1000 is to achieve a lower background index of $< 10^{-5}$ cts/(keV·kg·yr). The analysis presented in this chapter is conducted by the author of this thesis.

Cesium-137 ($T_{1/2}$ = 30.17 y) undergoes beta decay, transforming into Barium-137 (^{137}Ba) with a Q-value of 1175.6 keV. About 94.7% of these decays involve beta emission, leading to the formation of a metastable excited state of Barium-137m (^{137m}Ba). The remaining 5.3% of decays directly populate the stable ground state of ^{137}Ba. Within a relatively short half-life of 153 seconds, ^{137m}Ba decays to the ground state by the emission of 661.7 keV gamma [90]. This process generates a total of 85.1% of γ-ray emissions from the decay of ^{137}Cs. The detailed representation of the reaction involved in this decay scheme is described in Equation 6.1.

A visual representation of the decay scheme of ^{137}Cs is shown in Figure 6.1a.

$$^{137}\mathrm{Cs} \rightarrow {}^{137m}\mathrm{Ba} + {}^{0}_{-1}\beta \ \ (1175.6 \ \ keV) \qquad (6.1)$$
$$^{137m}\mathrm{Ba} \rightarrow {}^{137}\mathrm{Ba} + {}^{0}\gamma \ \ (661.7 \ \ keV)$$

To thoroughly investigate the presence of the 661.7 keV γ-line originating from ^{137}Cs throughout the entire GERDA Phase II data, all the enriched detectors such as ^{enr}BEGE, ^{enr}IC and ^{enr}Coax, were taken into account. The quality cuts were applied to the data. An energy window of $\pm$ 50 keV centered around 661.7 keV was examined with respect to different selection cuts. The result of the analysis representing this energy window under various selection cuts is shown in Figure 6.1b.

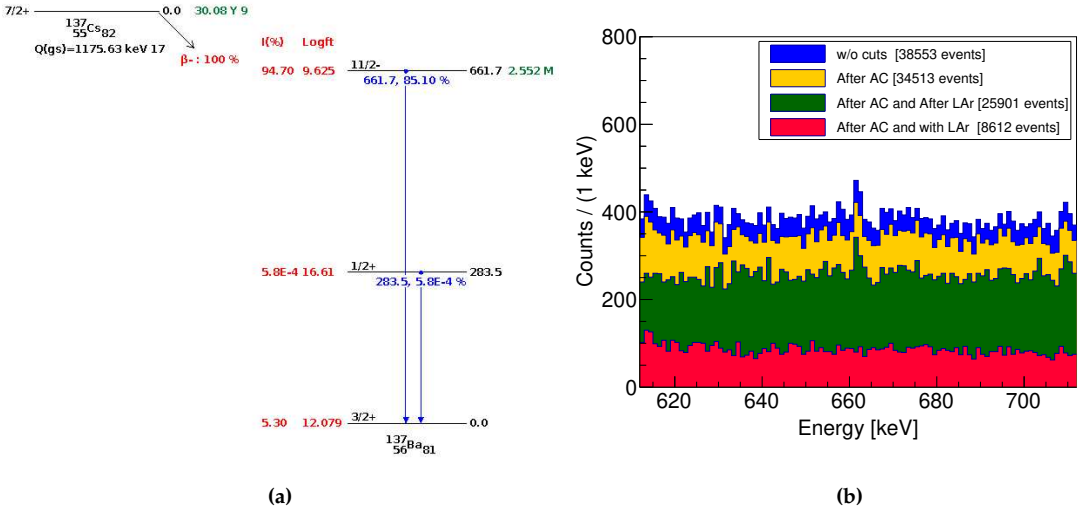

Figure 6.1: (a) Decay scheme of ^{137}Cs taken from [90], presenting the half-lives, daughter nuclides, and proportion of radiation emitted. (b) Energy window of γ = 661.6 keV $\pm$ 50 keV of ^{137}Cs isotope with respect to various selection cuts in the entire GERDA Phase II data.

A prominent peak at 661.7 keV energy is observed without any additional cuts, as indicated by the blue curve in Figure 6.1b. Even after applying additional cuts such as After AC (M=1) and After AC in combination with After LAr (w/o LAr), the peak remains visible, as shown by the yellow and green curves, respectively. However, when considering After AC (M=1) events in combination with the Ge events in coincidence with the LAr veto (with LAr), the peak disappears. This observation suggests that the contamination of ^{137}Cs isotope is more likely to be present in the nearby materials surrounding the detectors.

6.1 Statistical Analysis

In order to determine the number of signal counts (N_{sig}) in the peak region, an Extended Maximum Likelihood fit was performed on the energy window of 661.6 $\pm$ 50 keV, as shown in Figure 6.2a. This analysis utilized the same fitting procedure used for extracting signal counts during the cosmogenic peak search in Section 5.4.1. All the events with M=1 and After LAr veto cut were considered for statistical analysis. The likelihood model consists of Gaussian distribution centered at the γ-energy of 661.6 keV to represent the peak signal, along with a linear distribution for the background, as described in Equation 5.8. The systematic uncertainties, such as the energy resolution (σ_i) and possible systematic energy offset (δ_i) were taken into account. The Gaussian was centered at $\gamma_{662\ \mathrm{keV}} \pm$ 0.2 keV, i.e. (δ_i = 0 keV) is used as a central value for the peak shift and the uncertainty for the energy offset in the Gaussian term was set to 0.2 keV [41]. Furthermore, the width of the Gaussian peak (σ_i) is calculated using the formula $\sigma_i = \sqrt{a + bE}$, where 'a' and 'b' are specific fit parameters of FWHM resolution curves corresponding to different types of detectors, namely BEGe, Coax, and IC. Using the fit parameters from [41], and considering the energy E = 661.6 keV, the energy resolution for the ^{137}Cs peak was calculated to be 1.011. The uncertainty on the FWHM is calculated assuming the same relative uncertainty as for the FWHM at $Q_{\beta\beta}$ (taken from table 2 in [41]). N_{sig} and N_{bkg} as described in Equation represents the expected number of signal and background events in the signal range i.e. (661-663) keV for $\gamma_{662\ \mathrm{keV}}$ peak. After performing the Extended Maximum Likelihood fit on the energy window of 661.6 $\pm$ 50 keV and considering N_{sig} as a parameter of interest and all the other parameters with systematic uncertainties as nuisance parameters $\theta_i = \{\sigma_i, \delta_i, N_{bkg}, a_0, a_1\}$, the best-fit result yields a signal strength of N_{sig} = 156 counts, as shown in Figure 6.2a.

6.1.1 Profile Likelihood Analysis

To determine the two-sided limit interval on the number of signal counts (N_{sig}), the profile likelihood ratio test, as described in Equation 5.11, is used. The profile likelihood is constructed by fixing all the model parameters except one param-

eter (POI) and scanning over that specific parameter to calculate the likelihood at each point. This process effectively profiles out the nuisance (unknown) parameters and allows us to study the behavior of the likelihood as we vary N_{sig} while keeping the other parameters fixed at their best-fit values obtained from the full likelihood fit. The parameter of interest in this case is N_{sig} and nuisance parameters are denoted by θ_i. To represent the profile likelihood, the quantity $-2\log\lambda(\mathcal{L}) = -2\log(\mathcal{L}(N_{sig}, \hat{\hat{\theta}})/\mathcal{L}_{max}(\hat{N_{sig}}, \hat{\theta}))$ is plotted, where $\hat{\hat{\theta}}$ is the conditional maximum likelihood estimators for θ, i.e. the value for which $\mathcal{L}$ is maximized given a fixed value of a parameter of interest (N_{sig}) whereas $\hat{N_{sig}}$ and $\hat{\theta}$ are the maximum likelihood estimators that maximize $\mathcal{L}$ with respect to all parameters. According to Wilk's Theorem [91], the profile likelihood ratio follows a χ^2-distribution, i.e., $-2\log(\lambda) \sim \chi^2_N$ with 'N' degrees of freedom, where the number of degrees of freedom is the number of parameters of interest (in this case, one). By invoking Wilk's theorem, one can obtain upper and lower limits on parameters by finding the value of that parameter for which $-2\log(\lambda) = C$ where C is the critical value for a χ^2 distribution. For example, in the case of a 95% confidence level upper limit, $C = -1.92$.

The statistical analysis described here is performed with RooPlot/RooStat [84] framework. To calculate the profile likelihood ratio, the model pdf and the observed data are provided as inputs to the RooStats ProfileLikelihoodCalculator [92], which efficiently computes the likelihood profile. This calculator is a simple yet powerful tool for retrieving uncertainties at various confidence levels (1, 2, 3 sigma, etc). The ProfileLikelihoodCalculator is based on Wilks's theorem and the asymptotic properties of the profile likelihood ratio, which is known to follow a χ^2 distribution for the true value. By using this calculator, the profile likelihood is plotted against the N_{sig} as shown in Figure 6.2b which follows a parabolic behavior. The parabola indicates that the profile likelihood follows a χ^2 distribution, as expected from Wilk's Theorem. This χ^2 distribution allows us to set confidence intervals on N_{sig} based on the critical values. The minimum of the parabola corresponds to the maximum likelihood estimator for N_{sig}, and the width of the parabola around its minimum gives information about the uncertainty in the estimate of N_{sig}. The confidence interval of [82, 223] counts, represented by vertical

red lines is obtained within 95% confidence level on the estimated number of signal counts i.e. N_{sig} = 156 counts. The horizontal red line at C = − 1.92 in Figure 6.2b represents the critical value corresponding to the 95% confidence level.

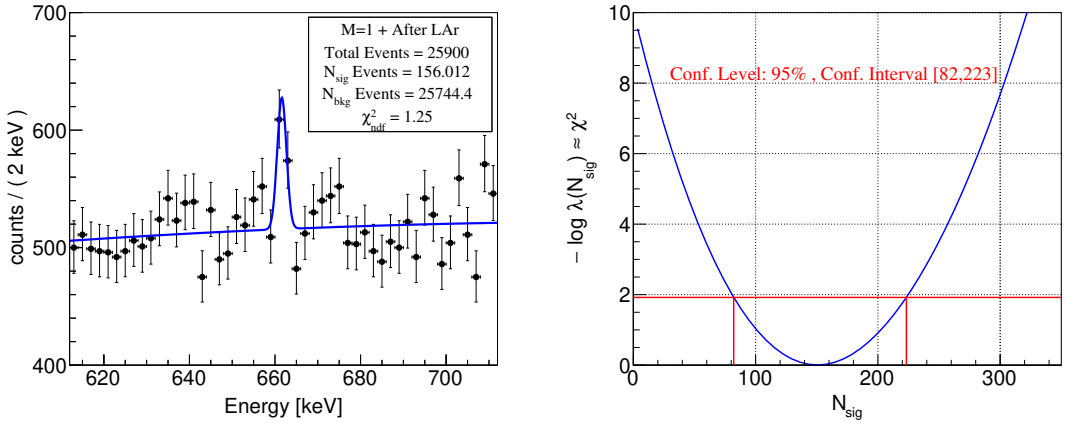

(a) Cs **(b)**

Figure 6.2: (a) Energy window of 661.6 keV ± 50 keV, with respect to M=1 and After LAr veto cuts. The profile likelihood fit to the data consists of a Gaussian signal and a Polynomial background. The best-fit yields a signal strength of N_{sig} = 156 counts in the entire Phase II data. (b) Profile likelihood scan of the parameter of interest (N_{sig}). Parabolic behavior indicates that profile likelihood follows a χ^2-distribution. The horizontal red line corresponds to −1.92 or 95% confidence level of a χ^2-distribution with one degree of freedom. Vertical red lines represent a confidence interval.

6.2 Determination of ^{137}Cs Specific Activity

The visibility of the ^{137}Cs peak in the enriched HPGe detector spectrum was necessary to estimate its specific activity. Monte Carlo (MC) simulations were performed to model the ^{137}Cs background originating from different components near the Ge-detector array. The specific activity, which represents the decay rate of ^{137}Cs nuclei per unit mass was calculated using the MC simulations and experimental data. Further details on the analysis of the MC simulations and specific activity calculation can be found in the corresponding sub-sections 6.2.1 and 6.2.2.

6.2.1 MC Simulations of ^{137}Cs Background in GERDA Phase II setup

In order to determine the activity from a number of signal counts, the source of ^{137}Cs from various components near Ge-detectors were simulated using the Geant4 based MAGE simulation framework. MaGe provides a full implementation of all the relevant components of the GERDA Phase II geometry, including the 40 Ge-detectors, their arrangement in 7 strings, the detector holder mounting, detector cables, front-end electronics as well as the LAr instrumentation. Figure 6.3 illustrates a graphical representation of the relevant hardware components implemented in MAGE. In this analysis, the decays of ^{137}Cs originating from the following components close to the Ge-detectors were simulated: the detector holder plates and holder bars seperately, detector HV and signal cables all together as well as parts of the cables (i.e. cable at holder and cables from holders to electronic board were simulated seperately) and the front-end electronics. The detector holders themselves consist of silicon (Si) holder plates and copper (Cu) bars as shown in the Figure 6.3b. Each germanium detector is mounted on a 1.5 mm thick silicon holder plate. The silicon plate plays a dual role: it defines the position of the vertical copper bars that support the Ge detectors and serves as a substrate onto which high voltage (HV) and signal cables are attached with bronze clamps. The copper bars are equipped with bolts and nuts at their top and bottom to enable connection to another detector module. The Ge detectors are read out with the custom-made preamplifiers called 'CC3' which are placed about 30 cm above the top of the detector array [38]. Figure 6.3c and 6.3d represents the front-end electronics in the simulation, visually indicated by vertical bars in the upper part. The readout electrode of Ge detector is connected to very front end Junction Field Effect Transistor (JFET) by a flexible flat cable (FFC), made from materials like Cuflon® or Pyralux®. Two different types of FFCs are used for the signal and HV contact: HV cables are made from 10 mils Cuflon®, or 3 mils Pyralux®, while the signal cables from 3 mils Cuflon® or Pyralux®. Each detector is equipped with one HV and one signal cable run along the side of the detector in a string, reaching from the detector's plate upto the front-end board

as implemented in Figure 6.3c.

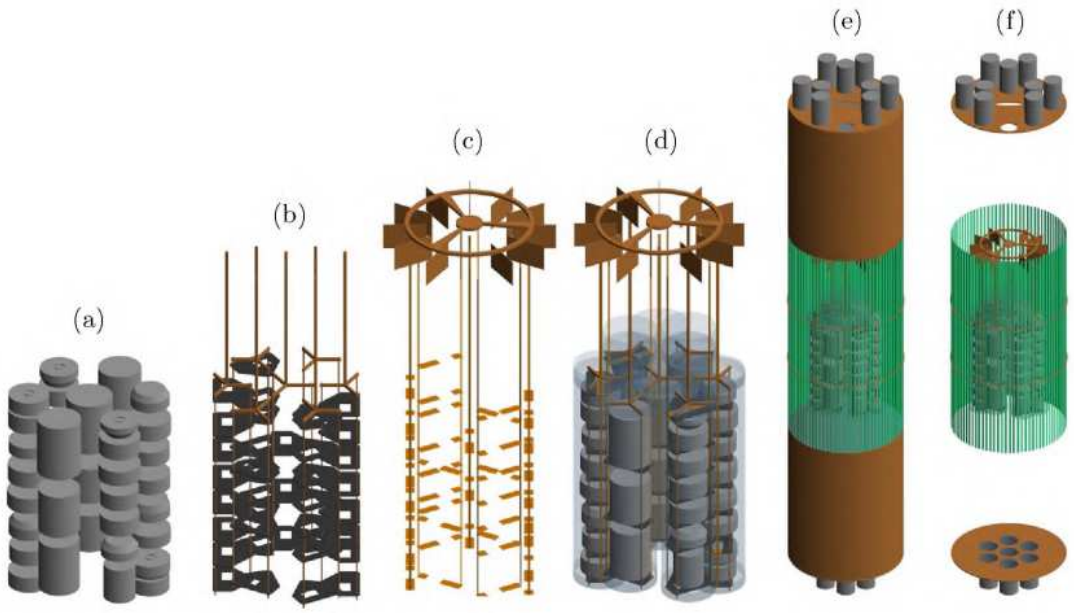

Figure 6.3: Visualization of the GERDA Phase II array in MaGe using Geant4 visualization drivers. (a) Gerda detectors arranged in 7 strings, (b) Holder mounting with Si plates and Cu bars, (c) Signal and High-voltage cables with front-end electronics on the top (30 cm from the detectors), (d) Full array instrumentation with transparent nylon mini-shrouds, (e) LAr veto system surrounding the array, including fiber shroud in green, Tetratex®-coated Cu shrouds above and below the fibers, and two PMT arrays (9 on the top and 7 on the bottom), (f) LAr veto system without Cu shrouds [86].

For each of these components, a total of $2 \cdot 10^8$ decays of the ^{137}Cs isotope were simulated. The events were generated by the G4gun of Geant4 to sample the decay from the final state of the isotope. All the simulated decays were uniformly distributed within the material of the respective hardware components. As an output, the sum energy depositions in the active volume of the detector crystals were constructed. Figures 6.4a, 6.4b and 6.4c show the resulting simulated energy spectra from the decays of ^{137}Cs in all cables combined, holder plates and holder bars. These spectra provide a detailed view of the contribution of each individual component to the overall background signal in the Ge-detectors. The remaining simulation spectra, which include the separate parts of the HV and signal cables, as well as the front-end electronics, can be found in Appendix C.

During the initial step of the analysis, it was observed that the prominent 661.6 keV peak, despite its significant branching ratio of 0.851, didn't appear in the

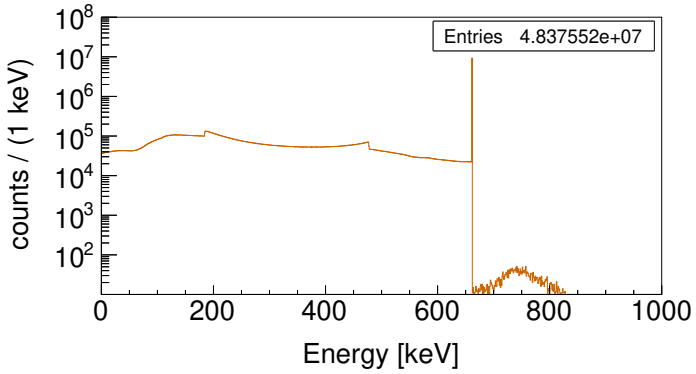

(a) ^{137}Cs MC simulation spectrum with the source origin in all cables.

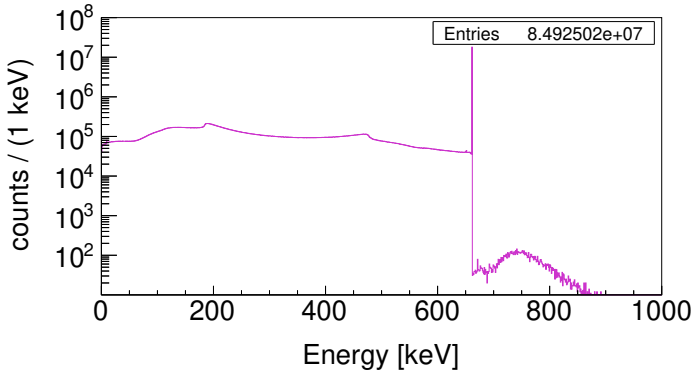

(b) ^{137}Cs MC simulation spectrum with the source origin in holder plates.

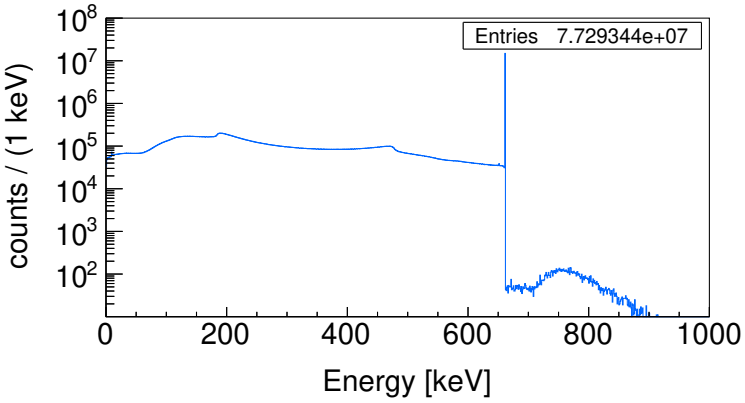

(c) ^{137}Cs MC simulation spectrum with the source origin in holder bars.

Figure 6.4: Simulated signature of ^{137}Cs decays in the enriched HPGe detectors with a source origin in (a) All Cables, (b) Holder Plates and (c) Holder Bars.

simulated spectrum. After investigation, the issue was traced within the MaGe, specifically within the Geant4 SteppingAction class. Originally there was a flag in this class which was set to kill daughter nuclei with a lifetime longer than 1μs without triggering their decay, to improve the simulation performance. However, the decay process of ^{137m}Ba to ^{137}Ba, which is responsible for 661.6 keV γ-line

takes approximately 153 seconds [90] to occur. Due to the 1μs threshold, this decay event was not being triggered, resulting in the missing peak. Hence, by increasing the threshold of the flag, the problem was thus resolved.

Before production, all the materials used in cables, electronics, and holder structures have been through screening to ensure that they satisfy the requirements of radio-purity. To study the background in more detail and to compare it with the expectations from screening measurements, the specific activity of all these components is calculated.

6.2.2 ^{137}Cs Specific Activity Calculation

By generating $2 \cdot 10^8$ events as a known quantity of ^{137}Cs source, the specific activity from different components near the detectors can be determined. The number of events observed under the 661.6 keV γ-line from the MC spectra was scaled down to its corresponding events from the measured data, allowing for the determination of the scaling factor, denoted as f_{scale}. The specific activity of the ^{137}Cs source ($A^{^{137}Cs}$) in the units of Bq/kg, was calculated using the following Equation 6.2.

$$A^{^{137}Cs} = \frac{N_{sim} \cdot f_{scale}}{T \cdot m} \tag{6.2}$$

where N_{sim} is the total number of simulated events used to obtain the energy spectrum, 'T' represents the total data-taking time of GERDA Phase II in seconds (T = 1.165 $\times$ 10^8 s), and 'm' represents the mass of each of the simulated components. For instance, by using the known mass of the cables, m_{cables} = 0.031 kg, and the ratio of the counting rates at 661.6 keV peak in the observed and simulated spectrum for all cables together (f_{scale} = 0.2 $\times 10^{-4}$), the estimation on the specific activity of ^{137}Cs in the cables ($A^{^{137}Cs}_{cables}$) can be calculated as:

$$A^{^{137}Cs}_{cables} = 1.00 \ \ mBq/kg \tag{6.3}$$

Similar calculations were performed for all the other simulated components, including the HV and signal cable parts individually, holder plates and holder bars, and front-end electronics, to obtain their respective specific activities. The results of these activity calculations, along with the masses, materials, and amount

of these components in the simulation, as well as the activity of these components from material screening, are summarized in Table 6.1. The masses of these components, as implemented in the MaGe, are taken from [93].

Source	Parts	Amount	Material	Mass [kg]	Calculated Activity* [mBq/kg]	Screening Activity [mBq/kg]
^{137}Cs	All Cables	160	-	0.031	1.0	< 0.13
	HV Cables HV Cable at Holder HV Cable from Holder to Electronics-Plate	40 40	10 mils Cuflon or 3 mils Pyralux	0.0018 0.0124	9.8 2.8	- -
	Signal Cables Signal Cable at Holder Signal Cable from Holder to Electronics-Plate	40 40	3 mils Cuflon or Pyralux	0.004 0.012	3.32 2.95	- -
	Holder Plates	40	Silicon	0.659	0.023	< 0.13
	Holder Bars	102	Copper	0.540	0.033	< 1.1
	Front-end Electronics	6	CC3 JFET BF862	0.052	157.2	< 7.96

Table 6.1: Summary of the GERDA components for which background contaminations of ^{137}Cs are simulated, including their amount, material, and masses as implemented in MaGe. The table also presents the *required activities to explain the ^{137}Cs peak in the data and activities from material screening, for each component.

The results were then compared with the activities of these components obtained from material screening [94, 38]. The calculated and required activities to explain the ^{137}Cs peak in the detector holder plates (0.023 mBq/kg) and bars (0.033 mBq/kg) were found to be lower than the upper limit of the material screening results i.e. holder plates: (< 0.13 mBq/kg) and bars: (< 1.1 mBq/kg) as shown in Table 6.1. This suggests that the detector holder plates and bars could be the source of the ^{137}Cs peak in the data. On the other hand, the calculated activity for all cables (1.00 mBq/kg) is higher than the upper limit of the material

screening result (< 0.13 mBq/kg) suggesting that the calculated activity exceeds the detection limit of the material screening for the cables. Also, the calculated activity for front-end electronics (157 mBq/kg) showed a significantly higher value compared to its value from screening (< 7.96 mBq/kg) and also compared to the other components, making it very unlikely to be the source of the ^{137}Cs peak. This analysis thus verified that the dominant background source location of ^{137}Cs in GERDA Phase II data could be the holder plates and bars. With a better understanding of the precise origin of background sources, the LEGEND-1000 experiment will be able to develop new techniques to mitigate these impurities, such as using even lower activity holder plates and bars, before assembly of the experiment and thus reduce its background index even further to a predicted value of 0.025 counts /(FWHM$\cdot$ t $\cdot$ yr), effectively reaching a background-free regime [19].

Chapter 7

From GERDA to LEGEND-200 Experiment: MC Simulation of Muon Veto

The Large Enriched Germanium Experiment for Neutrinoless Double Beta Decay (LEGEND) collaboration was formed in October 2016, with the aim of constructing the next generation of $0\nu\beta\beta$ decay experiments using ^{76}Ge. The experimental program is divided into two stages: the first stage involves the operation of a 200 kg array of ^{76}Ge-enriched detectors, known as LEGEND-200, which is currently running and collecting data. The ultimate plan is to build a ton-scale ^{76}Ge $0\nu\beta\beta$ decay experiment called LEGEND-1000.

The LEGEND-200 experiment went through significant changes with the adoption of new technologies, advanced hardware electronics and, sophisticated software. Moreover, the muon veto system, an essential part of the experiment, also experienced significant modifications, including the removal of spectroscopy oil form all the PMTs and a reconfiguration of PMT placements within the water tank. To ensure that these changes wouldn't compromise the muon veto's effectiveness, a Monte Carlo (MC) study was conducted before the modifications to check the sensitivity of the veto under the altered conditions. This chapter explains why the repair was necessary and provides a detailed explanation of the simulations conducted by the author. The next chapter 8 will cover the LEGEND-200's integration and commissiong of muon veto data.

7.1 Final Water Drainge of GERDA Water tank

The LEGEND-200 experiment, was planned to be set up at LNGS (Laboratori Nazionali del Gran Sasso), the former host of GERDA and decided to use the existing infrastructure from the GERDA experiment. In February 2020, the GERDA infrastructure was officially handed over to the LEGEND collaboration. After the end of the GERDA data taking, the water tank containing the muon veto system was drained in September 2020, for inspection. During or after the water drainage, two PMTs (103 and 506) were imploded, one from the Pillbox and the other from the 4m on the wall, resulting in the spillage and mixing of the spectroscopy oil from these PMTs into the water. Although the oil was drained, there were concerns about potential health hazards due to this exposure. According to the manufacturer, the used spectroscopy oil in the PMTs is not considered hazardous or dangerous under EU regulations [77, 72]. However, to ensure safety, the decision was made by the University of Tuebingen to remove the oil from all PMTs for the muon veto of LEGEND-200 experiment.

7.1.1 Transmission of light to the photocathode with and without Mineral oil inside PMT Capsule

As mentioned in Section 4.1.1, the spectroscopy oil was added to the PMT capsules in the first place to facilitate a smooth transition of the refractive index from water medium to PET window and further to the PMT. Without the oil, the space between the PET cap and the PMT would be filled with air, which has a refractive index of approximately $n_{air} \sim 1$, significantly different from that of the PET cap ($n_{PET} \sim 1.61$) and water ($n_{water} \sim 1.34$). The refractive index of oil is $n_{oil} \sim 1.47$ which is closer to the refractive index of water. It was estimated that without the oil, approximately three times less light would reach the PMT, with the rest being reflected at the boundaries. The oil therefore improved the overall data quality by enhancing light collection efficiency. However, this raised the question of how the absence of the oil will affect the overall performance of the muon veto system. In order to observe this scenario, a MC simulation nested in experimental data was performed to estimate the efficiency of the veto after reducing light efficiency by

a factor of three.

The arrangement of PMTs within the GERDA muon veto system is displayed in Figure 4.1b, which were organized in the form of seven rings inside the water tank. According to the simulations referenced in [74], along with the years of GERDA muon data, it is verified that the PMTs located inside the Pillbox and on the floor of the tank play a vital role in detecting muons. In the referenced simulation study [74], the efficiency of muon veto was calculated for several scenarios. The whole veto exhibited an exceptional efficiency of $(99.935 \pm 0.015)\%$. To further check the veto's efficiency by removing the number of PMTs in the Pillbox, it was observed that the efficiency dropped accordingly. Although even in the case of four out of six PMTs in the pillbox being excluded, the efficiency remained notably high at $(97.855 \pm 0.065)\%$. From these calculations, it was concluded that even in the unlikely event of one or two entire FADCs being removed, the efficiency remained above 99%. However, the removal of very few pillbox PMTs resulted in a significant decrease in efficiency compared to the loss of several PMTs in the main water tank. These results can be found in Table 5.5 of [74]. It means that the loss of more than one PMT in the pillbox should be regarded as a reason for an exchange of the PMTs at the earliest possible opportunity.

As mentioned in Section 4.5, throughout the entire operational lifetime of GERDA, in total 10 out of 66 PMTs were lost. Of these, two were located inside the Pillbox and one resided on the floor. Hence, to replace these defective ones with fully functional ones and to increase the number of PMTs inside the pillbox and on the floor, a decision was made to relocate the upper ring of functional PMTs positioned at a height of ~ 6.5 meters on the tank's wall and brought them down to distribute them in the pillbox and on the floor of the water tank. Therefore, alongside the removal of the spectroscopy oil, the MC simulation presented in this chapter also checked the rearrangement of PMTs inside the water tank, to ensure the continued efficiency of the muon veto system.

7.1.2 MC Simulation to study the sensitivity of veto

After the removal of oil, PMT can only see one third of the total light so, in order to check the sensitivity of the muon veto without the oil in the PMTs, the simu-

lation was performed with artificially reduced the amount of light entering the PMTs by a factor of three. Afterward, the impact of it on the analysis of muon-Ge coincident background events using the GERDA Phase II and Phase II+ data as described in Section 5.3, was studied. The objective was to model the variation in the quantity of light that reaches the PMT and evaluate its implications on data analysis.

Simulation Methodology: The simulation begins with the creation of probability distribution for an event to happen. To introduce the variability in light detection, a Gaussian random number generator was implemented with a mean centered at 0 and a standard deviation of 1, effectively mirroring the fluctuations in light detection. To distinguish between accepted and rejected events within the simulation, a threshold of - 0.43 was introduced which corresponds to 1/3 of the distribution (i.e. lower tail of the Gaussian distribution).

Hence for each event in the data, the random number generator was applied to each individual PMT that fired or triggered. If the generated number falls below the threshold of -0.43, the event was selected for further analysis. Conversely, if the generated number was greater than the threshold, the event was artificially rejected for analysis. Hence with this approach of toy MC, only 1/3 of the light was selected to be seen by the PMT. In addition to that, the upper ring on the wall containing 10 PMTs was also removed from the analysis, to see its impact on the data.

Simulation Outcome and Muonic Background Analysis: The outcome of the simulation on the GERDA's entire Phase II and Phase II+ data is represented in Figure 7.1b. This figure clearly illustrates that with only 1/3 of the light seen by the PMTs, we encountered a minimum loss of only 5 muon-Ge coincident events out of the total 4870 events. Figure 7.1a is added for comparison which showcases the original muon-Ge coincident background with respect to different selection cuts, as detailed in Section 5.3, while Figure 7.1b presents the results of MC simulation plus the removal of upper ring of PMTs from the wall. It can be seen from the figure, that these five events were the ones detected by the LAr veto system. This loss corresponds to only 0.1% of the total events, highlighting the reliability and effectiveness of the muon veto system. However,

it is noteworthy that despite the reduction in light efficiency, there was no impact on the remaining muonic background events after all the cuts (i.e. M=1 and no LAr).

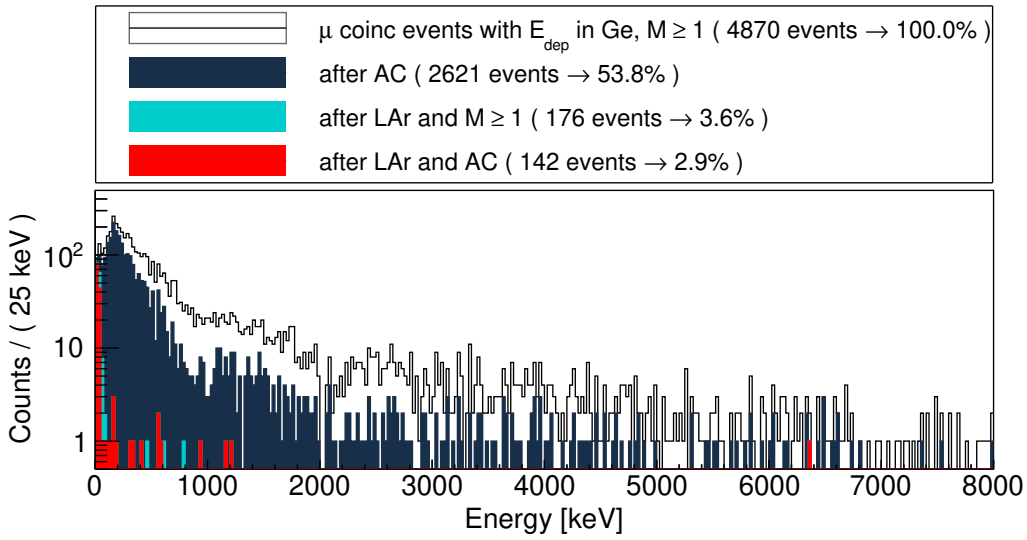

(a)

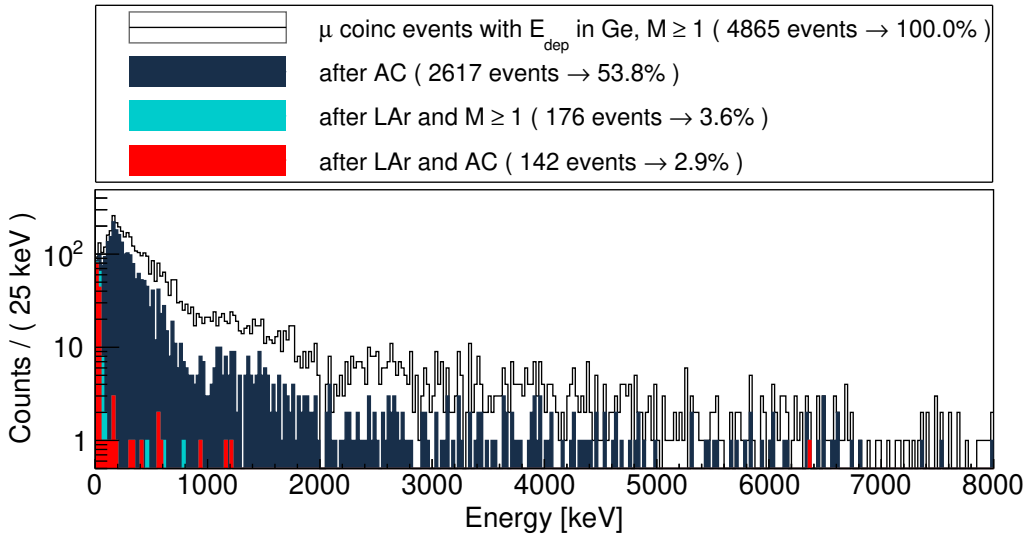

(b)

Figure 7.1: (a) Original analysis of the energy distribution of muon-induced background over the entire energy range under the assumption of various cuts i.e. M $\geq$ 1, After AC (M=1), After LAr veto plus M $\geq$ 1 and After LAr veto plus AC cut, added for comparison. (b) represents the energy distribution of muon coincident Ge events within a time window of 10 μs under the assumption of similar cuts after applying a toy MC simulation and excluding the upper ring of PMTs located at $\sim$ 6.5 meters on the wall of the tank.

All five of the missing events had lower energies i.e. well below 1 MeV. The energy distribution of these five events is shown in Figure 7.2. Four of these events

with E = 152 keV, 160 keV, 391 keV, and 598 keV were Ge-multiplicity one events while one event with E = 466 keV exhibited a Ge multiplicity greater than one but all these five events were seen by the LAr veto. As all the missing events were at lower energies, i.e. far below the region of interest, hence their absence had no impact on the background index from muonic-induced background within the ROI.

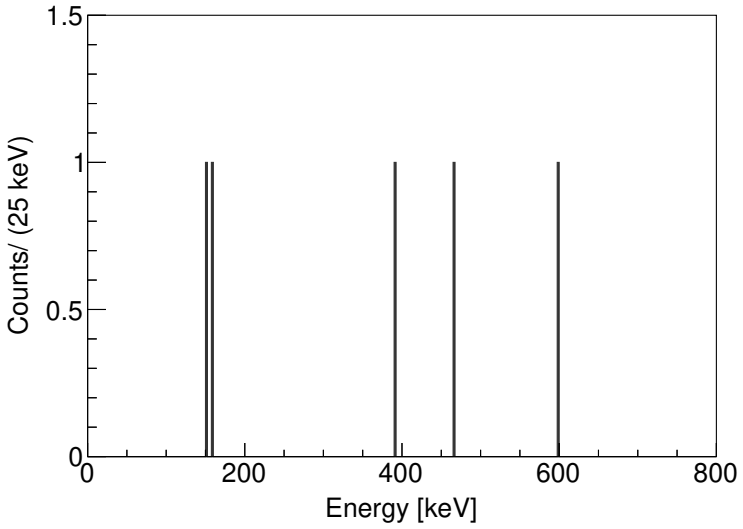

Figure 7.2: Energy distribution of the five missing events.

The PMT multiplicity of a total 4870 events when using all 66 PMTs as in the original setup and the impact of MC on the PMT multiplicity when considering only 56 PMTs (by removing upper ring of PMTs) are shown in Figure 7.3a and 7.3b respectively. In Figure 7.3b, a noticeable shift in the event multiplicity distribution towards the lower part of the spectrum is observed. This shift occurred as a result of reducing the availability of light by a factor of three during the MC simulation as well as by reducing the number of PMTs in the analysis. All these 4865 events were seen by the less number of PMTs then before as visullay presented in Figure 7.3b. The summary of muon-Ge coincident events for different scenarios with respect to various selection cuts is presented in Table 7.1. It can be seen from the table that exclusion of upper ring of PMTs from the original analysis has no impact on the total number of events. However, this modification does cause a shift in the PMT multiplicity distribution towards the lower values in the spectrum. Conversely, when a toy MC simulation is applied to the data, a reduction

in the number of events is observed in comparison to the original analysis.

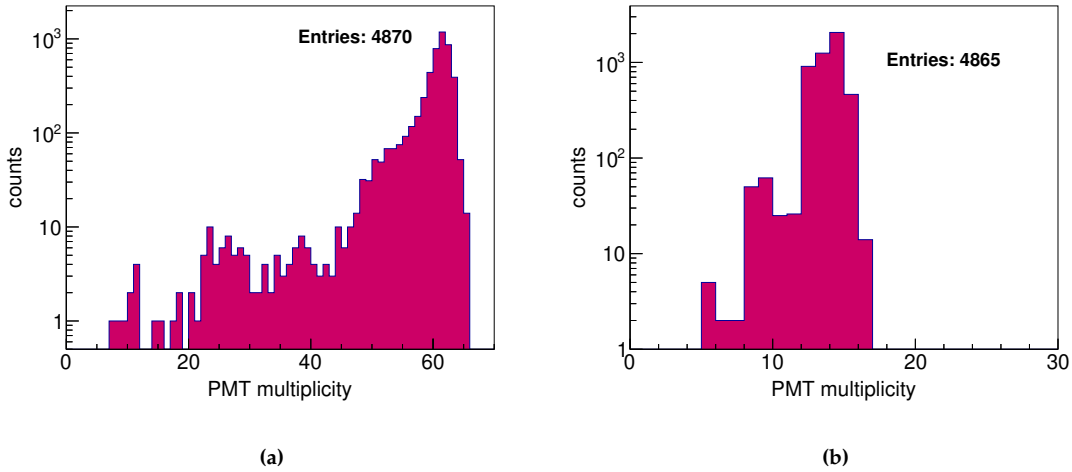

(a) (b)

Figure 7.3: Comparison of PMT Multiplicity: (a) Original Analysis with 66 PMTs. (b) MC Simulation with 56 PMTs in the data. The upper ring of PMTs were not considered.

Analysis	All Events	After AC	After AC + M≥1	After LAr + AC
Original Analysis	4870	2621	176	142
Original Analysis w/o upper ring	4870	2621	176	142
MC + no ring removed	4865	2617	176	142
MC + w/o upper ring	4865	2617	176	142

Table 7.1: Summary of the muon-Ge coincident events for different analyses considering various selection criteria in the same sequence as mentioned in Figure 7.1a i.e. For all events (M $\geq$1), After AC (M=1) events, After AC + M $\geq$1 and After LAr + AC events.

This simulation allows for the comprehensive estimation of how much light at a maximum level, can be afforded to be lost without compromising the efficiency of the muon veto. By using this approach, the conclusion can be drawn that even under the most adverse conditions, where 2/3 of the light will not be detected, the veto's sensitivity remains sufficient and as all the missing five events lies below 1MeV energy, it can confidently concluded that sensitivity of the veto remains the same at least above 1 MeV energy.

Chapter 8

Muon Veto System of LEGEND-200: Integration and Commissioning

LEGEND-200 re-uses much of the existing infrastructure of the GERDA Experiment at LNGS, including the muon veto system of GERDA, which was originally designed and built by the University of Tuebingen. This chapter begins with a comprehensive description of the refurbishment process of the muon veto system for LEGEND-200, as detailed in Section 8.1. The process involved the removal of oil from all the PMTs and their re-arrangement inside the water tank. The execution of this task was led by the University of Tuebingen's dedicated team, with the author actively contributing to the effort. Sections 8.2 and 8.3 discuss the new DAQ system for the muon veto and the associated hardware trigger settings to record meaningful data, which is a joint work of research collaboration. In Section 8.4, a review of the new data format and a new software framework based on Python programming, built specifically for LEGEND-200 are described. However, Sections 8.5 and 8.6 provide a detailed description of the calibration and monitoring of PMTs after the refurbishment of veto, along with the first look at the muon physics data, conducted by the author of this thesis.

8.1 Refurbishment of the veto

The simulation study described in Chapter 7 clearly indicates that even after the removal of oil from the PMTs, the muon veto system will maintain a satisfactory

level of performance. Therefore, a team from the University of Tuebingen went to LNGS in July 2021, to modify the GERDA's muon veto system for the LEGEND-200 experiment. The refurbished procedure involved two main steps: firstly, the removal of spectroscopy oil from the PMT capsules, and secondly, the reconfiguration of PMT placements within the water tank. As mentioned in section 7.1.1, the PMTs located in the pillbox and floor of the water tank are of great importance for muon detection. Notably, two out of six PMTs within the pillbox and one PMT on the floor of the water tank were malfunctioning (or broken) during GERDA's lifetime as graphically indicated in Figure 4.1b. To replace these faulty PMTs and to increase the number of PMTs in these two specific regions, a total of nine functional PMTs from the upper ring, positioned at a height of 6.5 meters on the tank wall were removed and taken down to place them in the pillbox and floor of the tank. Among them, six PMTs were distributed inside the Pillbox, while the other three were positioned on the floor, thereby effectively enhancing the detection capabilities in these critical regions. A visual representation of the new PMT arrangement within the water tank is shown in Figure 8.6. The PMTs brought down from the upper ring are highlighted in green circles, clearly marking their placement in the setup. The careful process of removing oil from the PMTs is explained through the following step-by-step procedure:

Step 1: The first step involved draining the oil from PMTs, and this was done by loosening the screws that secure the metal ring holding the PET cap. These screws were directly threaded into the steel capsule of the PMT. To collect the oil, a container (bucket) was positioned beneath the PMT. The collected oil in the bucket was later emptied into designated waste disposal containers located outside the water tank. During this step, the screws

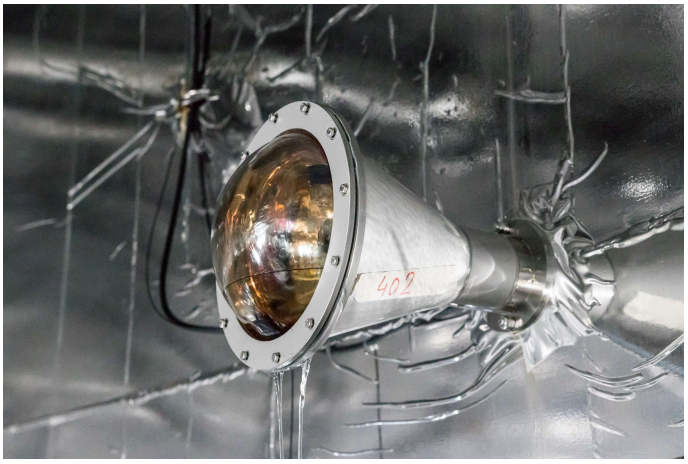

Figure 8.1: Loosening the screws and draining the oil.

were only partially loosened,
without being fully removed. This approach aimed to retain the PET window attached to the PMT for as long as possible, with the intention of keeping it in a clean state.

Step 2: In the next step, both the screws and the metal ring were carefully removed. Afterwards, the silicon seal binding the PET cap to the capsule was broken by gently lifting the PET cap and thereafter, the PET window was also detached, leaving behind the empty PMT, as visually presented in the attached Figure 8.2. To ensure cleanliness and avoid any contamination, all individuals participating in the process wore specialized cleanroom suits, overshoes, masks, face shields, gloves, and helmets.

Figure 8.2: Screws, metal ring, and PET cap were removed.

Step 3: Afterwards, the empty PMT was covered with a new rigid acrylic cap over it, replacing the previous flexible PET covers. To make sure it fits tightly, a rubber seal was inserted between the steel capsule and the acrylic cover. Throughout this process, a protective green plastic foil displayed in Figure 8.3 was kept on top of the cap to protect it against any scratches.

Figure 8.3: PMT covered with rigid acrylic cover.

Step 4: To make the seal even tighter, the connection between the capsule and the cap was supported with butyl tape. This tape also extended to cover the screw holes located both at the top and bottom of the flange, as shown in the figure attached. To further secure this butyl tape, quarter ring flanges were placed on both the top and bottom sides of the butyl tape, ensuring a firm placement as described in the next step.

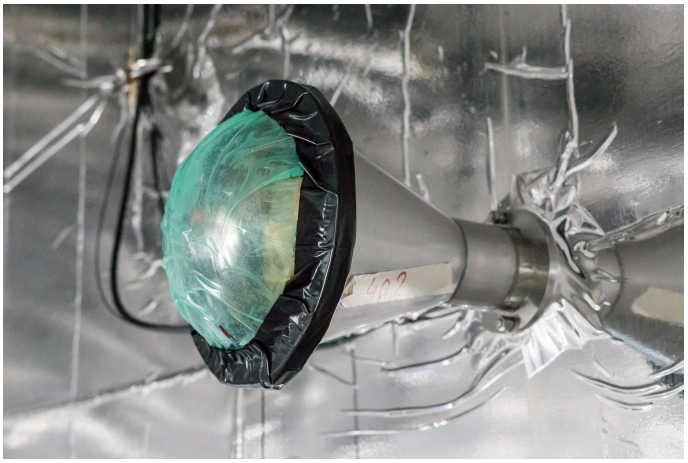

Figure 8.4: Cap is fastened with the capsule via butyl tape.

Step 5: Following the placement of the quarter metal rings on the top of the butyl tape, the screws were driven through the butyl tape, inserting it into the thread to provide additional sealing there as well. The screws used for this purpose were designed to withstand a torque of ∼10 Nm, ensuring a secure and reliable seal. To further enhance the sealing and structural integrity of the assembly, quarter rings were also applied from the bottom of the flange. These rings were carefully placed on and secured in place using nuts, which were also torqued to ∼ 10 Nm. This dual-layered approach ensured a tight and leak-proof seal for the PMT assembly. Upon completion of this fitting procedure, the foil attached to the acrylic cap was removed.

Figure 8.5: PMT fixed with quarter metal rings on top and bottom.

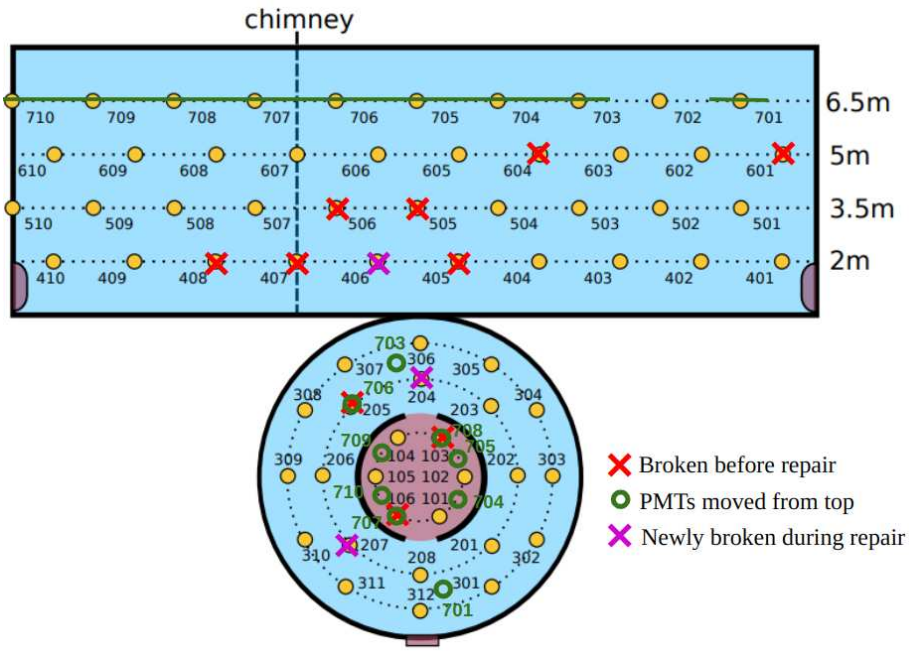

Figure 8.6: New arrangement of PMTs implemented for LEGEND-200 after the refurbishment of muon veto system. Notably, nine PMTs from the upper PMT ring were removed and relocated to the pillbox and on the floor of the tank, as indicated by the green circles. PMTs marked with red crosses are the broken ones from GERDA and those marked with purple crosses represent the newly broken PMTs during the refurbishment process. One PMT, due to an accessibility issue, remained in the upper ring.

8.2 New Data Acquisition System of LEGEND-200

The previous GERDA muon veto DAQ system 'Struck SIS 3301 modules' has been replaced by the more advanced and efficient FlashCam system for the LEGEND-200 muon veto. FlashCam (FC) is one of the most advanced camera systems which was originally developed for the Cherenkov Telescope Array (CTA) experiment [95] and is used up to now by many other experiments such as HESS [96] and HAWC [97]. The FlashCam system is based on an FPGA-based (Field Programmable Gate Arrays) readout board and a data acquisition software framework optimized for high-speed data processing and real-time event selection.

The Muon veto DAQ system of LEGEND-200 consists of one master card which is further divided into three FlashCam ADC cards. Each ADC card consists of 24 channels so in total, there are 72 channels reserved for the muon veto system. Each PMT has its own dedicated ADC channel. Any ADC card can set a

multiplicity of 24 channels and any ADC card can send a local trigger to the master card. The master can set a multiplicity of 3 ADC cards. In terms of sensitivity, the trigger threshold for each PMT is kept at a pulse height of 15 ADC-channels which is equivalent to 0.5 photoelectrons (p.e). The analog signals of the PMTs are digitized continuously with a sampling rate of 250 MHz at 12-bit resolution which is 2.5 times higher than that employed by the GERDA DAQ system. The distribution of all 54 PMTs across the ADC channels is summarized in Table 8.1.

The first FlashCam card, designated as "Card-0" in Table 8.1, accommodates all 10 PMTs located in the Pillbox region. These PMTs are connected to the FC channel numbers 4 to 13. The channel-0 of Card-0 is reserved for the pulser, used for the calibration of PMTs. The rest of the channels on this card are empty. The second FlashCam card, referred to as "Card-1" contains all 20 PMTs from the floor of the water tank, connected across FC channel numbers 0 to 19. The rest of the 4 channels on this card remain unoccupied. Similarly, the third ADC card "Card-2" consists of 23 PMTs from the Wall of the water tank, connected to the FC channels spanning from 0 to 22. Only one channel on this card is left vacant. The broken PMTs from GERDA are not connected to the new FlashCam cards.

8.3 New Trigger Conditions for muon veto of LEGEND-200

With the introduction of a new DAQ system and a revised arrangement of PMTs for the veto, the need to establish new trigger conditions to record data became necessary. In order to estimate new trigger conditions, a methodology similar to that employed in the GERDA experiment was used i.e. taking random coincidences into account which are caused by the dark rate of the photomultiplier. In order to calculate the rate of random coincidences (D_{rand}) for the possible trigger conditions, the following equation was used:

$$\begin{aligned} D_{rand} &= \binom{F}{N} D_{dark}^{N} \cdot \Delta t_{coinc}^{N-1} \\ &= \frac{F!}{N! \cdot (F-N)!} D_{dark}^{N} \cdot \Delta t_{coinc}^{N-1} \end{aligned} \tag{8.1}$$

where, "F" is the total number of detectors used, from which "N" detect a sig-

Muon Veto Channel List						
	Card-0: Pillbox		Card-1: Floor		Card-2: Wall	
FlashCam Ch No.	Total Ch No.	PMT ID No.	Total Ch No.	PMT ID No.	Total Ch No.	PMT ID No.
0	0	Pulser	24	201	48	401
1	1	–	25	202	49	402
2	2	–	26	203	50	403
3	3	–	27	706	51	404
4	4	101	28	206	52	409
5	5	704	29	208	53	410
6	6	102	30	701	54	501
7	7	705	31	703	55	502
8	8	708	32	301	56	503
9	9	104	33	302	57	504
10	10	709	34	303	58	507
11	11	105	35	304	59	508
12	12	710	36	305	60	509
13	13	707	37	306	61	510
14	14	–	38	307	62	602
15	15	–	39	308	63	603
16	16	–	40	309	64	605
17	17	–	41	310	65	606
18	18	–	42	311	66	607
19	19	–	43	312	67	608
20	20	–	44	–	68	609
21	21	–	45	–	69	610
22	22	–	46	–	70	702
23	23	–	47	–	71	–

Table 8.1: The distribution of PMTs across three FlashCam cards. Card-0 (highlighted in yellow) contains all the PMTs from the Pillbox, including the pulser (connected to channel-0), along with the corresponding FlashCam channel number assignments and the total number of channels. Card-1 (displayed in green) hosts all the PMTs located on the floor of the water tank. Card-2 (shown in blue) contains all the PMTs from the wall of the tank.

nal simultaneously within a time window of "Δt" and "D_{dark}" represents the dark rate of the PMTs. For our case, the dark count rate of the photomultipliers is $D_{dark} = 6000Hz$, and the coincidence window Δt is set at 60 ns. With these settings, multiple trigger conditions were checked. As a result, the majority level of 3 out of 10 PMTs from the Pillbox (Card-0), 4 out of 20 PMTs from the floor (Card-1), and 4 out of 24 PMTs from the wall (Card-2) of the water tank were chosen where the least random coincidences were expected. Therefore, for the beginning of the LEGEND-200 data taking, these trigger conditions need to be

achieved within a 60ns window to consider the signal as a valid trigger for the muon veto. The trigger threshold for the master card is set to 1 i.e. when at least 1 out of 3 ADC cards trigger, the signal is sent to the master card, and the entire veto is read out by the DAQ system.

New Majority level trigger for the Pillbox: After recording the first muon data with the LEGEND-200 setup, the rate of PMTs from the floor and wall of the water tank was found to be in good agreement with the expectations from GERDA but due to the increase in the number of PMTs in the Pillbox, the rate in this crucial part of the muon veto shows a drastic increase ($\sim$ 1.8 Hz) as compared to GERDA. As a temporary solution, only 4 PMTs (101, 102, 104, and 105) that were already in the pillbox during GERDA were used to establish the trigger condition which was reasonable for generating a trigger from the pillbox. This adjustment significantly brought down the rate to $\sim$ 0.43 Hz, which was low enough to prevent excessive data accumulation.

However, to establish a permanent solution for the pillbox trigger condition, several runs of data during the commissioning of LEGEND-200 were analyzed in a study done in another thesis. The only parameter adjusted for the masking process during this analysis was the majority level for the pillbox PMTs. Various majority levels were tested, specifically 5, 6, 7, 8, 9, and 10 out of the total 10 pillbox PMTs. After evaluating these scenarios, it was observed that with a majority level of 6 out of 10 pillbox PMTs, the triggering PMTs had a more balanced influence, resulting in a more stable rate of about 40 mHz. Therefore the decision was made to implement the trigger condition with a majority level of 6 out of 10 pillbox PMTs while maintaining the previous trigger settings for the floor and wall PMTs. Hence, the new trigger conditions of 6/10 pillbox, 4/20 floor, and 4/24 wall PMTs were selected for normal data taking.

FlashCam Switches to Record Muon Data: The DAQ settings of the LEGEND-200 muon veto system for physics data taking as well as for calibrations in terms of FlashCam PMT switches are described in Appendix D.1. Essentially, these flags instruct the system to record data exclusively from all the channels connected to the PMTs, while skipping the empty channels. In addition to that, these settings include a wide variety of parameters, ranging from event samples

to storage delay, baseline values, pulse shaping, and various trigger thresholds necessary to record muon data. Conveniently, these switches can be executed via command-line instructions, making it effortless to record data with their associated configurations.

8.4 New Software of LEGEND-200

Data Format and Software Package: The data analysis pipeline has been established and implementation of LEGEND-200 specific analysis tools continues. The "root-file" format used in GERDA is now replaced by the more advanced and sophisticated HDF5 (Hierarchical Data Format version 5) format [98] which provides more advanced features like flexibility, portability, and scalable way to store and manage large and complex datasets. LEGEND-200 is using the Python-based waveform analysis tool called "Pygama" [99]. It is an advanced Python-based package used for decoding digitizer data i.e. converting the physics DAQ output to LEGEND LH5-format HDF5 files. It also offers fast Digital Signal Processing (DSP) with NumPy and Numba libraries on time-series data and generating and selecting high-level event data for further analysis.

L200 FlashCam/ ORCA Software: LEGEND-200 binary data is digitized via the FlashCam system. FlashCam is configurable via ORCA (Open Resource Control Architecture) [100] GUI objects or through ORCA scripting. The GUI aspect of this framework is used for the operator interface and control of the DAQ. ORCA reads the data stream from FlashCam and provides real-time monitoring so one can see the source approach the detector array as it lowers during the calibration of Ge detectors and writes data to disk. The ORCA GUI also displays the rate in each individual detector in either a detector array or FlashCam crate view. In addition to that, it also supports the setup of FlashCam ADCs used for the muon veto system (24 channels, 12 bit ADC). ORCA handles run control and manages run/ cycle, or file boundaries. It also supports the dispatching of alarms via email or Slack to a predefined list of experts. For more detail on the data organization and terminologies associated with tier production in LEGEND-200, detailed information can be found in the referenced [101].

Data Processing: To enhance the analysis flexibility, muon veto data is placed alongside Ge and SiPM data within the same files which used to be in separate files in GERDA. The data processing is classified into a multi-tier structure, with each level building upon the previous one. This structure is composed of different tiers (levels), starting with Tier-0 (DAQ data) which contains the binary data, exactly as received from the DAQ system. The next level, Tier-1 (raw data), is constructed by converting DAQ data into HDF5 format that retains the original information from Tier-0 but arranges it in a layout suitable for data analysis. The subsequent Tier-2 (DSP data) contains the output of the Digital Signal Processing (DSP), extracted from the analysis of the single waveforms. The further tier production involves high-level analysis parameters such as calibration of DSP parameters or extraction of other analysis parameters related to detector hits. The process of tier production is conducted using the Pygama software. Each raw file is analyzed independently to generate the corresponding DSP and hit files. Upon completion of the data processing, each run possesses raw and DSP files in the case of the muon veto system and raw, DSP, and hit files in the case of Ge and SiPM data. Raw files primarily contain waveforms and are often too large to be fully loaded into memory. On the other hand, DSP and hit files contain computed values (such as energy, pulse heights, trigger conditions, etc) and are much smaller in size. Therefore, it's a good practice to produce tiers for high-level analysis. In the further analysis of muon veto's DSP files, one can get the total multiplicities of PMTs (or pillbox, floor, and wall multiplicities separately), total integral light in the water tank, timestamps, and channel numbers, muon event rate, and other useful parameters. The DSP config file contains all the necessary parameters for muon data analysis is presented in Appendix D.2.

8.5 Calibartion of PMTs after Refurbishment of the Veto

After the successful modifications of the muon veto system, a thorough examination of each PMT was conducted to ensure their proper functionality. This involved the reactivation of the high voltage of each PMT one by one, following

the same precise voltage settings described in Table 5 of [73], which had been previously optimized for GERDA. The individual voltages of each PMT were adjusted to reach a desired gain factor of 10^7. During this evaluation, the dark rate of each PMT was determined to be in the range of 5-6 kHz for each capsule which is comparable to what was observed for PMTs in GERDA. This precise examination and calibration process was essential to ensure the performance of all PMTs for data taking and analysis in the LEGEND-200 experiment.

The transition from GERDA to LEGEND marked a significant upgrade in the experimental setup, including the electronics used for the calibration of the muon veto PMTs. Much of the existing electronics were replaced with newer, more reliable versions. As part of this transition, the DAC (Digital-to-Analog Converter) and pulser, used in the calibration process of GERDA muon veto, were removed from the setup because of the removal of the electronics crate that previously housed these components. To accommodate this transition and for the sake of convenience in interfacing with the master electronics, which also featured a LAN port, a smaller control setup was devised by the University of Tuebingen. This new setup utilized a Raspberry Pi 4 with 4 GB of RAM, in conjunction with several Integrated Circuits (IC). The pulse signals are produced by switching a logic pin of the Raspberry Pi on and off repeatedly. Other than electronics, the calibration procedure of PMTs remained the same as used in GERDA (see Section 4.4) i.e. five diffuser balls inside the tank were illuminated by using the pulser signals generated by a pulser. This pulser is also connected to the FlashCam channel-0 of card-0 which reads out all the PMTs and triggers the entire veto for each pulse during calibration. As a result, a single photon peak (SPP) of each PMT is recorded and examined. The calibration aimed to achieve an SPP at 30 ADC channels, which allows to record pulses with up to 200 photons within the FlashCam's detection range. Figures 8.7a, 8.7b, and 8.7c show the SPP spectra of three representative PMTs (PMT: 102 from the Pillbox, PMT: 701 from the floor, and PMT: 507 from the wall). In each spectrum, the SPP was calibrated to be centered at the desired 30 channels demonstrating a clear distinction between the pedestal and SPP. The peak-to-valley ratio in these spectra ranged from 2.1 to 3.5, further showing the precision of the calibration. Figure 8.7d illustrates the PMT reso-

lution, which shows minimal deviations in both the peak position and standard deviation of the Gaussian distribution. Additionally, the forward voltages applied to the five diffuser ball LEDs, used to achieve the desired value of 30 ADC channels are mentioned in Table 8.2.

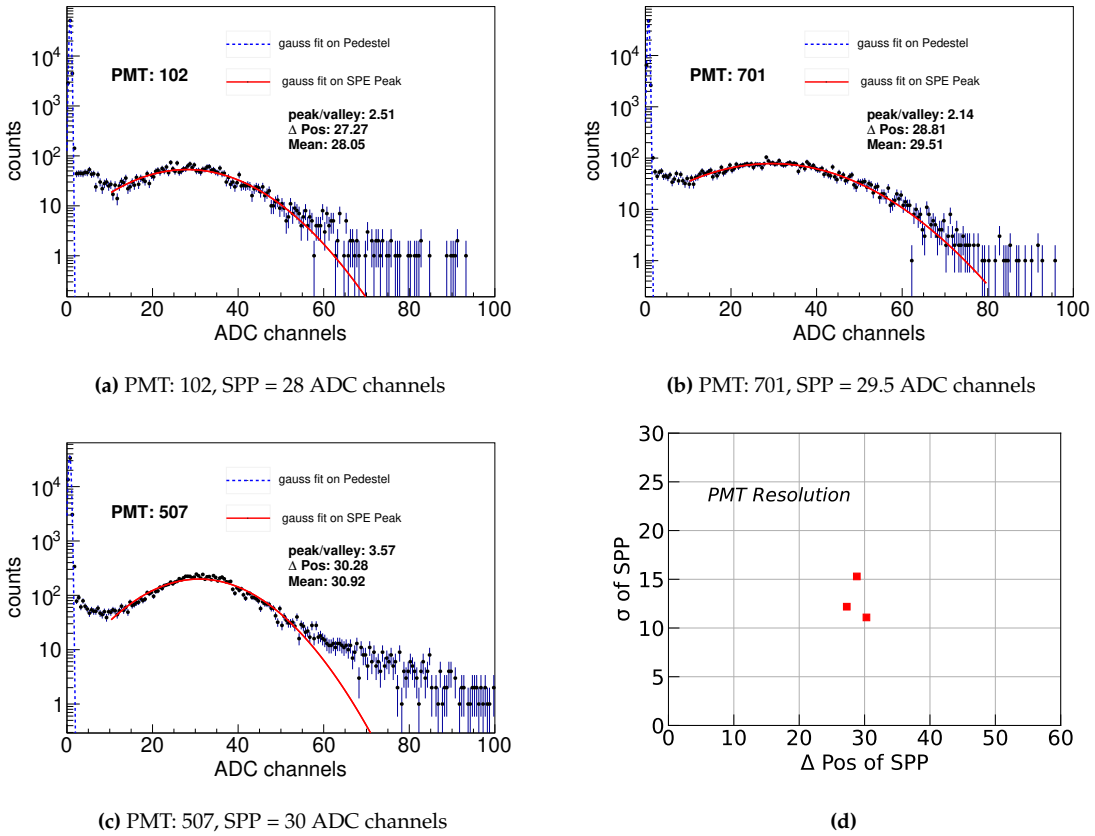

(a) PMT: 102, SPP = 28 ADC channels

(b) PMT: 701, SPP = 29.5 ADC channels

(c) PMT: 507, SPP = 30 ADC channels

(d)

Figure 8.7: Calibrated SPP spectra of three selected PMTs: (a) PMT 102 from the Pillbox, (b) PMT 701 from the floor, and (c) PMT 507 from the wall of the water tank. (d) The PMT resolution is shown as the width of the SPP versus the position of the SPP. Spectra are fitted with Gaussian distributions for both the SPP and pedestal.

The majority of PMTs showed good performance after the refurbishment of the veto, except for three PMTs (204, 207, and 406) that failed to register any pulses after the modifications and hence were disconnected from the FlashCam cards. The location of these PMTs is visually displayed in Figure 8.6. Other than that the peak-to-valley ratio for almost all the PMTs fell within the range of 1.5 to 3.0, which was comparable to their values in GERDA. Hence, the muon veto system was calibrated and fully functional after the refurbishment of the veto. While three new PMTs had broken in addition to the 10 PMTs from GERDA that were already non-operational, the remaining 53 PMTs were working well at the

LED	Forward Voltage [V] @ SPP	Location
1	10.6	water tank, 225°
2	10.6	water tank, 135°
3	10.6	water tank, 45°
4	10.6	water tank, 315°
5	10.3	pillbox

Table 8.2: Forward voltages determined for five diffuser ball LEDs within LEGEND-200 muon veto system. The position of the each of the four diffuser balls in the main tank is given in terms of an angle measured counter-clockwise from the manhole. These four diffuser balls are located at an approximate height equivalent to the 5 meters from the bottom of the tank. The fifth one is located inside the Pillbox.

beginning of LEGEND-200 data taking. To monitor the performance of all PMTs, regular calibrations were conducted during the commissioning runs of LEGEND-200, ensuring the reliability of the veto.

8.6 Analysis of L200 Muon veto

LEGEND-200's muon veto started collecting its physics data in December 2022. During the early commissioning runs of period p02, extensive testing and checks were carried out to ensure the system's reliability and performance. However, the analysis presented in this chapter focused on the commissioning data from later runs: 018 to 020 from period p02 and runs: 01 to 03 from period p03, which are more stable and reliable.

8.6.1 Multiplicity and Integral Light

A fundamental characteristic that defines a muon event is the number of fired PMTs, referred to as the multiplicity (M) of PMTs. A visual representation of the measured multiplicity of all PMTs for the muon events within the above-mentioned dataset is shown in Figure 8.8a. With the highly reflecting foil covering all the surfaces of the steel, and as it also shifts UV light into the visible range, the possibility of an optical photon reaching a PMT becomes higher. Thus, a standard muon should be detected by a high multiplicity of fired PMTs. The

multiplicity spectrum shown in Figure 8.8a exhibits two noticeable peak structures. One peak lies around M > 45, which serves as a regular response of the veto system to authentic muon events. Another peak is located at lower multiplicities i.e. M < 10, referred to as "The low multiplicity bump", which has been historically present since the beginning of GERDA. This structure was studied in detail in the simulations done in [73]. It has been confirmed by those simulations that these events are not caused by muons. Rather, it is hypothesized that the scintillation of VM2000 foil plays a significant role in generating this peak.

Another important characteristic is the integral light in the entire water tank which is plotted in Figure 8.8b with a dual x-axis representation. One axis denotes the detected light, while the other corresponds to the muon track length calculated from the light. The figure shows the diverse range of detected photoelectrons (p.e) inside the water tank, spanning from a few p.e. up to ten thousand p.e. The characteristic mean free path length of light in water is in the order of 10 meters. Notably, one can observe a nice steep drop occurs around 10 m, aligning with the maximum track length for a traversing muon i.e. a geometrical cutoff. Also, a huge bump at lower light intensities, corresponding to shorter tracks (ranging from 10 to 30 cm) is visible. However, investigations through simulations, as detailed in [73], have indicated that this considerable peak observed at shorter distances, in the measured light histogram, is not attributed to muon events. Based on the outcomes of that simulation study, a decision was made to implement a relatively straightforward criterion: a cut based on the recorded integral light ($\geq$ 30 p.e) which corresponds to the muon events with a track length of 60 cm within the water tank. This cut effectively removes the impact of the bump without excessively cutting valid muon events.

8.6.2 Conditions to Identify Muons

In Figure 8.9, the total integral light within the water tank is plotted against the total multiplicity of PMTs. One can clearly observe the hot spot in the lower-left corner of the plot, which corresponds to events that are not classified as muons. Thus the final muon event selection cut was defined to include either those events, that possess an integral light measurement of at least 30 p.e or a total multiplicity of

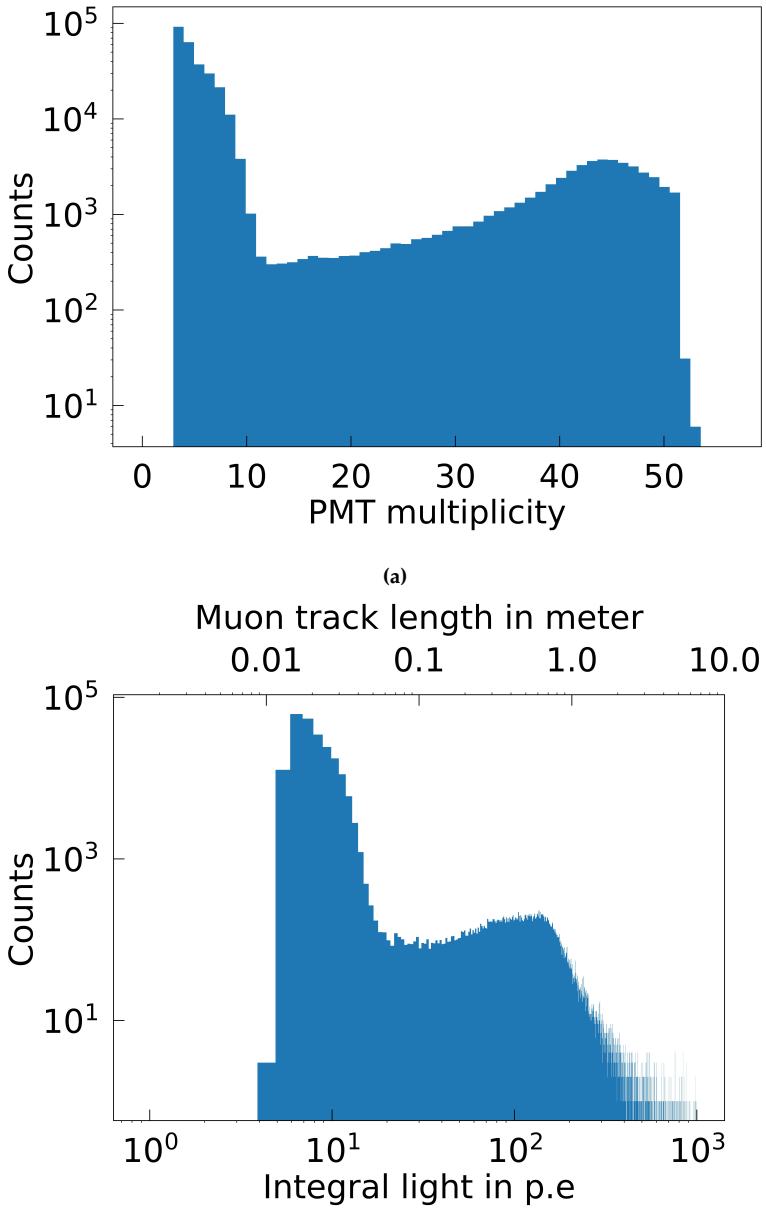

Figure 8.8: (a) Measured multiplicity spectrum of the Cherenkov PMTs. (b) Total integral light in the water tank.

at least 10 PMTs or both. These cut conditions are set in a way to remove the low multiplicity bump out of all the events as indicated by red lines in Figure 8.9. This criterion has been used to identify muons throughout the GERDA data analysis, and it continues to be used for the ongoing LEGEND-200 data.

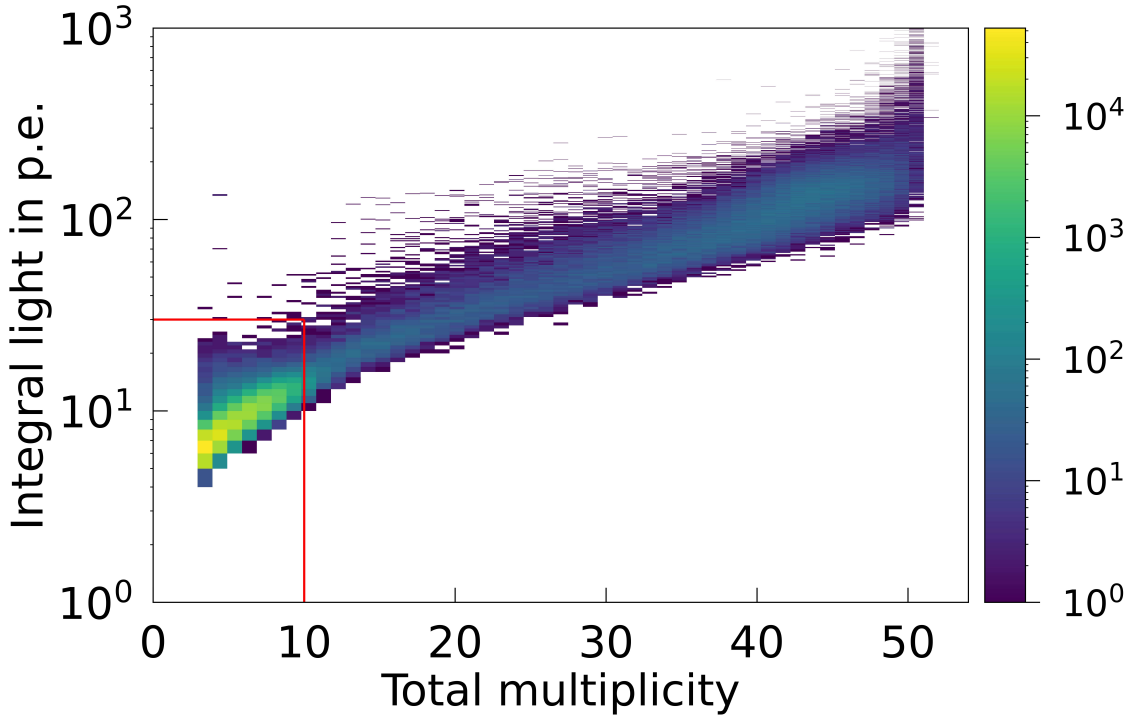

Figure 8.9: Integral light measured in the whole water tank versus the PMT multiplicity. The observed light in the water tank varies from a few p.e. up to several ten thousands of p.e. The "hot spot" at the lower-left portion of the spectrum represents the low multiplicity bump equivalent to low light in the spectrum. The red lines represent the precise cut conditions for the identification of true muon events within the data.

8.7 Monitoring of the Veto: Individual Rates of PMTs

The effectiveness of the muon veto system depends on the individual performance of each PMT. This section offers an overview of the individual performance of 54 PMTs after the refurbishment of the veto system. Figure 8.10 shows the muon rates recorded by each PMT over an 18-hour duration during run-000 of data collection within the data-taking period p03. The data of this period was recorded under the trigger conditions of 6 out of 10 PMTs from the Pillbox, 4 out of 20 PMTs from the floor, and 4 out of 24 PMTs from the wall of the water tank, all within a coincidence window of 60 ns. The total trigger rate of the muon veto system approximated 60 mHz, with an overall muon rate of $\sim$ 35 mHz, which is consistent with the overall rate of GERDA muon veto. To identify muon events, conditions requiring either a total multiplicity of at least 10 PMTs or a total integral light of at least 30 p.e., or both, were applied in plotting these

rates. Figure 8.10a shows the individual rates of all the PMTs from the Pillbox, while Figures 8.10b and 8.10c display the rates from the floor and wall PMTs, respectively. It can be seen from these figures that the operational PMTs exhibited only minimal variations in their rates and are consistent with their expected rates from GERDA [65]. However, this one PMT (608) from the wall highlighted blue in Figure 8.10c, experienced a temporary decrease in rate but later returned to its normal value. Unfortunately, two PMTs: 202 and 502, located on the tank floor and wall, stopped working at the end of January and the start of February 2023, respectively as indicated in Figures 8.10b and 8.10c. Overall, the individual PMT rates, as measured under these trigger conditions, are in good agreement with the expectations from GERDA. While the PMT loss rate has increased to 2-3 PMTs per year, compared to the previous rate of 1-2 PMTs per year in GERDA, muon veto still maintains a sufficient number of functioning PMTs to ensure the stability of the veto system for several more years.

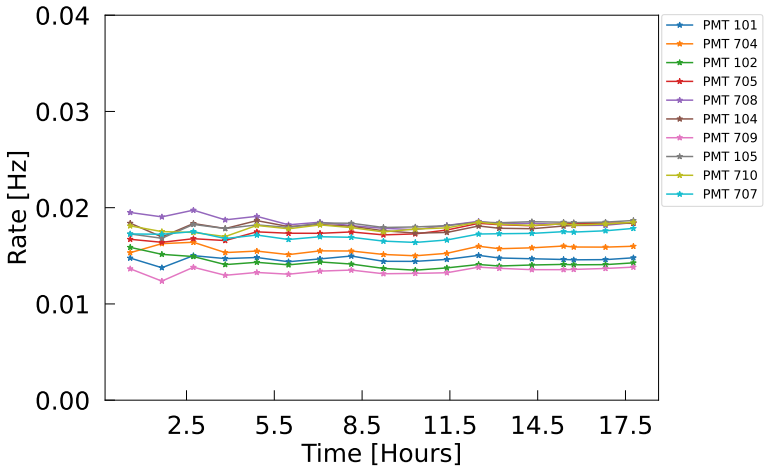

(a)

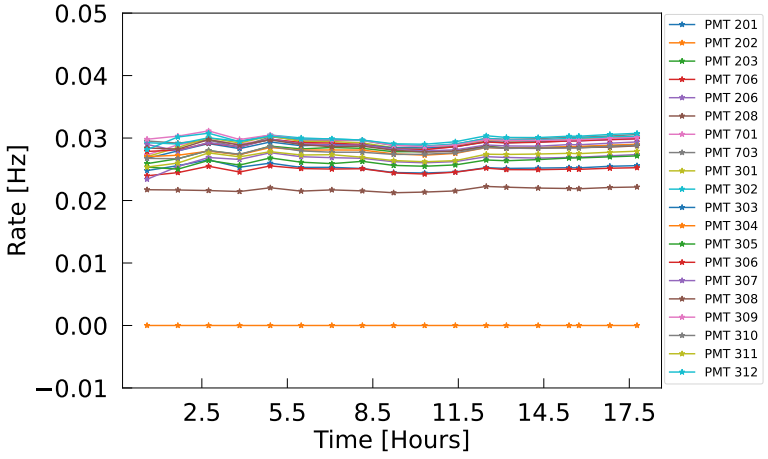

(b)

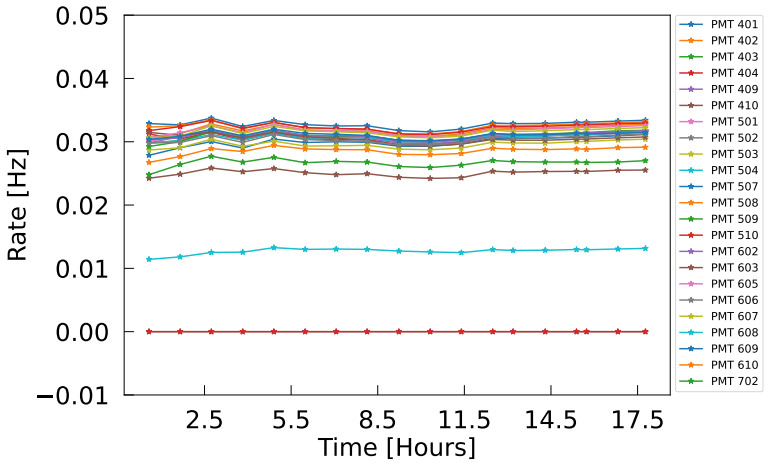

(c)

Figure 8.10: Individual rates recorded by all (a) Pillbox PMTs, (b) PMTs located on the floor, and (c) PMTs located on the wall of the water tank over a time span of 18 hours.

Chapter 9

Summary and Conclusion

In this work, the entire GERDA Phase II and Phase II+ data was analyzed for direct and indirect muonic backgrounds as well as for radioactive background peak search of ^{137}Cs in the data. MC simulations were employed to study the impact of modifications of the muon veto system. Furthermore, the commissioning data of the muon veto of LEGEND-200 was analyzed in this thesis. In addition, the muon veto was under observation throughout the entire duration of this thesis, ensuring the overall excellent performance of the veto.

Neutrinoless double beta ($0\nu\beta\beta$) decay represents the more feasible way for exploring the Majorana nature of neutrinos, i.e., whether neutrinos are their own antiparticles. The GERDA experiment was designed with the ambitious goal of conducting a background-free search for this process using enriched high purity ^{76}Ge detectors. Located at the Laboratori Nazionali del Gran Sasso in Italy, GERDA operated these detectors in liquid argon, accumulating a substantial total exposure of 127.2 kg·yr through the combined efforts of Phase I and Phase II. GERDA concluded its data-taking in November 2019 without detecting any evidence of neutrinoless double beta decay. The experiment however, established a remarkable lower limit of $T^{0\nu}_{1/2} > 1.8 \times 10^{26}$ yr at 90% C.L. for ^{76}Ge with a low background index of $(5.2^{+1.6}_{-1.3}) \times 10^{-4}$ counts/(keV·kg·yr).

The next genertaion of $0\nu\beta\beta$-decay search aims to push the boundaries further. With the intent of probing half-lives in the range of 10^{27} yr, LEGEND-200 aspires to collect a design exposure of 1 t·yr over a span of 5 years, and LEGEND-1000 ultimately aims to achieve sensitivity in the range of 10^{28} yr with a design exposure

of 10 t·yr. Operating within the same infrastructure as GERDA, LEGEND-200 has adapted to accommodate 200 kg of enriched ^{76}Ge detectors within the liquid argon cryostat.

The GERDA Cherenkov veto system, designed to detect muons within the experimental setup, has served very well throughout the entire operational lifetime of GERDA. Within the context of this thesis, a detailed investigation of muon events within the germanium detectors were studied, shedding light on two distinct classes of muon interactions: prompt energy deposition and slightly delayed events caused by secondary particles from the surrounding environment. By examining muon-Ge coincident events within a time window of 10 μs, a total of 4870 such events were recorded over the course of GERDA's Phase II and Phase II+ data. The effectiveness of the muon veto system is reflected in the significant reduction of the background index within a region of interest (ROI). Without the muon veto, the background index (BI) would have been as high as 2.25×10^{-3} counts/(keV $\cdot$ kg $\cdot$ yr). Notably, after the application of various analysis cuts, none of the remaining muon background events were observed in ROI, leading to an estimated BI limit of $\sim 36 \times 10^{-6}$ counts/(keV $\cdot$ kg $\cdot$ yr), demonstrating a remarkable degree of background suppression.

Further investigation of the residual muonic background, which remained after all analysis cuts, referred to as the "dangerous muonic background" was conducted. A detailed study revealed that the remaining 142 muon-Ge coincident events were indeed genuine muon events and not caused by any random coincidences. This finding shows the necessity of a muon veto system for future experiments, such as the LEGEND Experiment, highlighting the continuing importance of muon-induced background mitigation in experimental setups. Exploring the potential source of this residual muonic background, a thorough examination was conducted through Monte Carlo (MC) simulations using the Geant4-based MaGe simulation framework. The objective was to replicate the behavior of neutrons within the GERDA setup by utilizing the pre-simulated kinetic energy spectrum of neutrons at the precise position of the LAr cryostat as an input. A result from the comparison of these simulated neutron events with the residual muonic background spectrum, suggests that some of these remaining background events

could plausibly be attributed to neutron interactions.

Ultimately, the data was searched for isotopes generated by muon spallation of argon or subsequent proton activation within the GERDA Phase II and Phase II+ datasets. No characteristic peaks or time signatures of the expected decay were detected. Consequently, statistical analysis using profile likelihood method was conducted to compute upper limits on the production yield of these isotopes, thereby contributing to our knowledge of the GERDA experimental setup's response to muon-induced processes.

During the course of this thesis, the radioactive Cesium-137 background peak was discovered, identified, and analyzed in GERDA Phase II and Phase II+ data. Monte Carlo (MC) simulations via MaGe were conducted to model the ^{137}Cs background originating from various components near the Ge-detector array, including the detectors HV and signal cables, the detector holder plates and bars, and the front-end electronics. The objective was to identify the precise origin of this background peak. The specific activity of ^{137}Cs from these components was calculated via simulations and compared to the activities of these components obtained from material screening. It was observed that the calculated activities for the detector holder plates and bars showed lower values (0.023 mBq/kg and 0.033 mBq/kg) when compared with its upper limit values from screening (<0.13 mBq/kg and < 1.1 mBq/kg) and also in comparison to the other components. Thus the result suggests that the holder plates and bars could be a significant contributor to the ^{137}Cs peak within the entire GERDA Phase II data. With a better understanding of the precise origin of background sources, the LEGEND-1000 experiment will be able to develop new techniques to mitigate these impurities, such as using even lower activity materials, before the assembly of the experiment and thus reduce its background index even further to a predicted value of 0.025 counts /(FWHM$\cdot$ t $\cdot$ yr), effectively reaching a background-free regime.

With the conclusion of GERDA data taking, the existing infrastructure of GERDA was handed over to the LEGEND collaboration for the beginning of the $0\nu\beta\beta$-decay search with LEGEND-200 experiment. However, after the end of GERDA data-taking, the water tank containing the muon veto system was drained for inspection during which two PMTs imploded and their capsules broke. This in-

cident led to the mineral oil from PMTs mixed with the water. While the oil used in the PMTs posed no inherent danger, it raised legitimate concerns regarding the safety and functionality of the muon veto system. Hence for safety purposes, a decision was made to remove oil from all the PMTs. Without the oil, the PMTs would be capable of observing only one-third of the light. To thoroughly evaluate the consequences of this significant reduction in light efficiency, the toy MC simulations nested within the data analysis framework were conducted in this thesis. The outcomes of these simulations were reassuring, suggesting that even in the worst-case scenario, where 2/3 of the light was potentially lost, the sensitivity of the veto remains sufficient. Only 0.1% of the total muon-Ge coincident events were found to be lost. Based on these simulations, the GERDA muon veto was repaired in July 2021. The process involved the careful removal of oil from all PMTs, followed by the secure sealing of the PMTs to protect them from water. Furthermore, the arrangement of PMTs inside the water tank was adjusted, with functional PMTs replacing the damaged ones, ensuring the continuity and reliability of the muon veto system. These adjustments had also been verified through simulations conducted in this thesis.

The LEGEND-200's muon veto started collecting its physics data in December 2022. LEGEND-200 has been through significant changes with the adoption of new technologies, advanced hardware electronics, and sophisticated software enhancements. The new muon veto DAQ system was added to accommodate the PMTs in a new configuration. The new hardware threshold was chosen in a way, that by design a true muon sample is recorded with minimal contamination from random coincidences or other sources of background. The software was updated to new Python-based programming technologies. The first muon veto DSP parameters were implemented during this work. Several tests were conducted to validate the new configuration and modifications of the muon veto system. In addition, a series of regular and more frequent calibrations of the PMTs were carried out during this thesis, ensuring the good performance of the veto even after the repair procedure. Despite the fact that a few more PMTs have malfunctioned since the repair of the veto, the muon veto continues to perform exceedingly well, affirming its pivotal role in the ongoing success of the LEGEND-200 experiment.

Appendix A

Waveforms of the events

The waveforms of some of the remaining Ge-μ coincident events are shown here.

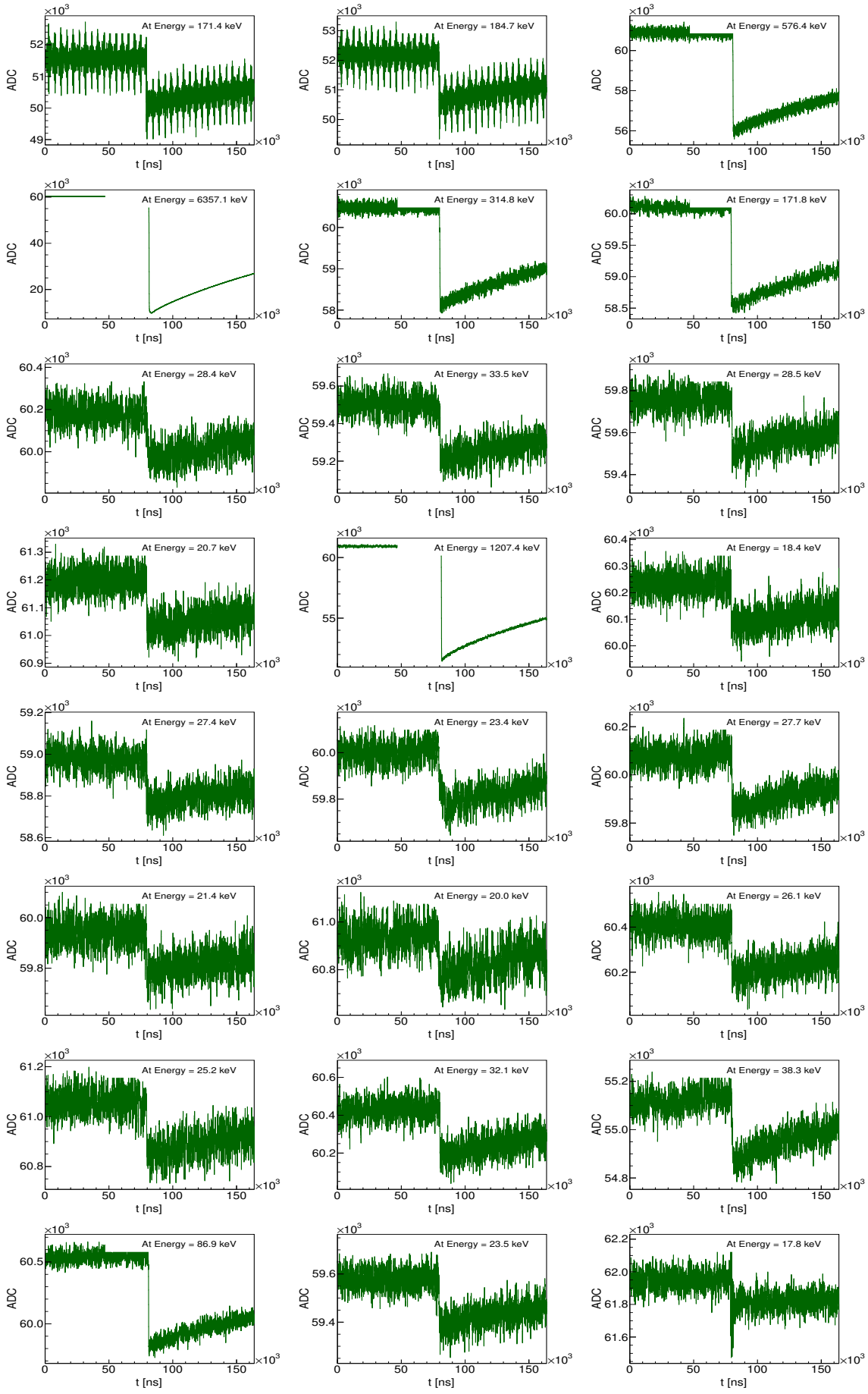
At Energy = 171.4 keV
At Energy = 184.7 keV
At Energy = 576.4 keV
At Energy = 6357.1 keV
At Energy = 314.8 keV
At Energy = 171.8 keV
At Energy = 28.4 keV
At Energy = 33.5 keV
At Energy = 28.5 keV
At Energy = 20.7 keV
At Energy = 1207.4 keV
At Energy = 18.4 keV
At Energy = 27.4 keV
At Energy = 23.4 keV
At Energy = 27.7 keV
At Energy = 21.4 keV
At Energy = 20.0 keV
At Energy = 26.1 keV
At Energy = 25.2 keV
At Energy = 32.1 keV
At Energy = 38.3 keV
At Energy = 86.9 keV
At Energy = 23.5 keV
At Energy = 17.8 keV
ADC
t [ns]
×10³

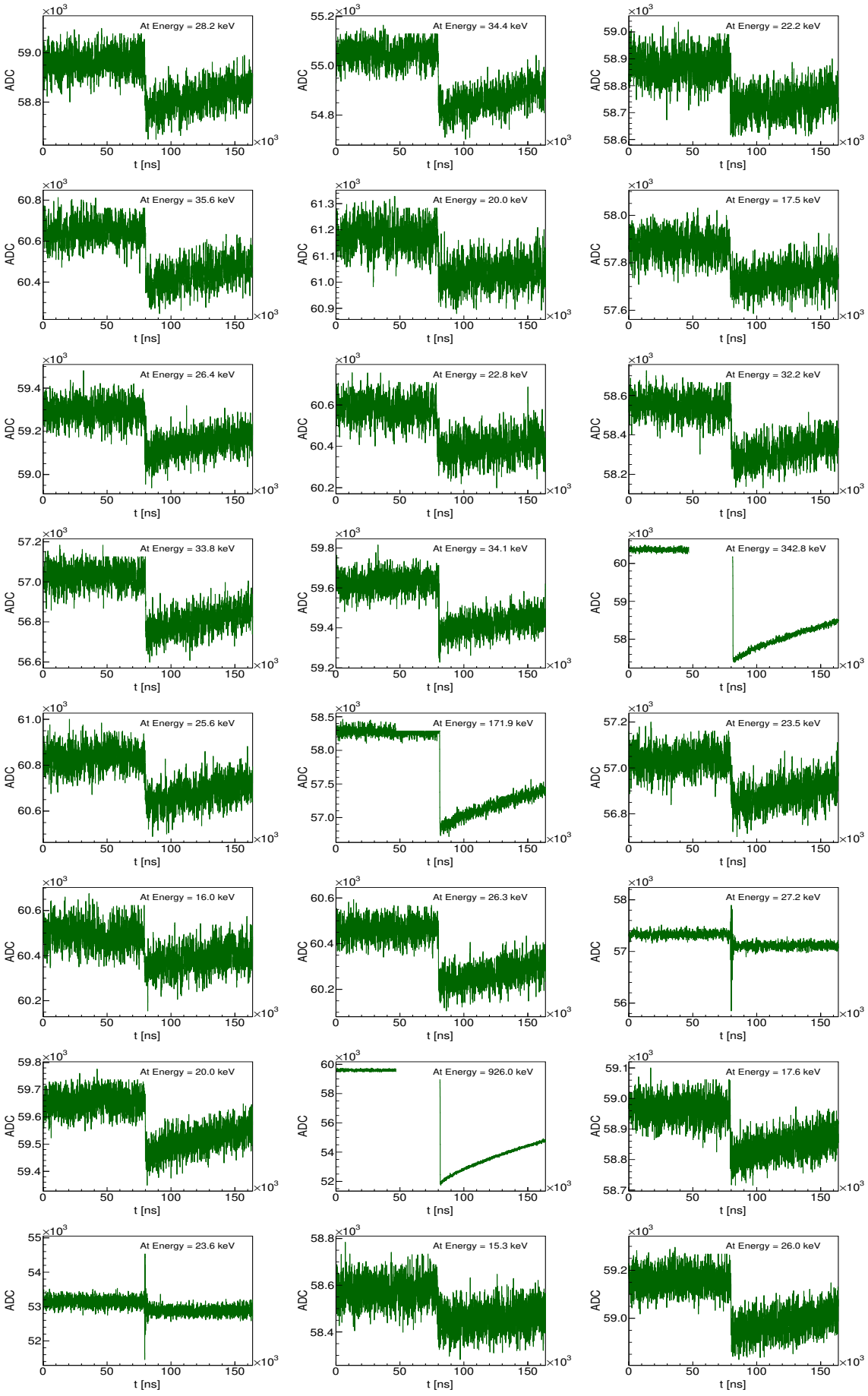
At Energy = 28.2 keV
At Energy = 34.4 keV
At Energy = 22.2 keV
At Energy = 35.6 keV
At Energy = 20.0 keV
At Energy = 17.5 keV
At Energy = 26.4 keV
At Energy = 22.8 keV
At Energy = 32.2 keV
At Energy = 33.8 keV
At Energy = 34.1 keV
At Energy = 342.8 keV
At Energy = 25.6 keV
At Energy = 171.9 keV
At Energy = 23.5 keV
At Energy = 16.0 keV
At Energy = 26.3 keV
At Energy = 27.2 keV
At Energy = 20.0 keV
At Energy = 926.0 keV
At Energy = 17.6 keV
At Energy = 23.6 keV
At Energy = 15.3 keV
At Energy = 26.0 keV
ADC
t [ns]
×10³

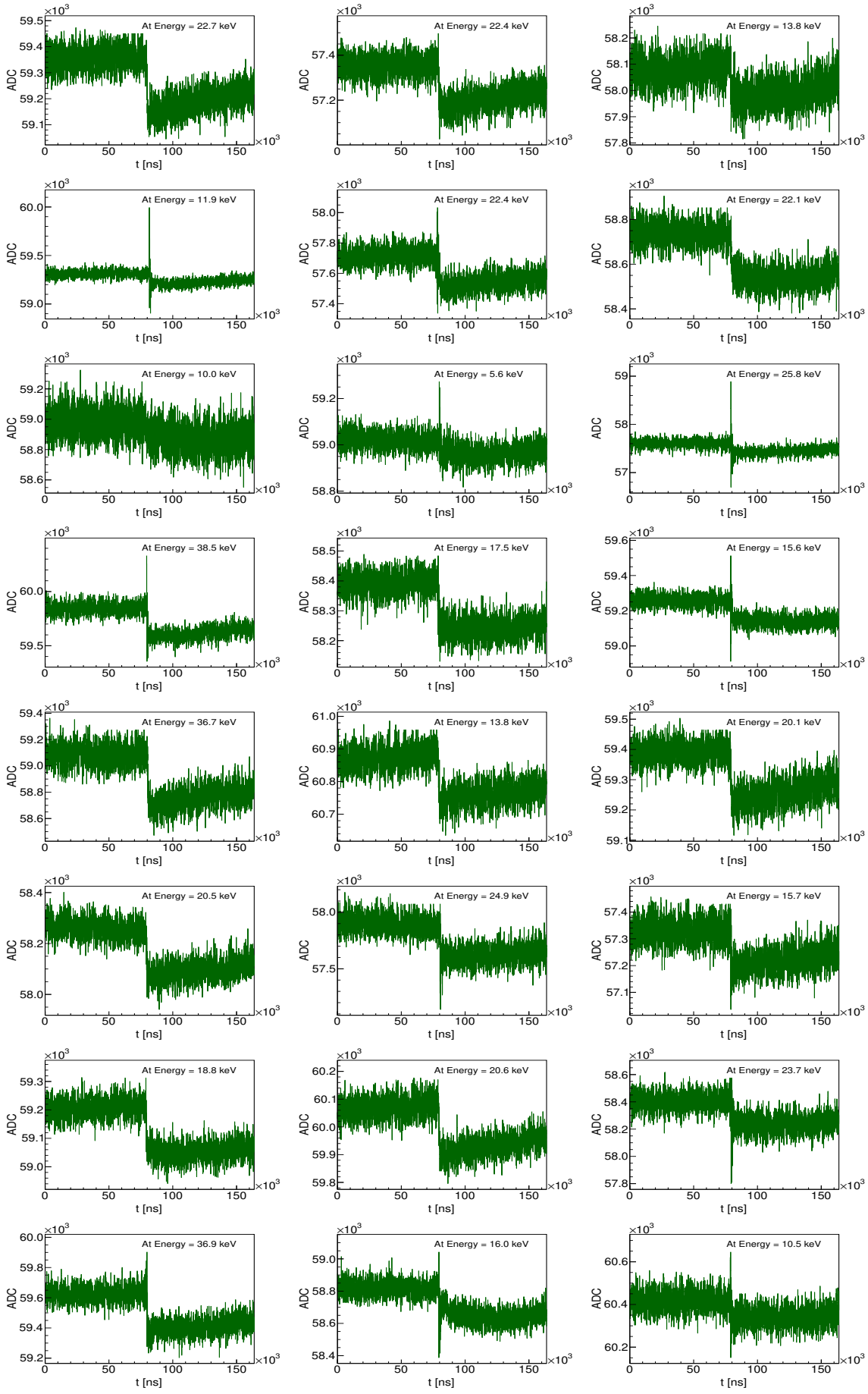
At Energy = 22.7 keV
At Energy = 22.4 keV
At Energy = 13.8 keV
At Energy = 11.9 keV
At Energy = 22.4 keV
At Energy = 22.1 keV
At Energy = 10.0 keV
At Energy = 5.6 keV
At Energy = 25.8 keV
At Energy = 38.5 keV
At Energy = 17.5 keV
At Energy = 15.6 keV
At Energy = 36.7 keV
At Energy = 13.8 keV
At Energy = 20.1 keV
At Energy = 20.5 keV
At Energy = 24.9 keV
At Energy = 15.7 keV
At Energy = 18.8 keV
At Energy = 20.6 keV
At Energy = 23.7 keV
At Energy = 36.9 keV
At Energy = 16.0 keV
At Energy = 10.5 keV
ADC
t [ns]
×10³

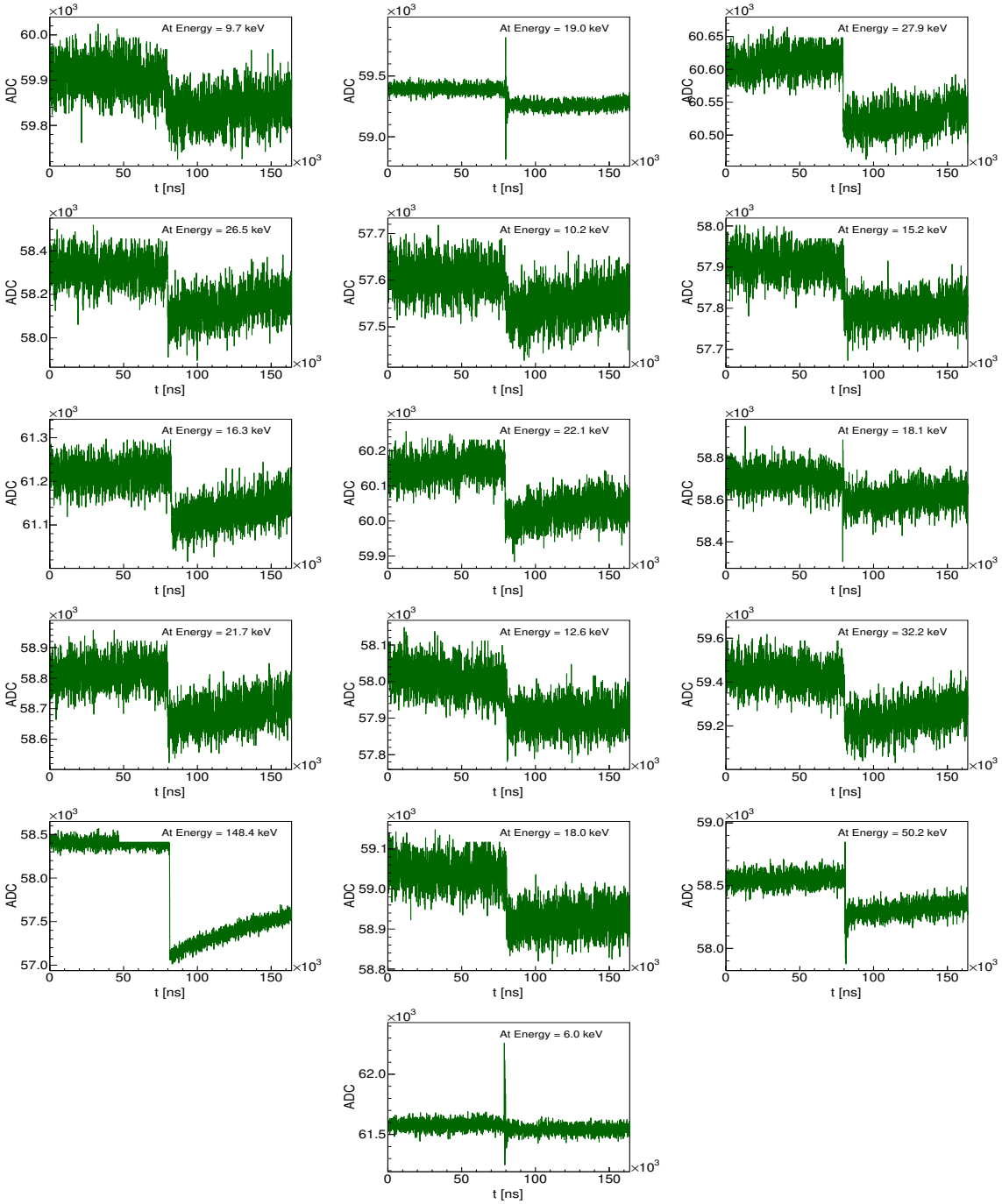
At Energy = 9.7 keV
At Energy = 19.0 keV
At Energy = 27.9 keV
At Energy = 26.5 keV
At Energy = 10.2 keV
At Energy = 15.2 keV
At Energy = 16.3 keV
At Energy = 22.1 keV
At Energy = 18.1 keV
At Energy = 21.7 keV
At Energy = 12.6 keV
At Energy = 32.2 keV
At Energy = 148.4 keV
At Energy = 18.0 keV
At Energy = 50.2 keV
At Energy = 6.0 keV
ADC
t [ns]
×10³

Appendix B

Cosmogenic Peak Search

The table containing isotopes from proton spallation of argon with their possible decay modes, intensities and end point energies are represented in Table B.1. The energy region around the expected γ-line $\pm$50 keV window of the four isotopes ^{29}Al, ^{27}Mg, ^{22}Na and ^{24}Na and their corresponding p-value distributions are presented in Figure B.1.

Table B.1: Isotopes from Proton Spallation of Argon [83]: Possible Decay Modes, Intensities and Endpoint Energies.

Isotope	Decay	Half-life [$T_{1/2}$]	Energy [keV]	Intensity [%]
^{38}Cl	IT	715 ms	671	99.9
	β^-	37.2 m	4920	55.6
	β^-		2750	11.3
	γ		1640	33.3
	γ		2170	44.4
^{39}Cl	β^-	55.6 m	1920	83
	β^-		2180	4.5
	β^-		3440	7.1
	γ		250	46.1
	γ		1267	53.6
	γ		1520	39.2
^{37}S	β^-	5.05 m	1760	94.0
	β^-		4870	5.6
	γ		3100	93.9
^{22}Na	β^+	2.6 y	550	90.3
	γ		1274	99.9
^{28}Al	β^-	2.25 m	2860	99.9
	γ		1780	100
^{24}Na	β^-	14.9 h	1390	99.9
	γ		1368	99.9
	γ		2750	99.9
^{28}Mg	β^-	20.9 h	460	94.8
	γ		940	36.3
	γ		1342	54
^{29}Al	β^-	6.56 m	1250	6.3
	β^-		2400	89.9
	γ		1273	91.3
	γ		2430	5.2
^{27}Mg	β^-	9.5 m	1600	29.1
	β^-		1770	70.9
	γ		840	71.8
	γ		1015	28.2

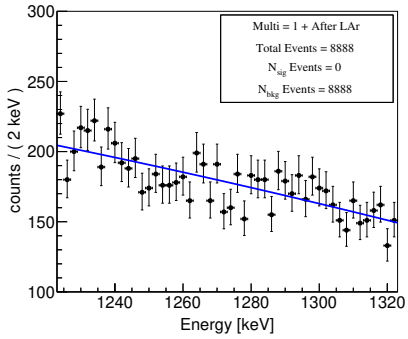

(a) 1273 keV $\pm$ 50 keV γ in ^{29}Al

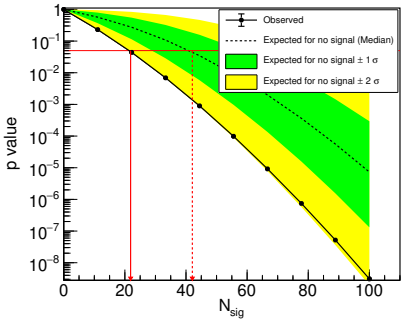

(b) $N_{sig} < 22$ counts (95% CL)

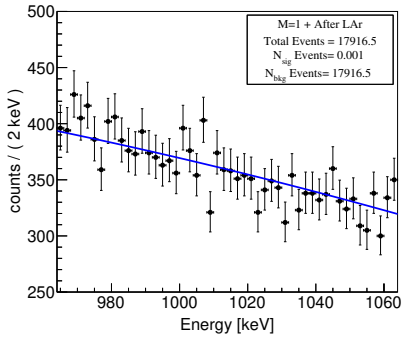

(c) 1015 keV $\pm$ 50 keV γ in ^{27}Mg

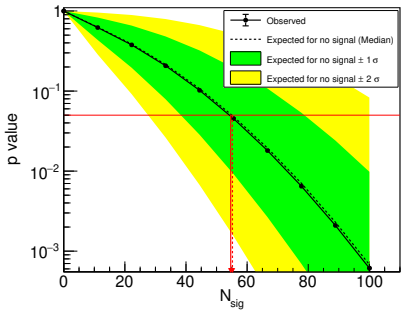

(d) $N_{sig} < 55.6$ counts (95% CL)

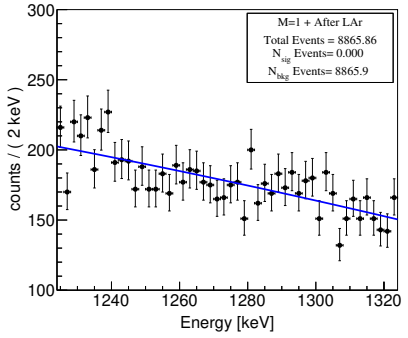

(e) 1274 keV $\pm$ 50 keV γ in ^{22}Na

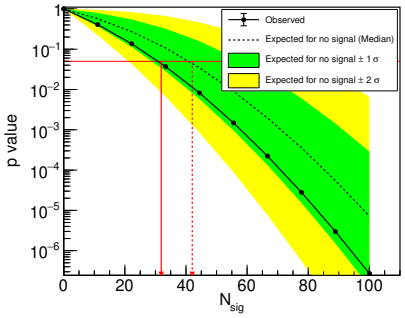

(f) $N_{sig} < 32$ counts (95% CL)

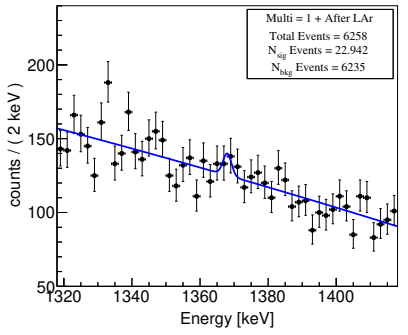

(g) 1368 keV $\pm$ 50 keV γ in ^{24}Na

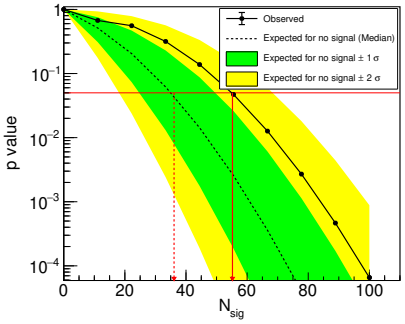

(h) $N_{sig} < 55.2$ counts (95% CL)

Figure B.1: Energy windows and their corresponding p-value distributions for the γ-lines of isotopes ^{29}Al, ^{27}Mg, ^{22}Na and ^{24}Na.

Appendix C

Cesium Background Peak Analysis

MC simulated spectra of ^{137}Cs decays in the enriched HPGe detectors with a source origin in individual parts of the cables such as HV and Signal cables at the Holder as well as HV and Signal cables from the Holder to the Electronic Plate and at the end with source origin in front-end electronics (CC3) are presented in Figures C.1 and C.2.

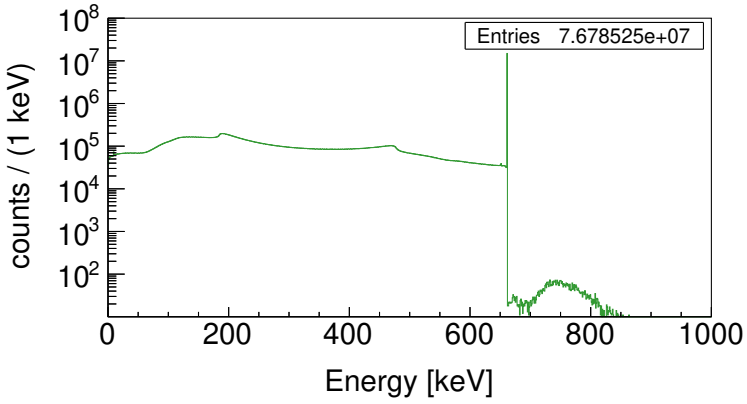

(a) ^{137}Cs MC simulations with the source origin in the HV cables at holder.

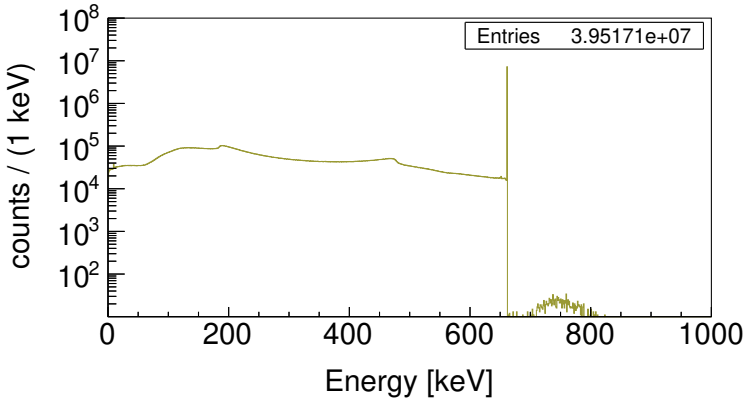

(b) ^{137}Cs MC simulations with the source origin in the HV cables from holder to electronic plate.

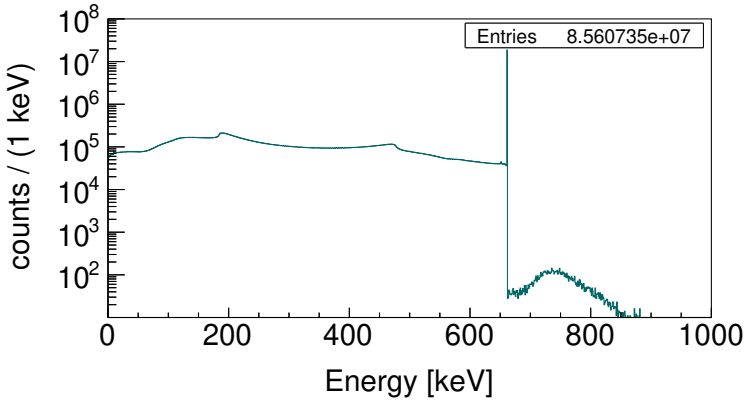

(c) ^{137}Cs MC simulations with the source origin in the signal cables at holder.

Figure C.1: Simulated signature of ^{137}Cs decays in the enriched HPGe detectors with a source origin in individual parts of the cables (a) HV Cables at Holder, (b) HV Cables from Holder to Electronic Plate and (c) Signal Cables at Holder.

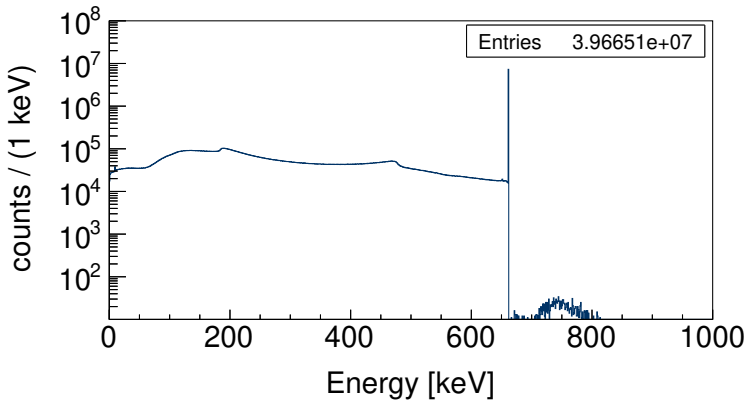

(a) ^{137}Cs MC simulations with the source origin in the signal cables from holders to electronic plate.

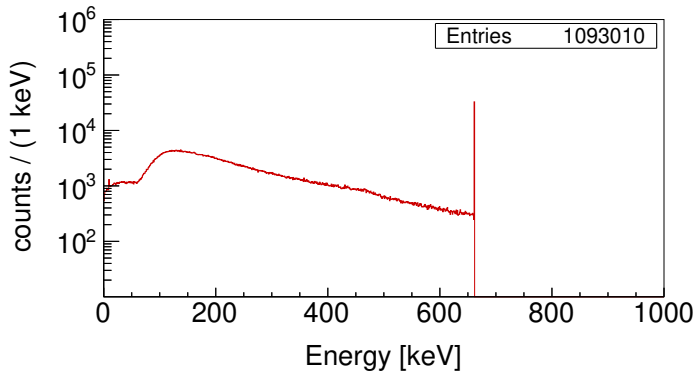

(b) ^{137}Cs MC simulations with the source origin in the front-end electronics.

Figure C.2: Simulated signature of ^{137}Cs decays in the enriched HPGe detectors with a source origin in (a) Signal Cables from Holder to Electronic Plate and (c) Front-end electronics (CC3).

Appendix D

L200 Data Settings

D.1 FlashCam PMT setup/ Switches for the readout program

FlashCam modules are addressed with a three-digit HEX address 0xHHH. Thus LEGEND-200 is using addresses in the form of 0xHH0. FlashCam is very flexible in its configuration. The readout program uses a very flexible way to program a range of channels/modules/entities i.e. switch value, start-entity, number of entities. These switches can be applied on the command line to record data with its relevant settings. The muon veto master card in terms of HEX address is 0xf0 and is connected to three ADCs 0x10 0x20 0x30.

For Physics Data Mode: LEGEND-200 muon veto DAQ settings for physics data taking in terms of FlashCam switches are the following:

- es (event samples) 220
- sd (storage delay) 100
- bl (baseline) 1000
- dm (daq mode) 2
- pz (pole-zero) 0
- fs (fast shape) 12
- ss (slow shape) 12
- athr (threshold for channels) 0 (set all to disable first)

CARD-0

- am (switched off empty channels in CARD-0) 3FF0, 0, 1
- athr (set threshold to 15 for ADC channel 4 - 10) 15, 4, 10
- amajl (set ADC majority level i.e. 6/10, card-range) 6, 0, 1
- amajw (set ADC majority width, card-range) 15, 0, 1

CARD-1

- am (switched off empty channels in CARD-1) FFFFF, 1, 1
- athr (set threshold to 15 for ADC channel starting from 24 and go ahead 48 channels) 15, 24, 48
- amajl (set ADC majority level i.e. 4/20, card-range) 4, 1, 1
- amajw (set ADC majority width, card-range) 15, 1, 1

CARD-2

- am (switched off empty channels in CARD-2) FFFFFF, 2, 1
- amajl (set ADC majority level i.e. 4/24, card-range) 4, 2, 1
- amajw (set ADC majority width, card-range) 15, 2, 1

For Calibration Mode: The DAQ settings for the calibration of PMTs in terms of FlashCam switches after starting the pulser are as follows: -dm 2 -bl 1000 -athr 0 -es 500 -sd 50 -am 3FF1,0,1 -am FFFFF,1,1 -am FFFFFF,2,1 -athr 500,0,1 -o calib_file.fcio

D.2 The config-file for muon veto to generate 'DSP' data files

The configuration file shown in Figure D.1 designed for muon veto contains a comprehensive set of parameters that have been extracted from the analysis of individual waveforms, specifically the outcomes of the Digital Signal Processing (DSP). This particular file serves as an essential input in the process of transforming raw data into digital signal-processing data. It contains a collection of computed values, including mean and standard deviation of the baseline, waveforms with baseline subtraction applied, pulse heights associated with each PMT, and various trigger conditions. These parameters collectively facilitate the conversion and subsequent analysis of raw data. The DSP data further enables the extraction of important parameters such as the multiplicity of PMTs, the total integral light within the water tank, and the event rates recorded by each individual PMT, etc.

Figure D.1: The DSP config-file of muon veto.

My Contributions to GERDA / LEGEND-200

In this work, if an image is borrowed from someone else's work, then the credit has been given to the creator of the image in the caption. The results obtained in Chapters 5, 6, and 7 are original contributions of this thesis and are not borrowed from any other source. The calibrations and monitoring of the muon veto system of GERDA, mentioned in Chapter 4 is also the work of this thesis. Chapter 8 represents a collaborative effort within the muon veto collaboration, with the author actively participating in the software development part. Additionally, the analysis of muon data presented in Chapter 8 is carried out by the author. The more detailed understanding of the content and contributions in each chapter are mentioned below:

Chapter 1, 2 and 3 provide a review of neutrino physics and introduce the GERDA and LEGEND experimental setups, as well as background reduction techniques developed within the GERDA collaboration. The background reduction techniques are used as a selection criterion for data analysis but were not developed by the author. The author of this work is not involved in any of those productions.

Half of Chapter 4 contains a review of the hardware and software components of the GERDA muon veto, which were previously developed in theses at the University of Tuebingen. The author was not involved in this part of the work too. However, the latter sections of Chapter 4, specifically Sections 4.4 and 4.5, focus on the calibrations and monitoring of the GERDA muon veto system, which was conducted by the author.

As stated in the opening paragraph, the results obtained in Chapters 5, 6,

and 7 are the original part of this work and were not borrowed from external sources. Most of the simulations in this work were performed using the Geant4-based MAGE simulation framework which was developed and maintained by the GERDA and MAJORANA collaborations. Additionally, the statistical analysis in this work was performed using the RooPlot/RooStat software which is commonly used for statistical modeling and analysis in high-energy physics and other related fields.

Chapter 8 primarily focuses on the refurbishment of the muon veto for the LEGEND-200 experiment at LNGS laboratory, a collaborative effort undertaken by the entire group at the University of Tuebingen. The author was also a part of that operation. However, it's important to note that the development of the new data acquisition system (DAQ) and hardware electronics for calibration of the LEGEND-200 muon veto was not within the scope of the author's work. Nevertheless, the author made contributions by developing the digital-signal-processing (DSP) configuration parameters. These parameters included pulse heights of the PMT signal, integral light measurements in p.e, PMT multiplicity as well as baseline mean and sigma, etc. These parameters were extracted from the analysis of individual waveforms and played a vital role in the subsequent analysis of muon data within the LEGEND-200 experiment. Furthermore, the author conducted several tests during the commissioning of the muon veto's LEGEND-200 data and handled regular calibrations and monitoring of the muon veto system during this commissioning phase. All the analysis plots presented in Chapter 8 were generated by the author.

Acknowledgments

This work would not have been possible without the constant support of my supervisor Prof. Dr. Josef Jochum. I will always be indebted to him for providing me with this opportunity to work with them and learn from him. I would like to express my sincere thanks to my colleagues, Dr. Andreas Zschoke and Dr. Annkathrin Schutez, who not only served as mentors but also as friends during my Ph.D. Their invaluable insights and support played a pivotal role in shaping the outcome of this work.

I am very grateful to all my family members and friends, who stood by me during this challenging journey. My husband, Immad Ahamd was very patient and helpful to me all the time. He supported me throughout the Ph.D., ensuring my comfort and well-being. I am particularly thankful to my friend Shahid, whose support and encouragement provided relief during the tough phases of my Ph.D. His kindness and generosity in offering assistance whenever needed is a reflection of his exceptional character. He not only motivated and uplifted me during my lowest moments but also was very kind to take the time from his busy schedule to read my thesis and provide useful comments, for which I am truly appreciative.

I also want to extend my thanks to my friends Sibgha, Shaguffta, Ali, Shayan, Chiragh, and Bilal, who have cheered me up with their presence and with nice spicy food. Other friends like Stephen, Taner, Victor, and Cathia have assured me that I am competent enough to finish this work. Dario, Janmejay, and Micheal encouraged and cheered me up during the challenging process of thesis writing.

Thanks to all my fellow group members from the Physikalisches Institut including Lukas and Katharina who made the research experience both joyful and comforting.

To all those who have played a part in my academic journey, your contributions, whether big or small, have left a memorable mark on my life, and I am extremely grateful for your presence and support.

References

[1] Clyde L Cowan Jr et al. “Detection of the free neutrino: a confirmation”. In: *Science* 124.3212 (1956), pp. 103–104.

[2] Wei-Ming Yao et al. “Review of particle physics”. In: *Journal of Physics G: Nuclear and Particle Physics* 33.1 (2006), p. 1.

[3] S Fukuda et al. “Determination of solar neutrino oscillation parameters using 1496 days of Super-Kamiokande-I data”. In: *Physics Letters B* 539.3-4 (2002), pp. 179–187.

[4] Wolfgang Hampel et al. “GALLEX solar neutrino observations: Results for GALLEX IV”. In: *Physics Letters B* 447.1-2 (1999), pp. 127–133.

[5] Takeshi Araki et al. “Measurement of neutrino oscillation with KamLAND: Evidence of spectral distortion”. In: *Physical review letters* 94.8 (2005), p. 081801.

[6] Y Ashie et al. “Evidence for an oscillatory signature in atmospheric neutrino oscillations”. In: *Physical review letters* 93.10 (2004), p. 101801.

[7] Y Abe et al. “Reactor ν e disappearance in the Double Chooz experiment”. In: *Physical Review D* 86.5 (2012), p. 052008.

[8] MH Ahn et al. “Measurement of neutrino oscillation by the K2K experiment”. In: *Physical Review D* 74.7 (2006), p. 072003.

[9] Fumihiko Suekane. *Neutrino oscillations: a practical guide to basics and applications*. Vol. 898. Springer, 2015.

[10] Pablo F de Salas et al. “2020 global reassessment of the neutrino oscillation picture”. In: *Journal of High Energy Physics* 2021.2 (2021), pp. 1–36.

[11] X Qian and P Vogel. “Neutrino mass hierarchy”. In: *Progress in Particle and Nuclear Physics* 83 (2015), pp. 1–30.

[12] Luigi Pertoldi. “Sensitivity to the neutrino mass hierarchy with the JUNO experiment”. In: (2015).

[13] Paul Adrien Maurice Dirac. “The quantum theory of the electron”. In: *Proceedings of the Royal Society of London. Series A, Containing Papers of a Mathematical and Physical Character* 117.778 (1928), pp. 610–624.

[14] Richard P Feynman and Murray Gell-Mann. “Theory of the Fermi interaction”. In: *Physical Review* 109.1 (1958), p. 193.

[15] Matteo Agostini et al. “Toward the discovery of matter creation with neutrinoless β β decay”. In: *Reviews of Modern Physics* 95.2 (2023), p. 025002.

[16] AS Barabash. “Average and recommended half-life values for two-neutrino double beta decay”. In: *Nuclear Physics A* 935 (2015), pp. 52–64.

[17] Michael Dürr. “Phenomenological aspects of theories for baryon and lepton number violation”. PhD thesis. 2013.

[18] Benjamin JP Jones. “The physics of neutrinoless double beta decay: A primer”. In: *arXiv preprint arXiv:2108.09364* (2021).

[19] N Abgrall et al. “LEGEND-1000 preconceptual design report”. In: *arXiv preprint arXiv:2107.11462* (2021).

[20] Valerio D’Andrea. “Improvement of performances and background studies in GERDA Phase II”. In: (2017).

[21] Michelle J Dolinski, Alan WP Poon, and Werner Rodejohann. “Neutrinoless double-beta decay: status and prospects”. In: *Annual Review of Nuclear and Particle Science* 69 (2019), pp. 219–251.

[22] J Kotila and F Iachello. “Phase-space factors for double-β decay”. In: *Physical Review C* 85.3 (2012), p. 034316.

[23] Matteo Agostini et al. “Final results of GERDA on the search for neutrinoless double-β decay”. In: *Physical review letters* 125.25 (2020), p. 252502.

[24] Felix Johann Fischer. “The Search for $0\nu\beta\beta$ Decay with LEGEND: Signal the Background and Back the Signal”. PhD thesis. Technische Universität München, 2022.

[25] John Bardeen and Walter Hauser Brattain. “The transistor, a semi-conductor triode”. In: *Physical Review* 74.2 (1948), p. 230.

[26] RD Baertsch and RN Hall. “Gamma ray detectors made from high purity germanium”. In: *IEEE Transactions on Nuclear Science* 17.3 (1970), pp. 235–240.

[27] John Ballato et al. “Glass-clad single-crystal germanium optical fiber”. In: *Optics express* 17.10 (2009), pp. 8029–8035.

[28] EJ Friebele, DL Griscom, and GH Sigel Jr. “Defect centers in a germanium-doped silica-core optical fiber”. In: *Journal of Applied Physics* 45.8 (1974), pp. 3424–3428.

[29] N Abgrall et al. “New limits on bosonic dark matter, solar axions, pauli exclusion principle violation, and electron decay from the Majorana demonstrator”. In: *Physical review letters* 118.16 (2017), p. 161801.

[30] Zbigniew Galazka. “Czochralski method”. In: *Gallium Oxide: Materials Properties, Crystal Growth, and Devices* (2020), pp. 15–36.

[31] Ettore Fiorini et al. “A search for lepton non-conservation in double beta decay with a germanium detector”. In: *Physics Letters B* 25.10 (1967), pp. 602–603.

[32] Juris Meija et al. “Isotopic compositions of the elements 2013 (IUPAC Technical Report)”. In: *Pure and Applied Chemistry* 88.3 (2016), pp. 293–306.

[33] Brianna J Mount, Matthew Redshaw, and Edmund G Myers. “Double-β-decay Q values of Se 74 and Ge 76”. In: *Physical Review C* 81.3 (2010), p. 032501.

[34] VE Guiseppe et al. “The MAJORANA neutrinoless double-beta decay experiment”. In: *2008 IEEE Nuclear Science Symposium Conference Record*. IEEE. 2008, pp. 1793–1798.

[35] SI Alvis et al. “Search for neutrinoless double-β decay in Ge 76 with 26 kg yr of exposure from the M ajorana D emonstrator”. In: *Physical Review C* 100.2 (2019), p. 025501.

[36] S Schönert et al. "The GERmanium Detector Array (GERDA) for the search of neutrinoless $\beta\beta$ decays of 76Ge at LNGS". In: *Nuclear Physics B (Proceedings Supplements)* 145 (2005), pp. 242–245.

[37] *Mirion, Broad Energy Germanium detectors*. URL: https://www.mirion.com/products/bege-broad-energy-germanium-detectors (visited on 11/08/2023).

[38] GERDA Collaboration grabmayr@ uni-tuebingen. de et al. "Upgrade for Phase II of the Gerda experiment". In: *The European Physical Journal C* 78 (2018), pp. 1–30.

[39] M Agostini et al. "Characterization of inverted coaxial [... formula...] Ge detectors in GERDA for future double-[... formula...] decay experiments". In: *The European Physical Journal. C, Particles and Fields* 81.6 (2021).

[40] Stefano Riboldi, Alberto Pullia, and Carla Cattadori. "Improvement of the "CC2" charge sensitive preamplifier for the GERDA phase II experiment". In: *2012 IEEE Nuclear Science Symposium and Medical Imaging Conference Record (NSS/MIC)*. IEEE. 2012, pp. 782–785.

[41] M Agostini et al. "Calibration of the GERDA experiment". In: *The European Physical Journal C* 81 (2021), pp. 1–11.

[42] "Background-free search for neutrinoless double-β decay of 76Ge with GERDA". In: *Nature* 544.7648 (2017), pp. 47–52.

[43] *L. Pertoldi, gedet-plots*, 2019. URL: https://github.com/gipert/gedet-plots (visited on 09/08/2023).

[44] CE Aalseth et al. "IGEX 76 Ge neutrinoless double-beta decay experiment: prospects for next generation experiments". In: *Physical Review D* 65.9 (2002), p. 092007.

[45] Hans Volker Klapdor-Kleingrothaus et al. "Latest results from the Heidelberg-Moscow double beta decay experiment". In: *The European Physical Journal A-Hadrons and Nuclei* 12 (2001), pp. 147–154.

[46] M Agostini et al. “Production, characterization and operation ofˆ 76 76 Ge enriched BEGe detectors in G ERDA: GERDA Collaboration”. In: *The European Physical Journal C* 75 (2015), pp. 1–22.

[47] Dušan Budjáš et al. “Pulse shape discrimination studies with a Broad-Energy Germanium detector for signal identification and background suppression in the GERDA double beta decay experiment”. In: *Journal of Instrumentation* 4.10 (2009), P10007.

[48] Michael Miloradovic. “Characterisation of Inverted Coaxial Detectors and Calibration Source Production for the GERDA Experiment”. PhD thesis. University of Zurich, 2020.

[49] DG Phillips et al. “The Majorana experiment: an ultra-low background search for neutrinoless double-beta decay”. In: *Journal of Physics: Conference Series*. Vol. 381. 1. IOP Publishing. 2012, p. 012044.

[50] *LEGEND*, URL: `https://legend-exp.org/` (visited on 12/08/2023).

[51] Frank Edzards et al. “Surface characterization of p-type point contact germanium detectors”. In: *Particles* 4.4 (2021), pp. 489–511.

[52] A Domula et al. “Pulse shape discrimination performance of inverted coaxial Ge detectors”. In: *Nuclear Instruments and Methods in Physics Research Section A: Accelerators, Spectrometers, Detectors and Associated Equipment* 891 (2018), pp. 106–110.

[53] Andreas Zschocke. “Analysis and evaluation of the pulse shape performance of an Inverted Coaxial HPGe detector for $0\nu\beta\beta$ Experiments”. PhD thesis. Universität Tübingen, 2021.

[54] Ian Guinn et al. “Low background signal readout electronics for the MAJORANA DEMONSTRATOR”. In: *AIP Conference Proceedings*. Vol. 1672. 1. AIP Publishing. 2015.

[55] Y Efremenko et al. “Use of poly (ethylene naphthalate) as a self-vetoing structural material”. In: *Journal of Instrumentation* 14.07 (2019), P07006.

[56] Pall Theodorsson. *Measurement of weak radioactivity*. World scientific, 1996.

[57] Gerd Heusser. "Low-radioactivity background techniques". In: *Annual review of Nuclear and Particle science* 45.1 (1995), pp. 543–590.

[58] Glenn F Knoll. *Radiation detection and measurement*. John Wiley & Sons, 2010.

[59] *Table of decay isotopes data*. URL: https://www.nndc.bnl.gov/nudat3/.

[60] Michelangelo Ambrosio et al. "Measurement of the residual energy of muons in the Gran Sasso underground laboratories". In: *Astroparticle physics* 19.3 (2003), pp. 313–328.

[61] Christoph Wiesinger. "No neutrinos not found". PhD thesis. Technische Universität München, 2020.

[62] I Abt et al. "Background reduction in neutrinoless double beta decay experiments using segmented detectors—A Monte Carlo study for the GERDA setup". In: *Nuclear Instruments and Methods in Physics Research Section A: Accelerators, Spectrometers, Detectors and Associated Equipment* 570.3 (2007), pp. 479–486.

[63] Matteo Agostini et al. "Background free search for neutrinoless double beta decay with GERDA Phase II". In: *arXiv preprint arXiv:1703.00570* (2017).

[64] Frank Edzards, LEGEND Collaboration, et al. "The Future of Neutrinoless Double Beta Decay Searches with Germanium Detectors". In: *Journal of Physics: Conference Series*. Vol. 1690. 1. IOP Publishing. 2020, p. 012180.

[65] K Freund. "Muonic background in the GERDA $0\nu\beta\beta$ experiment". PhD thesis. Ph. D. Thesis, Eberhard Karls Universität Tübingen, 2014.

[66] V D'Andrea et al. "Pulse shape analysis in Gerda Phase II". In: *The European Physical Journal C-Particles and Fields* 82.4 (2022).

[67] M Agostini et al. "Pulse shape discrimination for GERDA Phase I data". In: *The European Physical Journal C* 73 (2013), pp. 1–17.

[68] Andreas Hocker et al. *TMVA-toolkit for multivariate data analysis with ROOT: users guide*. Tech. rep. 2007.

[69] Andrea Lazzaro. “Signal processing and event classification for a background free neutrinoless double beta decay search with the GERDA experiment.” PhD thesis. Technische Universität München, 2019.

[70] *3M, Daylighting Film DF2000MA*, 2007.

[71] *E. T. Enterprises, 9354KB series data sheet*. 2012. URL: "http://lampes-et-tubes.info/pm/9354KB.pdf".

[72] *Sigma-Aldrich, 161403 IR Spectroscopy Oil, safety sheet*. 2014. URL: "https://www.sigmaaldrich.com/DE/en/sds/aldrich/d161403".

[73] Florian Ritter. “Analysis of the GERDA muon veto. First light”. In: (2012).

[74] B. Shaybonov K. Freund F. Ritter and P. Grabmayr. *Update on the Muon Veto — installation of the DAQ*. Tech. rep. GERDA Scientific Technical Reports, GSTR-10-003, 2008.

[75] T. Kihm and B. Schwingenheuer. *List of DAQ tags*. Tech. rep. GERDA Scientific Technical Reports, GSTR-12-002, 2014.

[76] Markus Alexander Knapp. “Design, simulation and construction of the GERDA-muon veto; Design, Simulation und Aufbau des GERDA-Myonvetos”. In: (2009).

[77] *Sigma-Aldrich, 161403 IR Spectroscopy Oil*. 2014. URL: "https://www.sigmaaldrich.com/DE/de/product/sial/161403".

[78] GEANT Collaboration, S Agostinelli, et al. “GEANT4–a simulation toolkit”. In: *Nucl. Instrum. Meth. A* 506.25 (2003), p. 0.

[79] Melissa Boswell et al. “MaGe-a Geant4-based Monte Carlo application framework for low-background germanium experiments”. In: *IEEE Transactions on Nuclear Science* 58.3 (2011), pp. 1212–1220.

[80] Mark B Chadwick et al. “ENDF/B-VII. 1 nuclear data for science and technology: cross sections, covariances, fission product yields and decay data”. In: *Nuclear data sheets* 112.12 (2011), pp. 2887–2996.

[81] Christoph Wiesinger, Luciano Pandola, and Stefan Schönert. "Virtual depth by active background suppression: revisiting the cosmic muon induced background of GERDA Phase II". In: *The European Physical Journal C* 78.7 (2018), p. 597.

[82] VA Kudryavtsev. "Muon simulation codes MUSIC and MUSUN for underground physics". In: *Computer Physics Communications* 180.3 (2009), pp. 339–346.

[83] R L Brodzinski and N A Wogman. "HIGH-ENERGY PROTON SPALLATION OF ARGON." In: *Phys. Rev., C 1: 1955-9(Jun 1970).* (Jan. 1970). DOI: 10.1103/PhysRevC.1.1955. URL: https://www.osti.gov/biblio/4158191.

[84] Christian Gumpert et al. "Software for statistical data analysis used in Higgs searches". In: *Journal of Physics: Conference Series*. Vol. 490. 1. IOP Publishing. 2014, p. 012229.

[85] Glen Cowan et al. "Asymptotic formulae for likelihood-based tests of new physics". In: *The European Physical Journal C* 71 (2011), pp. 1–19.

[86] Matteo Agostini et al. "Modeling of GERDA Phase II data". In: *Journal of High Energy Physics* 2020.3 (2020), pp. 1–39.

[87] Ann-Kathrin Schütz. "Full analysis of the background for the search of neutrinoless double beta decay in GERDA". PhD thesis. Universität Tübingen, 2020.

[88] K. von Sturm E. Bossio L. Pertoldi and C. Wiesinger. *Measurement of the 85Kr activity in GERDA*. Tech. rep. GERDA Scientific Technical Reports, GSTR-23-002, 2023.

[89] Xiang Liu Kevin Kröninger. *Initial results from the GERDA Monte Carlo Simulation of internal bakground - Update 1*. Tech. rep. GERDA Scientific Technical Reports, GSTR-05-019, 2005.

[90] Alejandro Sonzogni. "NNDC chart of nuclides". In: *International Conference on Nuclear Data for Science and Technology*. EDP Sciences. 2007, pp. 105–106.

[91] Samuel S Wilks. "The large-sample distribution of the likelihood ratio for testing composite hypotheses". In: *The annals of mathematical statistics* 9.1 (1938), pp. 60–62.

[92] Grégory Schott. "RooStats for searches". In: *arXiv preprint arXiv:1203.1547* (2012).

[93] L Pertoldi et al. *Monte carlo simulations and probability density functions for GERDA Phase II background model*. Tech. rep. GERDA Scientific Technical Reports, GSTR-18-009, 2018.

[94] *Material screening*, URL: https://www.mpi-hd.mpg.de/gerdawiki/index.php/TG-11_Material_screening (visited on 10/08/2023).

[95] Arno Gadola et al. "FlashCam: a novel Cherenkov telescope camera with continuous signal digitization". In: *Journal of Instrumentation* 10.01 (2015), p. C01014.

[96] F Aharonian et al. "Observations of the Sagittarius Dwarf galaxy by the HESS experiment and search for a Dark Matter signal". In: *Astroparticle Physics* 29.1 (2008), pp. 55–62.

[97] AU Abeysekara et al. "Sensitivity of the high altitude water Cherenkov detector to sources of multi-TeV gamma rays". In: *Astroparticle Physics* 50 (2013), pp. 26–32.

[98] Sandeep Koranne and Sandeep Koranne. "Hierarchical data format 5: HDF5". In: *Handbook of open source tools* (2011), pp. 191–200.

[99] *Pygama software*, URL: https://github.com/legend-exp/pygama/.

[100] Jeff Chase and Ilya Baldin. "A retrospective on orca: Open resource control architecture". In: *The GENI Book* (2016), pp. 127–147.

[101] O. Schulz M. Agostini J. A. Detwiler and C. G. Wiseman. *Data Organization and Terminology for LEGEND 200 (version 3)*. Tech. rep. LEGEND Technical Reports, LTR-20-001, 2020.

List of Figures

List of Tables